# PHYSICOCHEMICAL SURFACE INTERACTIONS OF NANOIMPRINT LITHOGRAPHY RESISTS AND IMPRINTED PORE MEMBRANES

by

Philip Y. Choi

A dissertation submitted in partial fulfillment
of the requirements for the degree of
Doctor of Philosophy
(Electrical Engineering)
in the University of Michigan
2010

Doctoral Committee:

Associate Professor L. Jay Guo, Chair
Associate Professor Wei Lu
Associate Professor Euisik Yoon
Assistant Professor Anish Tuteja

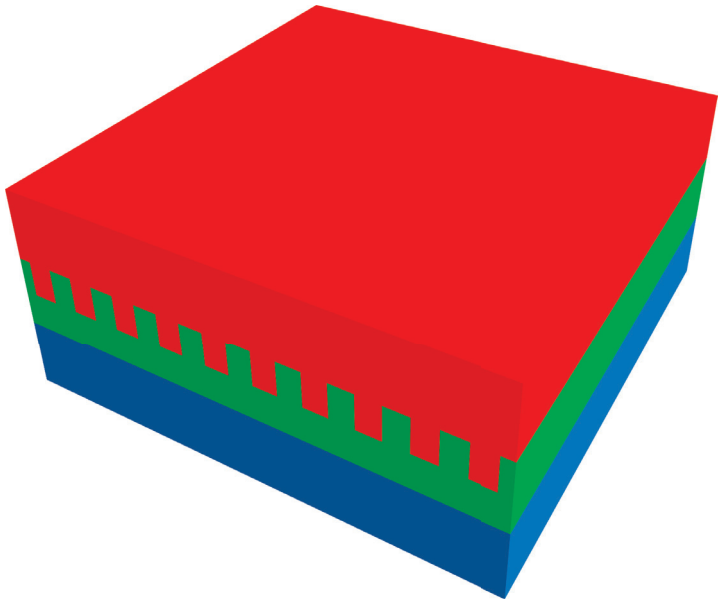

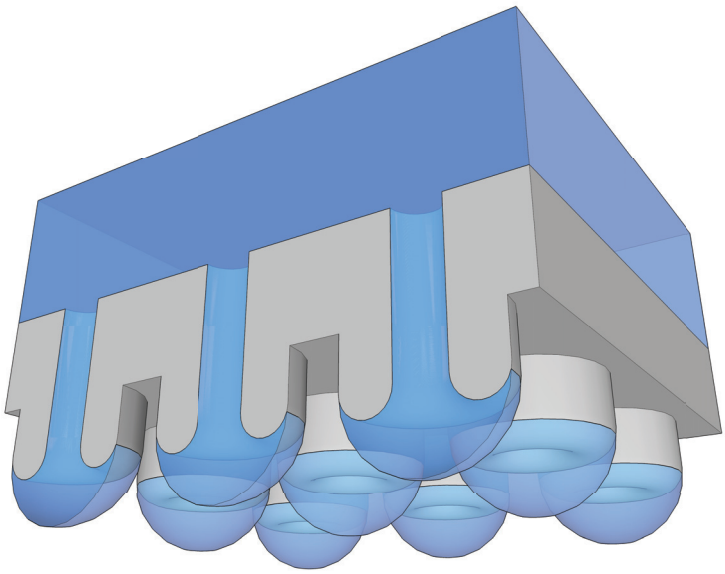

For Sejica

## PREFACE

When I began graduate school, my father, an engineering professor himself, told me, "Above all else, the PhD is a test of endurance." My experience in this endeavor has proven to be nothing less. Throughout the years I have experienced countless challenges to my perseverance. But though the journey was long and difficult, I have learned a great deal, both professionally and personally.

In the beginning, I was accepted to an interdisciplinary NSF IGERT fellowship, for which I am grateful. I would like to thank the Foundation and Profs. M. David Curtis and Richard Laine for organizing such a wonderfully diverse and educational experience. My first research rotation was with Prof. David Martin; I learned a great deal about lab work from his research group. Thank you, Larry, Yinghong, and Junyan for your mentorship early on. From this early period until the terminus, my eyes in the nano world have been the scanning electron microscopy equipment in EMAL. My thanks to Dr. John Mansfield, who operates a first-rate microscopy lab which the entire university depends on. Away from Michigan during my first summer, I had the enriching opportunity to immerse myself in a far-removed microbiological research lab at the University of North Carolina. My thanks to Prof. Jian Wang for inviting me to rotate through his group, where I gained a great appreciation for the natural world and its applicability to my nanoscale research.

When I began research in my home department, opportunities that fit my broad research curiosities were few and far between. I extend my deep gratitude to my research advisor, Prof. L. Jay Guo for his support and enthusiasm so early on. I could not imagine being able to explore such a broad field of research without his patronage. In his group, I solidified my skills in experimentation and research synthesis; I would like to thank the early mentors I had for teaching me so much: Grant, Xing, and Chung-Yen. Working together with many fine individuals has been a rewarding and enriching experience, and I

am grateful to past and current group members: Brandon, Larry, Carlos, Jinsung, Myung-Gyu, Se Hyun, Tao, Wayne, Sting, and so many more.

While exploring copolymer imprint resists, I had the chance to collaborate with an expert in polymer synthesis at Dow Corning. I thank Dr. Peng-Fei Fu for his significant contributions to this phase of the research, providing the polymers themselves, and his expertise and mentorship. Dr. Jinsung Kim, an intrepid postdoctoral researcher, provided the high quality imprint molds used to fabricate the smallest features in my research—his contribution is invaluable. Prof. Zhan Chen allowed me to make the very important contact angle measurements using his goniometer equipment; thank you.

While exploring applications of the imprinting expertise I gained early on, I had the chance to collaborate with Prof. Jinsang Kim soon after he arrived at the university. His enthusiasm and energy are rare. Prof. Kim served on my dissertation committee during the proposal phase, but unfortunately it was too difficult for him to serve in the final phases of my dissertation defense from abroad. My deep gratitude and best wishes to Prof. Kim for his mentorship.

All of the intricate fabrication work in this dissertation was performed in the LNF cleanroom laboratory. Without the hard work and dedication of the scientific staff in the lab, it would fall apart. My thanks to the many staffers who have not only maintained, but directly assisted me in the use of such sophisticated equipment. Their help has saved me innumerable amounts of time. Thank you Greg, Brian, Kimberly, Jim, Cedric, and Ed for teaching me how to use vital equipment. My gratitude goes out to Dave, Dennis, Phil, Tim, Steve, Matthew, and Sandrine for helping in so many ways. Nanonex provided a great deal of technical support for the NX-2000 NIL equipment that was used to make all the imprints in my research. None of the high quality imprints would have been possible without this help. I would like to thank their engineers, Larry, Mark, Linshu, and Tony, for their support of this invaluable machine.

Part of the reason why graduate school has been so enriching were the numerous teaching opportunities that I received in the department. Through these experiences I have become a patient and insightful instructor, and it improves my ability to explain my research to others. My thanks to Profs. Yoon, Ganago, Najafi, and Lu, for the experience

to learn from and work alongside them. To Arun, Katherine, Robert, and Terre, teaching one of the most demanding courses in the department with you was a treat.

To my fellow graduate students who mentored me when I began, I owe my success. Thanks Amar, Steve, Senol, Sunny, and Xin. So many little things that go unnoticed were done by dedicated administrative staff, whose expertise and diligence kept operations running smoothly during my time in graduate school. Thank you Beth, Karen, Deb, Aiko, Nonna, Betty, Laura, Trasa, Gary, and Bonnie.

My committee members represent a broad slice of the intellect, and it is their expert advice and critique that makes the success of this dissertation possible. With so many broad disparate topics in my work, I depend on their collective knowledge to help solidify my research. Thank you Profs. Guo, Kim, Lu, Tuteja, and Yoon. The challenges and rigors of experimental research have made me impose a demanding schedule on their parts towards the close of my degree, and I am eternally grateful to them for their diligence and sacrifice of time to help me succeed. I would like to mention that Prof. Tuteja, whom I have cited heavily in the latter portion of my research, agreed to serve on my committee a mere two weeks before my defense, having just been appointed at the university the prior semester.

As I stand at the zenith of my graduate studies, I look back and reflect upon the many years spent here at Michigan. I would not be here if not for the loving support and guidance of my mother, Hoyoun and my father, Kyung-Kook. I thank my parents and my sister, Heather, for their patience through this long and arduous journey.

To my fiancée, Sejica, I can never fully express my gratitude. Your unwavering, unconditional love and support during the most difficult part of my dissertation has made all the difference. I am so glad you persevered through it beside me, and I am forever indebted to you for it. Thank you for believing in me.

To my readers, thank you for your interest in my research. It is my hope that you might learn something useful from my many years of hard work on this dissertation. The best way to contact me will be through email: choip@umich.edu

Phil Choi

January 18, 2010

## TABLE OF CONTENTS

## LIST OF FIGURES

Figure

## LIST OF TABLES

Table

## LIST OF APPENDICES

Appendix

## ABSTRACT

This dissertation begins by presenting the use of inorganic copolymer imprint resists, namely siloxane graft and block copolymers. These new materials are shown to have lower resist to mold adhesion such that mold-release is more reliable without delamination from the substrate. Due to the high fraction of silicon atoms, these resists have a high degree of plasma etch resistance compared to organic polymers, so they serve as excellent high-contrast masks to facilitate pattern transfer into underlaying layers. Feature sizes of 60 nm, and possibly below, can be imprinted. Copolymerized resists presented here are single-chain component systems, offering convenience over multicomponent miscible mixtures. The graft copolymers PDMS−*g*−PMIA and PDMS −*g*−PMMA demonstrated the best performance due to their higher degree of homogeneity.

To achieve a greater understanding of the wetting behavior of liquid imprint resists on mold surfaces, the phenomenon has been modeled by analysis of liquid-solid interfacial energies. The calculation methods presented here are unique in that the microscopic profile of the solid surfaces were parameterized for accurate modeling of carefully measured sample sidewalls. Equilibrium free energy minimization as well as nonzero liquid pressures were used to predict the dynamic behavior of the interacting systems. Meniscus pressure calculations in particular are a new contribution.

To test the wetting models and verify the predictions of wetting behavior, freestanding, porous polymer membranes were fabricated using a modified imprinting process. These durable SU-8 polymer membranes were insoluble against a variety of test fluids. Pore morphologies were controlled to the same level of nanometer-scale accuracy due to the fidelity of the NIL process used. The modified process demonstrates the possibility of applying imprint processing to micrometer-scale size regimes and three-dimensional processing. Liquid breakthrough pressures were measured on the two types

of membranes. Cross-sectional profiles of the pores, accurately scanned and digitized by electron microscopy, were used to predict wetting behaviors, and the results were compared. The small pressures were measured using a sensitive manometer, and measured wetting behavior was found to be in good agreement with the model.

# CHAPTER I

## Introduction

Nanoimprint lithography (NIL) is a fabrication technology designed to rapidly produce high-resolution patterns in planar microfabrication settings. A solid relief mold containing the desired feature pattern is brought into physical contact with a deformable imprint resist material. Once the resist has assumed the desired shape, the imprint mold is removed, leaving the freestanding pattern in the resist layer, as illustrated in Figure 1.1.

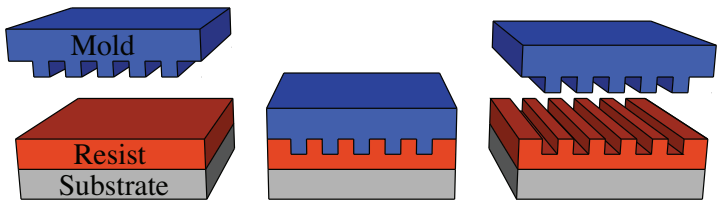


Figure 1.1: The nanoimprint lithography process.

NIL was designed as an improvement over existing microfabrication technologies. Mask-based radiative lithography techniques, such as photolithography and extreme ultraviolet (EUV) lithography, pattern resist by exposure to photon radiation. These processes have rapid throughput and minimal defects because no contact is made with the resist layer. However, as the size of pattern features approaches the de Broglie wavelength of the radiative particles in use, the quantum mechanical wave behavior prevents clear boundaries between exposed and unexposed regions, leading to loss of definition. Mask-less or "direct write" small-wavelength patterning, such as electron-beam (e-beam) lithography, have throughput limitations due to the raster scanning process that is required to define a pattern area (rather than the full-field exposure of photolithography). Instead, NIL can pattern a mold-sized area of sub-optical wavelength

features in one relatively rapid imprint step. The origins of high-resolution NIL molds are typically from e-beam lithography processes. Though the electron has a smaller de Broglie wavelength, and hence can resolve smaller features than photons, the absence of sufficiently powerful electron sources precludes rapid patterning by e-beam lithography. But because the NIL mold is reusable, the resource cost of mold fabrication scales as a small fraction of the overall number of imprinted patterns. This model of scale is similar to the costly nature of photomasks that can then be used to expose immense quantities of photoresist coated substrates.

High-resolution patterning in NIL is made possible by direct physical contact pattern transfer unlike contact-less methods. The resolution is not limited by any wavelength, but rather the conformability of the resist to the mold. The tradeoff is that the direct contact between imprint mold and resist introduces a unique set of processing issues that do not exist in radiative lithography methods. Chemical interactions between the surfaces of the three materials in Figure 1.1 give rise to various adhesion forces. These forces in turn cause mechanical interactions between mold, resist, and substrate. This dissertation presents research that addresses these interactions. The physical basis of these interactions is explored with the goal of improving the overall imprinting process.

## Nanoimprint Lithography

Nanoimprint Lithography (NIL) has been shown very early by Chou *et al*. to produce fields of sub-10 nm features, and more recently 5 nm features by Austin *et al*. The process has been shown to replicate fields as large as 200 mm by Perret *et al*. Two classes of imprint resist materials are in use, broadly dividing NIL into two categories: plastic deformation, reported by Chou *et al*. in 1997 and crosslinking polymerization, reported by Willson *et al*. in 1999. All techniques involve the aforementioned contact between resist material and mold. The first set of imprint resists are thermoplastic polymers; these are solids at room temperature that undergo a transition to a viscoelastic

material above a certain characteristic temperature known as the glass transition, $T_g$. The bulk modulus decreases substantially in this regime, and polymer creep increases such that applied stress from the imprint mold causes controlled deformation. When the temperature is reduced with the mold held in place, the deformation is permanent as the resist becomes a solid again. The earliest thermoplastic imprint resists were poly(methyl methacrylate) (PMMA).

Crosslinking polymers are the second set of resists; these are low viscosity fluids that readily assume the contours of the imprint mold. Because of the low viscosity, less molding pressure is required. The crosslinking reaction is initiated externally by heat or light, causing the molecules of the resist to polymerize, producing the permanent final solid shape. The earliest crosslinking imprint resists were acrylate and siloxane monomer blends. At the conclusion of either of these processes, the imprint mold is forcibly removed from the formed resist. A thin residual layer of resist material is left covering the substrate in the otherwise recessed regions, and it is necessary to remove this by controlled anisotropic plasma etching. Afterwards, the resist profile is similar to the result obtained from other lithography methods following their develop processes.[1-7]

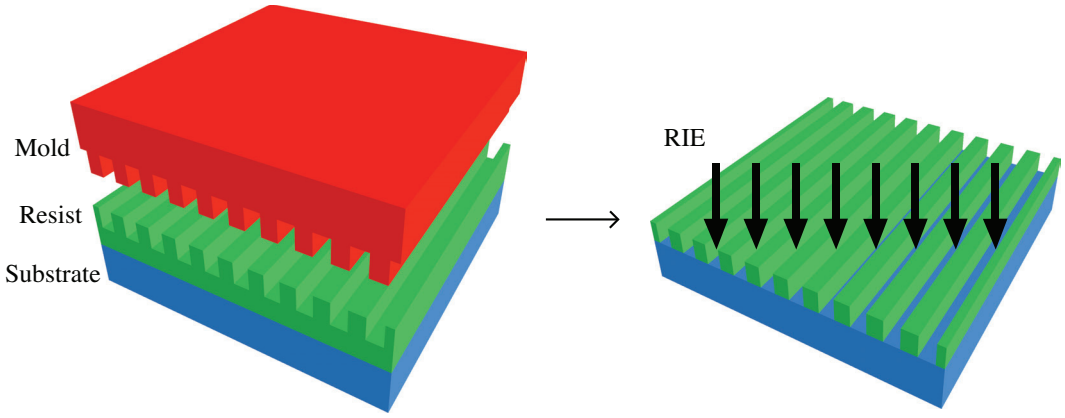


Figure 1.2: After imprinting, the residual layer is etched to produce a result similar to other lithography methods.

Large adhesion forces between the mold and resist have been identified as a critical issue in the NIL process.[8-9] During the release step of the process, it is imperative that the imprint resist remain wholly adhered to the substrate and not the

mold. To date, solutions to this issue are nontrivial and require specific engineering design of all three materials as well as process parameters. This solid to solid adhesion is explored in detail in Chapter II. Additionally, during the imprint step, the resist, as a viscoelastic melt or liquid-phase precursor, flows and conforms to the mold and substrate surfaces. Issues that may arise during this part of the process include partial dewetting and void formation. Liquid-solid adhesion is also explored in detail in Chapters III and IV.

## Surface and Interfacial Energies

Surfaces of condensed matter can be characterized by a surface free energy per unit area, $\sigma$. This quantity describes the increase in free energy required to increase by a proportional amount the surface area of the continuum matter. Surface energy is sometimes referred to by the variable $\gamma$, and typically carries a subscript of $s$, $l$, or $a$ to denote solid, liquid, or gas phase matter. Surface energy has units of energy per area. For two separate bodies of matter in contact, interfacial free energy terms are used to describe the interaction. The notation used to describe the paired interactions reflects the two materials involved; the interfacial energy between a liquid in contact with a solid material would be denoted $\sigma_{sl}$. Analogous to surface energy, this interfacial energy describes the energy required to increase the interfacial area between the liquid and solid matters, such as a fixed volume of liquid wetting a solid surface.[10-11]

These surface and interfacial energies are illustrated in Figure 1.3. In the first example, a single phase of material with fixed volume $V$, surface area $A_0$, has a surface free energy of $G_0$. The material is then deformed such that its surface area changes to $A_1$. The resulting change in surface energy $G$ is proportional to the product of surface energy per area $\sigma$, and change in surface area $A$. As covered in detail by Adamson and later Israelachvili, all $\sigma$ values are greater than zero, and if the surface area of the material was increased, external work was required make this deformation occur. In the second

example, two different materials, one a solid and the other a liquid, have an interfacial area of $A_0$ and an interfacial free energy of $G_0$. The two materials are then displaced such that their interfacial area changes to $A_1$. The resulting change in interfacial energy $G$ is proportional to the product of interfacial energy per area $\sigma_{sl}$, and change in interfacial area $A$. If the interfacial area of the materials was increased, external work was required make this deformation occur as well.

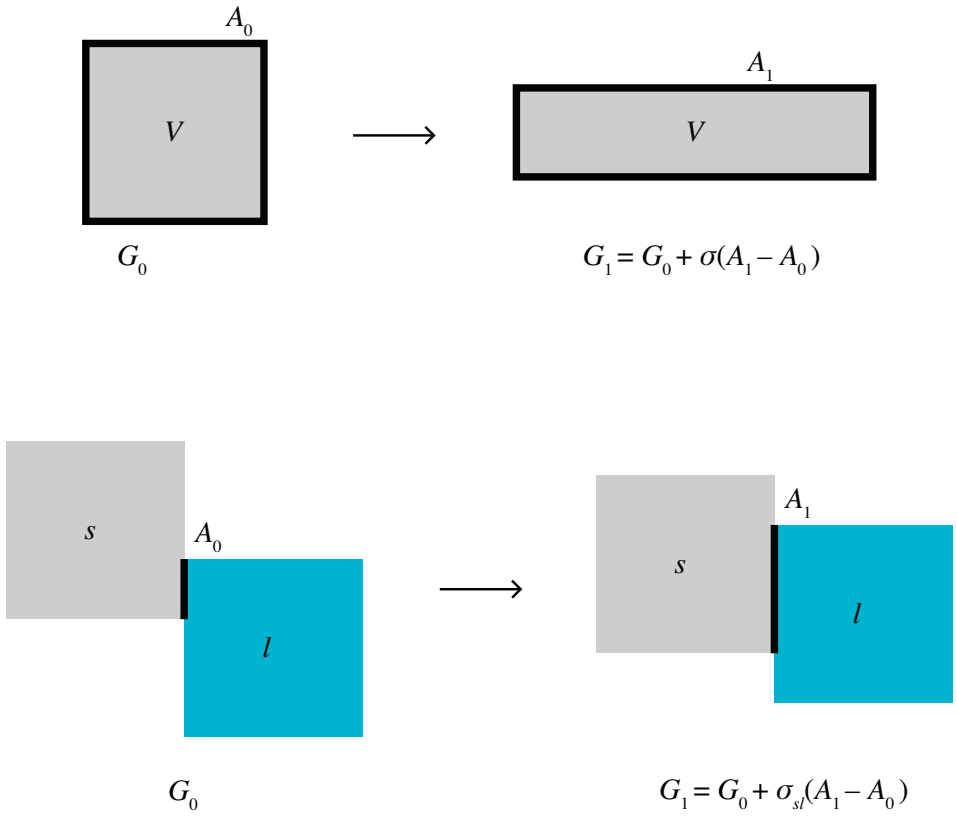


Figure 1.3: Surface or interfacial energy $G$ is proportional to the product of $\sigma$ and $A$.

These macroscopic properties are the collective manifestation of various intermolecular forces, first hypothesized by van der Waals, and further elucidated by Keesom, Debye, and London. Unbonded molecules in close proximity experience attractive forces due to fixed dipole interactions and induced dipole interactions. Wholly non-polar species are also subject to attractive forces due to fluctuating electron orbitals causing momentary dipolar induction. As such, the presence of permanent dipoles, and

susceptibility to polarization are contributing factors to the van der Waals adhesion between dissimilar materials. Molecules with asymmetrical electron and nucleus structures, particularly those comprised of alkali metals and halogens, have dipole moments, the product of charge magnitudes and separation lengths. Such polar molecules can induce dipoles in neighboring, otherwise apolar chemical species. All molecules have a characteristic polarizability, the ratio between the induced dipole moment that occurs in a given electric field. These two characteristics determine the degree of the interfacial energy between two distinct phases of matter.

## Mold, Resist, and Substrate Adhesion

As the intermediate layer between mold and substrate, the imprint resist polymer must have a higher adhesion energy with the substrate than with the mold. Because the total interfacial energy $\sigma A$ between dissimilar materials is proportional to the interfacial area, the pattern-bearing resist-mold interface will experience stronger adhesion than the smooth resist-substrate interface. Specific use of mold and substrate materials such that $\sigma A$ between mold and resist was kept below $\sigma A$ between resist and substrate provided workable early solutions, such as coated nickel molds and silicon substrates as shown by Keil *et al*. and Lee *et al*.[12-13] These molds had low enough interfacial $\sigma$ with the imprint resists to prevent exceeding $\sigma A$ between resist and substrate. However, changing mold materials was a difficult task, because most of the high resolution mold patterns were generated using low-throughput e-beam lithography on silicon substrates and its derivatives. A subsequent strategy still in wide use is to specifically modify the surface of these silicon molds with a low $\sigma$, molecular fluoro-surfactant coating, first reported by Jaszewski *et al*.[14-15] Alternative coatings based on siloxanes have been reported by Lee *et al*. and oxazines by Wang *et al*.[16-17] Furthermore, molds composed not of silicon, but of bulk low $\sigma$ polymers, as shown by Schmid and Michel, McClelland *et al*.,

Kim *et al*., Khang *et al*., and Choi *et al*., were themselves imprinted by or cast from silicon molds.[18-23]

In addition to modifying the mold to reduce its $\sigma$, the imprint resist material can be modified to achieve favorable demolding performance as well. However, because the resist material is in contact with both the mold and substrate, changing its $\sigma$ will affect both interfacial energies. Adamson summarizes based on Fowkes, Girifalco, and Good that the interfacial free energy is a monotonically increasing function of the surface free energies of the constituent phases. However, non-homogeneous polymers, such as graft or block copolymers, or miscible blends, are known to phase separate near the bulk surfaces. This occurs in a manner that exposes low $\sigma$ copolymer chain components to neighboring low energy phases, and high $\sigma$ components to high energy surfaces, as described by Chen and Gardella, Yilgör, Stoebe *et al*., Ma *et al*., Xu *et al*., and Barbero *et al*.[24-32] A newly engineered imprint resist that utilizes this strategy and exhibits the dual surface behavior is described in Chapter II. This work focuses on organic-inorganic copolymers where the low $\sigma$ component is siloxane chains and grafts. High resolution features down to 60 nm were imprinted into these resists.

## Residual Layer

After the imprint resist has been shaped, there typically exists a thin residual layer. This residual layer must be removed to make the resulting resist pattern compatible with existing microfabrication paradigms. In photolithography, the radiation exposure activates embedded photo-acids. After exposure, the resists are immersed in basic "developer" baths; regions of irradiated resist readily dissolve in the high pH solutions while unexposed regions remain insoluble. In e-beam lithography, the radiation exposure causes scission in long polymer chains, thereby increasing the dissolution rate when the resists are immersed in weak solvents. Both processes are designed such that the resist

from exposed regions is fully removed or developed down to the underlying substrate or layer.

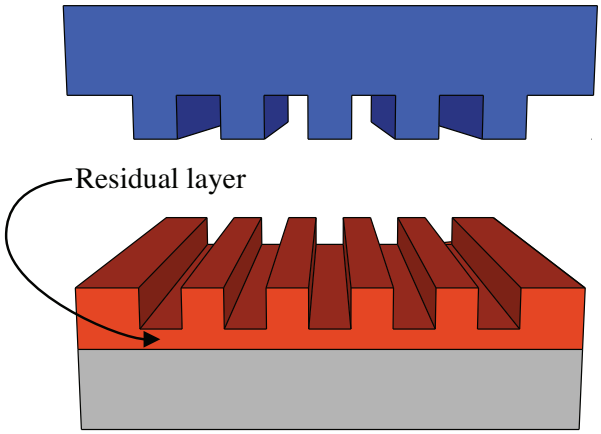


Figure 1.4: Residual layer after imprinting.

Analogous to these developing processes, the common method of removal of NIL residual layers is with an anisotropic reactive ion plasma etch (RIE). Choices of etch chemistry are limited by the need for high etch selectivity; initially, $O_2$ plasma was used widely on homopolymer imprint resists to avoid etching anything but the polymer.[1] Though the residual resist material must be definitively removed by RIE, it is desirable for the layer to possess some degree of etch resistivity that is useful in the context of microfabrication. As with photo and e-beam resists, organic imprint resists are susceptible to rapid etching in $O_2$ plasma. There is some moderate resistance to plasmas used to etch underlying inorganic materials, as demonstrated by Schulz *et al*.[36] Williams *et al*. have compiled a thorough review of these chemistries.[33-34] Complete removal of the residual layer also facilitates high-resolution liftoff patterning, as shown by Carlberg *et al*.[35] Applying multilayer resists of varying etch selectivity has been demonstrated by Hofer *et al*. and earlier to e-beam lithography by Howard *et al*.[37-38] and this strategy is one that is also utilized with the imprint resist presented in this work. Chapter II describes the etch behaviors of the siloxane copolymer resists in various relevant RIE chemistries.

## Solid Surface Wetting

Crosslinking imprint resists are applied as a low-viscosity liquid precursor.[2] Unlike the viscoelastic thermoplastic imprint resists, this form of material requires far less molding pressure to form pattern features. But liquid dewetting effects may cause incomplete molding and pattern loss. Thermal resists can also be susceptible to dewetting problems while heated above $T_g$ as shown by Reiter, and this viscoelastic flow has been studied by Rowland *et al*.[41-43] Crosslinking resists are often deliberately designed so that the solid after curing will have low surface energy $\sigma$. This can further exacerbate dewetting issues. Modification of the substrate to increase its $\sigma$ is one possible workaround, as shown by Cheng *et al*.[44] However, this approach is not readily applicable to the imprint mold, which should maintain a low $\sigma$.

To develop an understanding and model for liquid resist behavior on the solid mold and substrate surfaces, the origins of solid surface wetting are studied. In the simple case of a liquid droplet on a flat surface, the balance of interfacial tension forces at the triple-point where solid, liquid, and gas phases meet results in a characteristic contact angle $\theta$, as described by Young's equation.

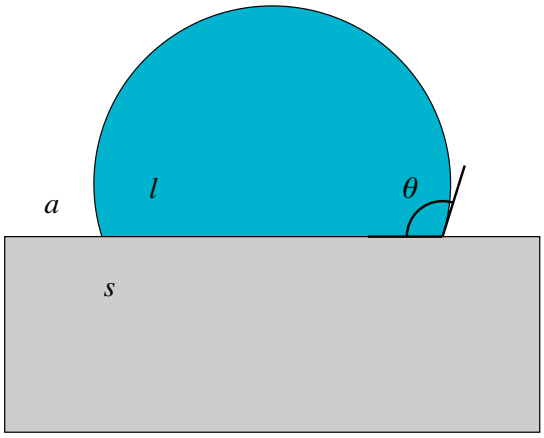

Figure 1.5: The contact angle.

$$\sigma_{sa} = \sigma_{sl} + \sigma_{la}\cos\theta \tag{1.1}$$

In equilibrium, a sufficiently small droplet, denoted $l$, is accepted to be spherical in shape. The effects of gravity are negligible and the droplet is in contact with a flat solid surface, denoted $s$. Air surrounds the entire setup, denoted $a$. Because the liquid droplet and surrounding air medium are fluids, both will deform until the free energy of the system is minimized. The consequence of this minimization is that the droplet assumes the shape of a section of a sphere, bordered by a circular plane sharing an interfacial contact area with the solid surface, and a dome-shaped interface with the air. The line of intersection of all three phases, $s$, $l$, and $a$, is a circle and referred to as the "triple point". At the triple point, the normal angle measured between the solid-liquid interface and the tangent to the liquid-air interface is referred to as the contact angle $\theta$.

Dimensional analysis allows the surface energy $\sigma$ to be considered a surface "tension". This tension is a distributed force, parallel to the interface plane, acting across a line—in this case the line is the circumference of the triple point circle. The three forces $F$ are the product of $\sigma$ and this circumference, and because the triple point is at equilibrium and nonmoving, the vector sum of the forces parallel to the solid surface gives rise to Equation 1.1. This equation utilizes the tangent contact angle $\theta$, which the triple point assumes whenever the system is at equilibrium. Conversely, if the triple point angle is not $\theta$, the system is not in equilibrium and the angle or triple point location can be expected to move. In Figure 1.6, the seemingly unbalanced component of $F_{la}$ that is normal to the solid surface is counteracted by the bulk cohesion of the solid material (not drawn). Liquid-solid interactions resulting in contact angles $\theta$ greater than 90 degrees are commonly referred to as dewetting, and the opposite, wetting.

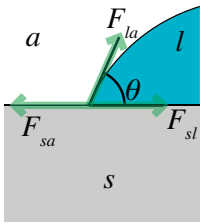


Figure 1.6: Derivation of Young's equation.

With the help of microscopic imaging, the situation on real surfaces was found to not be so ideal, however. Apparent contact angles were found to be affected by the presence of microstructures on the solid surface, as described by Wenzel, and Cassie and Baxter. Wenzel described the complete wetting of the patterned solid surface, and Cassie, the partial wetting and existence of air voids interrupting the solid-liquid interface. [45-46]

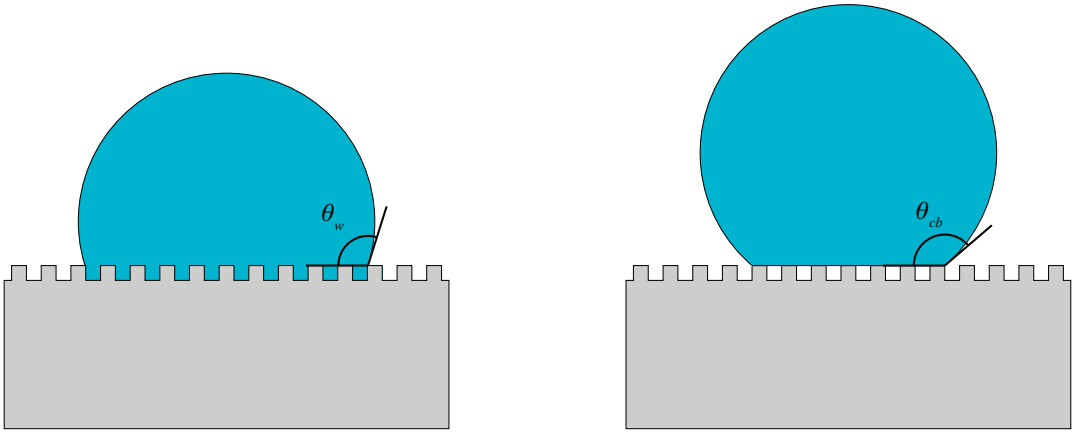


Figure 1.7: Left, Wenzel and right, Cassie wetting states and their associated apparent contact angles.

$$\cos\theta_w = \frac{A_{rough}}{A_{projected}}\cos\theta \tag{1.2}$$

$$\cos\theta_{cb} = \frac{A_{contact}}{A_{projected}}\cos\theta - \left(1 - \frac{A_{contact}}{A_{projected}}\right) \tag{1.3}$$

In Wenzel mode wetting, the area fraction represents the ratio of the patterned solid surface area to the projected or apparent solid surface area. In Equation 1.2, $\theta$ is the Young's contact angle, while $\theta_w$ is the apparent Wenzel mode contact angle. This fraction is always greater than unity, and hence the presence of microstructures will increase apparent contact angles greater than 90 degrees, and decrease angles less than 90 degrees. Thus, the tendency for Wenzel mode wetting is to make liquids on smooth, dewetting surfaces to have even greater contact angles or "dewetting quality" with the addition of

microstructures. Likewise, liquids on smooth, wetting surfaces have even smaller contact angles with the addition of microstructures. The area fraction in the Cassie equation is the ratio of solid-liquid contact area to projected area, and this fraction is less than unity. In Equation 1.3, $\theta$ is the Young's contact angle, while $\theta_{cb}$ is the apparent Cassie mode contact angle. The result is a general tendency towards high apparent contact angles in the Cassie wetting state, with the potential to make even wetting surfaces appear to be dewetting. That is, liquids on any type of smooth surface will exhibit monotonically higher contact angles with the addition of microstructures and Cassie mode wetting.

It is this Cassie wetting mode that gives rise to such extreme liquid dewetting commonly observed in nature. Dubbed "superhydrophobicity", many plants and animals have naturally developed microstructures to inhibit wetting by water. Neinhuis and Barthlott, and Koch *et al*. have thoroughly surveyed vast numbers of natural Cassie mode surfaces, exhibiting numerous variations in morphologies.[47-48] Furstner *et al*. performed early experiments to replicate the hypothesized self-cleaning behavior seen in the well-known, superhydrophobic lotus leaf surface.[49] Later, Sun *et al*. made direct polysiloxane casts from lotus leaves.[50] Artificial surfaces have been designed to take Cassie mode wetting to the extreme, as demonstrated by Gao and McCarthy.[51]

Figure 1.8: Cassie state water droplets on the surface of *Brassica oleracea*.

Transitions between the two Cassie and Wenzel wetting states are poorly understood. Reports of observations of transitions from Cassie to Wenzel wetting states abound, but the reverse transition is not known to occur. Callies and Quere cited surfaces that could be electrically or radiatively switched to induce either Cassie or Wenzel modes, but this always relied on new droplets and interfaces, not existing droplets.[52] Bhushan *et al*. summarized several of their own reports being unable to induce Wenzel to Cassie transition of droplets, including direct microscopic observation.[53] Cheng *et al*. have directly observed microscopic droplets on lotus leaves transitioning to Wenzel mode during evaporation.[54] Ahuja demonstrated a well controlled transition from Cassie to Wenzel modes on microfabricated surfaces, but not the reverse.[55] Marmur and Patankar have made theoretical predictions about the nature of this transition, but neither has been experimentally verified.[56-57] Nevertheless, the wetting mode duality that micro-structured surfaces can achieve can be of utility, as demonstrated in the selectively absorbing nanowire membrane, by Yuan *et al*.[58]

## Modeling Equilibrium Wetting States

Marmur, Nosonovsky, and Tuteja *et al*. all take the generalized approach of the summation of all interfacial energy and area products as total interfacial free energy.[11, 53, 56, 59-62] This free energy $G$ varies depending on the relative values of the solid-liquid, solid-air, and liquid-air interfacial areas. Marmur, and later Nosonovsky, predicted local minima and maxima as functions of interfacial areas representing stable wetting states in the transition between Cassie and Wenzel modes for droplets on surfaces and immersed surfaces. Tuteja *et al*. went further to apply this paradigm to myriad experimental surfaces, including feathers, leaves, electrospun fabric, and micropatterned silicon. All researchers concluded that a reentrant surface microstructure will support a triple point location in a Cassie mode wetting state due to a local minima in $G$, and Tuteja

verified this by analysis of the fabric and (to greater experimental control) the specially patterned silicon.

$$G = \sigma_{sl}A_{sl} + \sigma_{sa}A_{sa} + \sigma_{la}A_{la} \tag{1.4}$$

All authors have modeled the solid wetting surfaces as closed-form plane, spheroid, and cylindroid geometries. In this work, the approach will be expanded upon to predict the existence of stable wetting states on micro-structured surfaces relevant to the NIL process. Chapter III will describe an analytical methodology based on curve tracing microscopically quantified surface structures to determine stable triple point locations. Chapter IV will cover the application of this methodology to porous membrane structures and predicting liquid flow behavior under pressurized conditions. The membrane structures themselves were fabricated using a specially developed NIL process, bringing the work full-circle. Experimental flow of pressurized liquids through these membranes were compared to theoretical predictions made by the analytical wetting model.

# CHAPTER II

## Siloxane Copolymer Imprint Resists

Two of the most critical steps in NIL are mold release and pattern transfer by RIE. Candidate polymers used in imprinting-based lithography should provide reliable releasing properties during the demolding process, while at the same time not compromising adhesion to the substrate. To address these critical needs, materials that possess dual surface properties are needed. Of special interest are the polydimethylsiloxane (PDMS)-organic block or graft copolymers.[63-64] In contrast to poly(methyl methacrylate) (PMMA) and organic polymers in general, siloxane copolymers exhibit significant differences by virtue of the highly open, flexible, and mobile Si−O−Si backbone. These qualities include low surface energy, low glass transition temperature, and high thermal stability. Furthermore, it is known that these copolymers undergo micro-phase segregation above their glass transition temperature ($T_g$) due to the unfavorable enthalpy of mixing.[24-32]

Siloxane copolymers offer another advantage over homopolymers as NIL resist due to much improved etching resistance. When exposed to oxygen plasmas, silicon contained in the resists oxidizes, drastically slowing down the etch rates of the polymers. This is in stark contrast to organic polymers, notably PMMA, and bilayer lithography is a common utilization of such material systems.[36-38]

Compositions investigated in this work include poly(dimethyl siloxane)-polystyrene diblock copolymer (PDMS−*b*−PS), poly(dimethyl siloxane)-graft-poly(methyl acrylate)-co-poly(isobornyl acrylate) (PDMS−*g*−PMIA), and poly(dimethyl siloxane)-graft-poly(methyl methacrylate) (PDMS−*g*−PMMA). This work will explore the novel applicability of these materials to the NIL process in comparison to PMMA homopolymer. Significant improvements in imprinting large area samples and reactive

ion etching (RIE) resistance have been demonstrated. Coating, printing, and etching of the new polymers will be presented, with particular attention to the critical performance issues covered in the introduction. Copolymers were provided by Fu, and details of the synthesis are listed in Appendix A.[39]

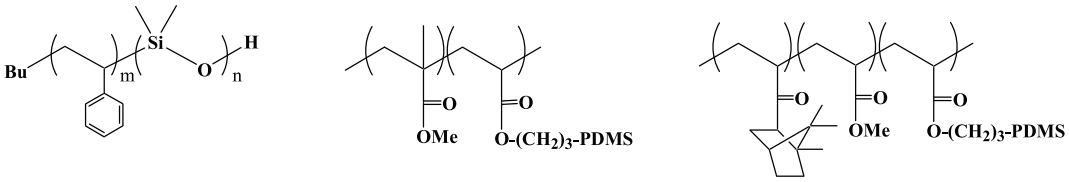


Figure 2.1: PDMS–*b*–PS, PDMS–*g*–PMMA, and PDMS–*g*–PMIA.

## High Resolution Imprinting Performance

Resolution capabilities of the PDMS copolymer resist systems can be seen in Figure 2.2. The smallest feature size on the mold used in this study is 60 nm lines. The mold used to imprint is shown in Figure 2.2(A), which has 60 nm trenches at a 225 nm pitch in a silicon nitride layer on a Si substrate. Figure 2.2(B-D) shows the 72 nm features obtained in various siloxane copolymer resists. The dimensional discrepancy is due to some physical expansion of the resist structures after printing. The mold was vapor-coated with a perfluorinated monolayer to lower its surface energy.[15] The vapor-coating method followed by a thorough anneal produced a stable surfactant coating that did not require any maintenance beyond solvent cleaning during all imprinting tests. Refer to Appendix B for imprinting process details.

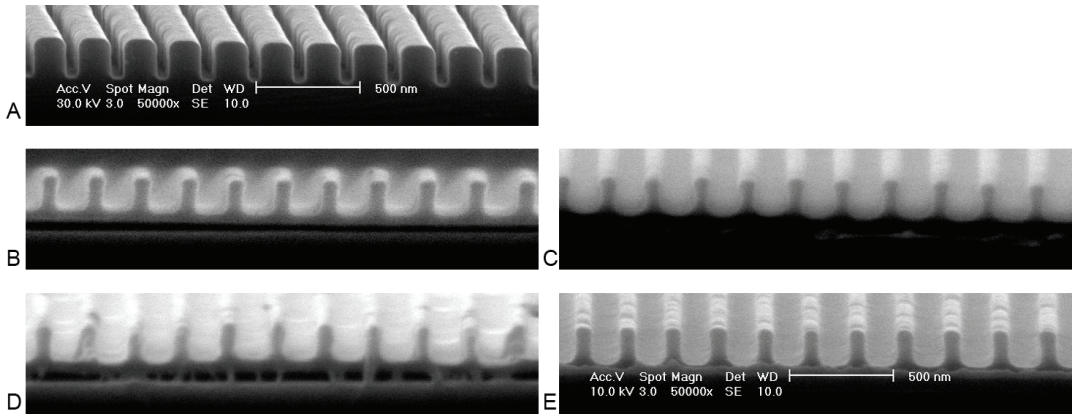


Figure 2.2: (A) the 60 nm feature mold used to imprint into (B-D), PDMS−*g*−PMIA, PDMS−*g*−PMMA, and PS−*b*−PDMS copolymers, respectively. (E) PDMS−*g*−PMIA imprinted at lower pressure and shorter time.

Cross-section scans shown in Figure 2.2(B-D) are each of PDMS−*g*−PMIA, PDMS−*g*−PMMA, and PS−*b*−PDMS copolymers. The copolymers were dissolved in PGMEA and spin-coated onto clean silicon wafer substrates. It was found that 4% weight concentrations in solution produced approximately 100 nm films for each resist. After coating, the samples were thoroughly baked to remove any residual solvent, to prevent out-gassing during imprinting. Samples were then imprinted at 170 °C, 600 psi for 5 min. These imprint parameters are not restrictive, however; shown in Figure 2.2(E) is a sample of PDMS−*g*−PMIA resist that was imprinted at 170 °C, 200 psi for 30 sec. Processing parameters can be tailored to specific imprint feature sizes and aspect ratios. Although 60 nm features were the smallest available mold, it is reasonable to say that these resists can be patterned to even finer dimensions. Noticeably, the corner morphology of the graft siloxane copolymers exhibits much less rounding than that of the block copolymer, indicating the different rheological behavior between the two kinds copolymers under the imprinting conditions.

## Large Field Imprinting Performance

Figure 2.3 shows the large-area performance of the copolymers, revealing perfect adhesion to the substrate after mold-substrate separation. The mold used was a full 100 mm wafer with 100 nm line-width grating features. Figure 2.3(A) shows the mold on the left and the imprinted PDMS–*g*–PMIA surface on the right. Some defects on the original mold, apparent as spots, can be seen replicated in exact mirror position on the imprinted substrate. Figure 2.3(B) is a photograph of blue light diffraction from the periodic gratings imprinted into the PDMS–*g*–PMIA when the sample was immersed in water. There was some distortion because the light must be viewed through an air-glass-water interface to be visible. Again, the intrinsic mold defect in the center is apparent as an absence of diffracted light in the center of the as-replicated grating field. In each of several successive imprints, there was no apparent gross-delamination of the copolymer, and as a result, no need for solvent rinsing between imprints.

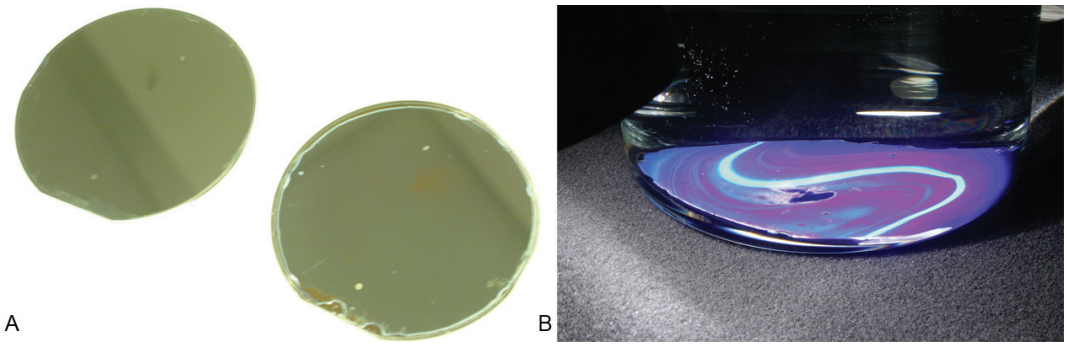


Figure 2.3: (A) 100 mm wafer mold, left, was imprinted into silicon substrate coated with PDMS–*g*–PMIA copolymer, right. (B) Strong diffraction of imprinted PDMS–*g*–PMIA copolymer.

Prior work has shown PMMA to have too strong of an adhesion force to the imprint mold to produce reliable demolding.[8-9] Because of this, large area performance may be difficult to obtain with the homopolymer. In prior experiments, the strong adhesion force when imprinting large areas (e.g. 100 mm wafer size) of dense 200 nm period grating structures using PMMA would cause either the mold or the

substrate to break during the mold-sample separation step. To quantify the advantageous release property given by the PDMS component, the forces required to demold PMMA and PDMS−*g*−PMIA were compared. The mean copolymer release force was 6.09 N/cm$^2$, while the release force for PMMA was 8.87 N/cm$^2$, which is almost 1.5 times greater.

## Etch Resistance

Etch rates for the copolymers in comparison to various other materials are shown in Table 2.1. Two $T_g$ were observed for PS−*b*−PDMS, corresponding to the glass transitions of polystyrene ($T_g$ = 100 °C) and polydimethylsiloxane blocks ($T_g$ = −127 °C), by DSC. The presence of two $T_g$ in the copolymer indicate polymer phase segregation, which was confirmed by TEM analysis (lamellae morphology with a periodicity of 35 nm for THF cast film and 17.4 nm for microtomed film), as detailed in Appendix A. Etch rates of the polymers in fluorine plasma were all roughly equivalent. However, there was a large contrast in etch rates in oxygen plasma. PS−*b*−PDMS, with the highest concentration of silicon, showed the lowest $O_2$ RIE rate, giving it a 13:1 contrast to $CHF_3$ RIE, and a >100:1 selectivity to PMMA in oxygen plasma. This behavior was expected for PDMS-containing polymers.[38] PDMS−*g*−PMMA and PDMS−*g*−PMIA, both with lower concentrations of silicon, had correspondingly lower resistances to $O_2$ RIE. The relatively lower etch rate of PDMS−*g*−PMIA compared to PDMS−*g*−PMMA at equivalent silicon contents can be attributed to the high C/H ratio of the isobornyl group.

| Polymer | Si by wt% | $T_g$ (°C) | $CHF_3$ (nm/min) | $O_2$ (nm/min) |
|---|---|---|---|---|
| **PS–*b*–PDMS** | 18.92 | −127, 100 | 13 | 0.98 |
| **PDMS–*g*–PMIA** | 7.57 | 54-64 | 19 | 18 |
| **PDMS–*g*–PMMA** | 7.57 | 105 | 26 | 29 |
| **PDMS** | 37.84 | −127 | 26 | 1.2 |
| **PMMA** | 0 | 105 | 20 | 110 |

Table 2.1: Etch rates of copolymer NIL resists in comparison to other materials. Parameters were 20 sccm $CHF_3$, 20 mtorr, 150 W; 20 sccm $O_2$, 5 mtorr, 50 W.

## Dual Layer Resist Process

High selectivity to PMMA makes the siloxane copolymer resists ideal materials to be used in bilayer NIL, similar to traditional bilayer photolithography.[37] Figure 2.4 shows SEMs of the original mold features, (A), and the use of the mold to pattern features on the substrate, (B, C). Figure 2.4(A) shows the grating features of the 100 mm mold used in the whole-wafer imprint shown in Figure 2.3. The substrate was coated with 100 nm of high molecular weight PMMA to serve as the under-coating layer, followed by 100 nm of PDMS–*g*–PMIA resist. The high molecular weight PMMA has a slow dissolution rate to minimize intermixing when the NIL resist is applied. However, a small degree of entanglement is expected at the interface, which helps to improve the adhesion. After imprinting, there was a thin, 30 nm residual layer of resist. If the imprint polymer layer is thin enough, a zero residual layer result can be obtained as in Figure 2.5. The 30 nm residual layer was etched in a $CHF_3$ RIE, followed by a through-etch of the under-layer in 5 mtorr $O_2$ RIE without breaking vacuum. Such low pressure is necessary to minimize PMMA undercutting at these small feature sizes. The $O_2$ RIE was applied well beyond the time required to etch through the under-layer to ensure that the exposed substrate surface was thoroughly cleaned by the plasma. In this case, the $SiO_2$ substrate was not harmed by the $O_2$ RIE; this further supports the use of an under-layer rather than

etching the resist directly atop the substrate, whereby the residual etch would adversely affect the oxide.

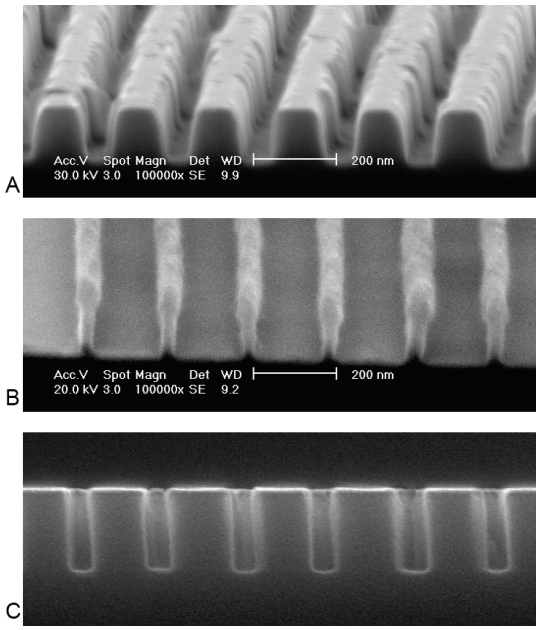


Figure 2.4: (A) 200 nm period mold used to imprint. (B) Pattern after PDMS–*g*–PMIA residual layer and PMMA under-coating layer were etched. (C) Reproduced new mold after all lithography and oxide plasma etching.

Figure 2.4(B) shows the substrate after the $O_2$ RIE step. Resist features at this point consist of a PDMS–*g*–PMIA copolymer "cap" on top of a PMMA "stem". The vertical side-wall of the PMMA is evidence for very little copolymer degradation during the $O_2$ RIE. Much of the inherent line-edge roughness from the mold, Figure 2.4(A), was mitigated by the residual etch. The lateral width of the resist lines correlates to the narrow width of the bottoms of the mold trenches. Such a bilayer resist approach can be used to create very high aspect-ratio structures, in this case 3:1. A 20 nm thick nickel layer was evaporated onto the substrate following a 5 nm titanium layer (for adhesion), and then lift-off was performed by dissolving the PMMA under-layer in acetone. The slight undercut profile of the resist in Figure 2.4(B) is very advantageous for lift-off processing such as this. The substrate was then treated to a short $O_2$ RIE to descum any remaining PMMA, and then, without breaking vacuum, a low-pressure $O_2$ RIE. The Ti/

Ni hard-mask was then stripped in a 1:1 $H_2SO_4$ (conc.):$H_2O_2$(30%) ("Piranha") solution. The resulting structure is shown in Figure 2.4(C). The hard-mask coupled with a low-pressure oxide RIE produces vertical side-walls, unlike the angled side-walls in the original mold in Figure 2.4(A). The duty cycle of this new structure corresponds to the duty cycle of the bottoms of the features of the original mold. This process demonstrates the utility of the copolymer NIL resists in nanolithography.

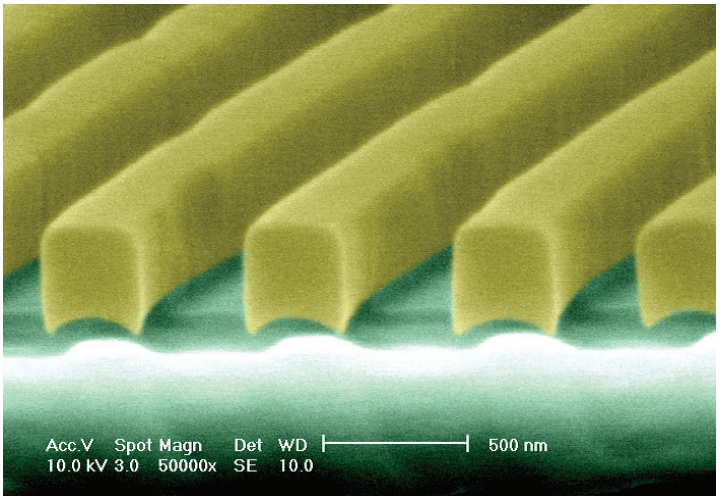


Figure 2.5: No residue layer left after imprinting, due to thin imprint copolymer layer. To highlight, the monochrome image has been tinted yellow for PDMS–*g*–PMIA and green for PMMA.

## Imprinting over Existing Topography

Figure 2.6 shows the bilayer resist approach used to pattern on top of existing topography. The same process was used as in Figure 2.4, but this time with PS–*b*–PDMS. A 350 nm line-width mold was used to lift-off metal lines. After the first lift-off was completed, the process was repeated in the orthogonal direction. The spin-coated PMMA under-layer served to planarize the non-flat substrate surface. Figure 2.6(A) shows the substrate after the second layer of metal was deposited but before lift-off. The

grid pattern of the combined metal layers is visible in the cross-section, above which is the resist mask covered with metal. Some cracks can be seen on the metal lines on top of the sacrificial resist due to the tensile stress as-deposited, but the top is otherwise level, demonstrating the utility of the copolymer resists in bilayer lithography. The resulting metal grid is shown in Figure 2.6(B) after the second lift-off step. The square dimensions of the crossed metal lines show that a consistent duty cycle was achieved in both steps.

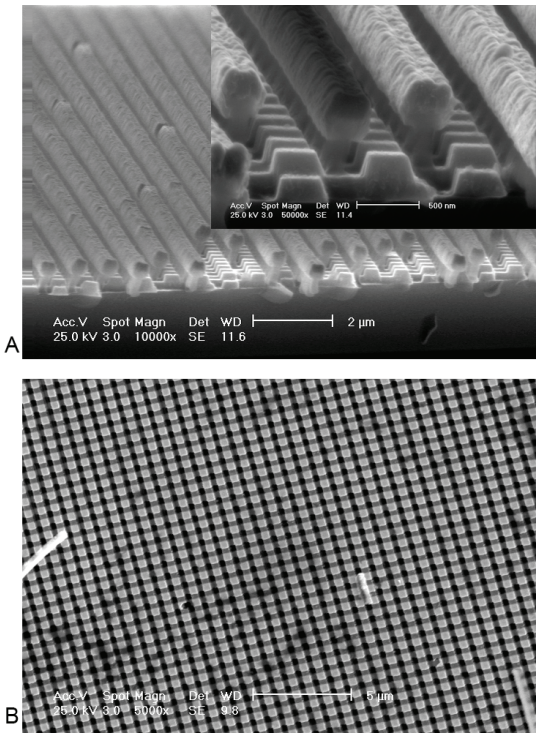


Figure 2.6: (A) Etch resistance of copolymers, in this case PS–*b*–PDMS, allows for complex patterning utilizing an under-coating layer to planarize. (B) Two layer metal grid deposited by two complete NIL steps.

## Nonhomogeneous Strain Relaxation

As previously mentioned, the copolymer resists exhibited some corner rounding, line-edge roughness, and feature width expansion. Among them, PDMS–*g*–PMIA had

the lowest incidence of roughness and the best corner morphology, and PS–*g*–PDMS exhibited the most roughness and rounded corners. This is possibly due to non-uniform stress relaxation in the bulk resist after pressure and the physical constraint of the mold were released. Further evidence for stress relaxation is the 20% feature width expansion of the resist lines. Relaxation of stress involves the rearrangement of polymer chains. Removal of the mold prior to sufficient stress relaxation permits the resist features to alter morphology. To overcome this problem, relaxation to room temperature and atmospheric pressure should be allowed to occur before demolding; however, the corresponding creep rates of plastic polymers at room temperature are quite long. Nevertheless, such relaxation can be induced in a reasonable time by raising the temperature. In order to test this hypothesis, imprinted copolymer resists were heated at 0 and 100 psi to 170 °C for 5 min, without demolding. After cooling again to 40 °C, the samples were demolded. Figure 2.7 summarizes these results. Figure 2.7(A) and (C) show imprinted PDMS–*g*–PMIA and PS–*b*–PDMS without annealing, respectively. The roughness was so severe in the case of 60 nm PS–*b*–PDMS features that entire void defects occurred along the lines. The roughness does not scale with feature size, such that large features (200 nm) do not have this problem, as shown in Figure 2.7(E). There was a great reduction in roughness after annealing, as seen in Figure 2.7(B) and (D). The 60 nm feature size of the mold was also accurately produced after annealing. PDMS–*g*–PMIA showed excellent feature reproduction (the mold used is that shown in Figure 3A), while the void defects in PS–*b*–PDMS lines were also minimized. Although the corner morphology is still better with the annealed PDMS–*g*–PMIA than with PS–*b*–PDMS, the improvements in both are significant nonetheless.

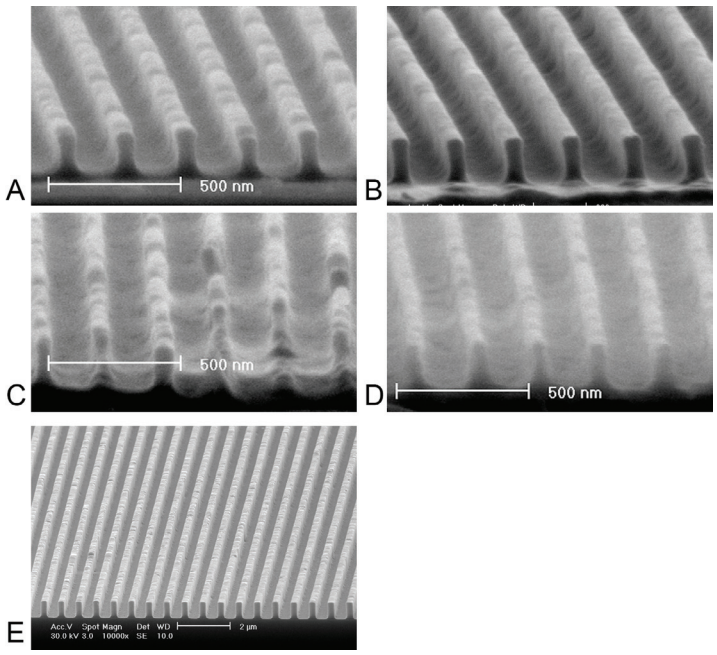


Figure 2.7: (A, C) PDMS–*g*–PMIA and PS–*b*–PDMS, respectively, after single imprint cycle showing roughness and expanded, 72 nm features. (B, D) Annealing at low pressure reduces roughness and gives 60 nm features. (E) PS–*b*–PDMS 200 nm features less prone to roughness.

While samples annealed at 0 and 100 psi showed equivalent improvements in pattern morphologies, the samples annealed without pressure suffered from dewetting in various places along the mold die. This was because the pressure is necessary to hold the mold and substrate in conformal contact, to overcome surface non-uniformities and particulate contamination. The dewetting problem was eliminated by annealing at 100 psi and taking care to minimize particulates in between the mold and substrates. While the copolymers exhibit non-uniform stress relaxation unlike homopolymers, such defects can be eliminated by this annealing step.

## Conclusions

Siloxane-organic copolymers have been shown for the first time to be an effective NIL resist material. The dual-surface properties of these copolymers provided superior mold-release performance without delamination—a critical problem facing the NIL area. Furthermore, these copolymers have high silicon content to give them excellent etch resistances, so they can be used as masks to facilitate further pattern transfer to underlying layers. Feature sizes of 60 nm, and possibly below, can be imprinted. Because NIL is a contact process, resists can contaminate the mold. Crosslinked resist systems by UV or thermal curing pose a danger in this regard due to difficulty when cleaning, so thermoplastic copolymers are safer, because any inadvertently contaminating material can be removed easily by dissolution.

In principle, any siloxane based copolymer with higher $T_g$ organic chains should produce a useful NIL resist. In particular, organic components with higher glass transitions ($T_g > 50$ °C) are necessary to compensate for the $T_g$ of siloxanes. The resists presented here are single-chain component systems, unlike non-homogeneous mixtures. Organo-siloxane graft copolymers, such as PDMS–*g*–PMIA and PDMS–*g*–PMMA, are preferred due to their higher degree of homogeneity (less phase segregation) and ease of synthesis.

# CHAPTER III

## Predicting Liquid Dewetting on Immersed Nano-structured Surfaces

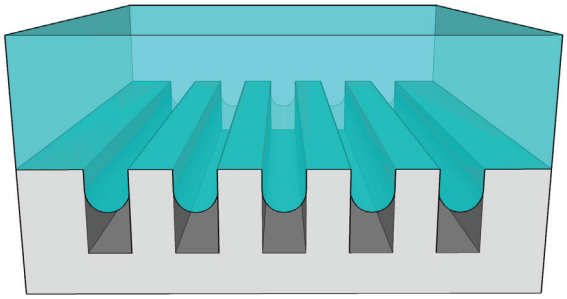

Figure 3.1: Hypothetical Cassie-mode wetting state on a grating structure, under applied pressure.

Following Marmur, Nosonovsky, and Tuteja, an analytical methodology has been developed to calculate total surface free energy at a heterogeneous, or three-phase, solid-liquid-air Cassie-mode wetting interface to predict what combinations of solid surface morphology, and solid and liquid surface energies will produce stable states.[53, 56, 59-62] Two cases are presented: one where the derivation is carried out across the two dimensions of a grating pattern cross section, with the third dimension extending without change in morphology for all phases, and another where the cross section is of cylindroid surface cavities.

## Derivation of Free Energy Calculation for Gratings

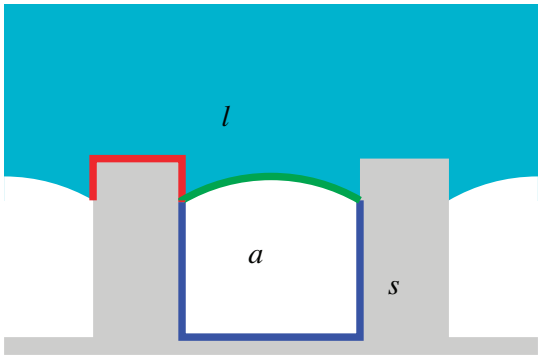


Figure 3.2: Three-phase wetting state with each distinct interface highlighted.

Given a known grating surface geometry, the solid-liquid and solid-air interfacial areas are trivial to calculate as they are simply the contour integral of the parameterized solid surface. Because it is part of a solid surface, this contour data is assumed fixed and unchanging. The liquid-air interfacial area is found by assuming a cylindrical arc form extending across the solid to solid gap, satisfying Young's equation at the solid-liquid-air triple point, as shown in Figure 3.3.

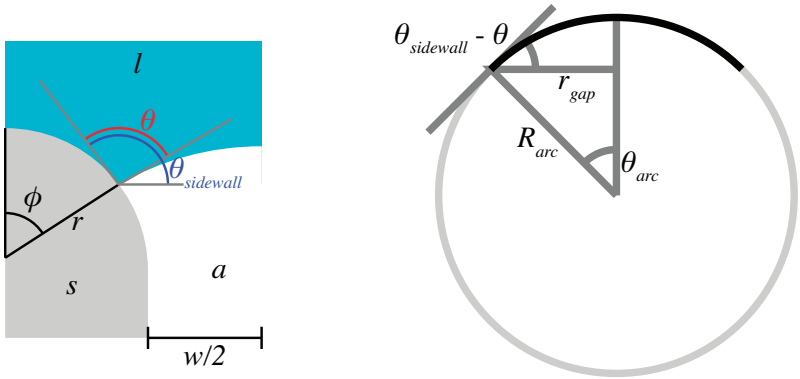


Figure 3.3: The solid-liquid-air triple point where Young's equation is satisfied. Right: arc length geometry in relation to the triple point angle and gap width.

$$A_{la} = \theta_{arc} R_{arc} = \frac{r_{gap}(\theta_{sidewall} - \theta)}{\sin(\theta_{sidewall} - \theta)} \tag{3.1}$$

Given a known contact angle and sidewall profile, the arc length can be calculated from the difference in sidewall tangent and contact angles as well as the local width of the gap. Combine Young's equation with the free energy equation to get Equation 3.2. This step adds the Young contact angle $\theta$ to the equation while removing the $\sigma_{sl}$ term. This is useful for two reasons: standard data is abundant for solid and liquid free energies (or, essentially, interfacial energy with air), and the contact angles of liquids on solids can be easily measured.[11, 66-68] In fact, $\sigma_{sl}$ is normally derived from known $\sigma_s$ and $\sigma_l$ values, along with measured $\theta$.

$$\begin{aligned} G_{cell} &= \sigma_{sl}A_{sl} + \sigma_{sa}A_{sa} + \sigma_{la}A_{la} \\ \sigma_{sa} &= \sigma_{sl} + \sigma_{la}\cos\theta \\ \Rightarrow G_{cell} &= (\sigma_{sa} - \sigma_{la}\cos\theta)\,A_{sl} + \sigma_{sa}A_{sa} + \sigma_{la}A_{la} \end{aligned} \tag{3.2}$$

Further simplify the free energy per cell $G_{cell}$ by setting an arbitrary zero point corresponding to a "dry" or Cassie state at the uppermost point on the sidewall profile. $A_{sl}$ and $A_{sa}$ are codependent quantities, and so one can be expressed as the other. That is, $A_{sl}$ during full Wenzel mode is equal to $A_{sa}$ before any wetting occurs, and the two interfacial areas always sum to these extremes. Arrive at Equation 3.3, where $A_{la}$ is the arc length as shown in Equation 3.1, $A_{sl}$ is the contour integral of the parameterized sidewall profile in contact with the liquid. Parameters $w$ and $\phi$ are as indicated in Figure 3.3.

$$
\begin{aligned}
G* &= G_{cell} - G_{dry} \\
&= \left(\sigma_{sa} - \sigma_{la}\cos\theta\right) A_{sl} + \sigma_{sa} A_{sa} + \sigma_{la} A_{la} - \left(\sigma_{la} A_{la,dry} + \sigma_{sa} A_{sa,dry}\right)
\end{aligned}
$$

$$
A_{sa} - A_{sa,dry} = A_{sl}
$$

$$
\Rightarrow \frac{G*}{\sigma_{la}} = A_{la} - A_{la,dry} - A_{sl}\cos\theta
$$

$$
\Rightarrow G* = \sigma_{la}\left(\underbrace{\left(r + \frac{w}{2} - r\sin\phi\right)\frac{\pi - \phi - \theta}{\sin\left(\pi - \phi - \theta\right)}}_{A_{la}} - \underbrace{r\phi}_{A_{sl}}\cos\theta - \underbrace{\left(r + \frac{w}{2}\right)\frac{\pi - \theta}{\sin\left(\pi - \theta\right)}}_{A_{la,dry}}\right)
$$

3.3

$G^*$ takes as parameters the liquid surface tension in air, the liquid contact angle on the unpatterned solid, and the spatial surface nanostructure shape. This equation has been derived to work in tandem with experiment, such that the well known $\sigma_{la}$ can be used for pure liquids in controlled ambient, and the contact angle $\theta$ can be measured on control samples. The surface nanostructure can be imaged with high resolution SEM and traced to parameterize the shape.

### Analysis Applied to Hypothetical Grating Nano-structures

Using this analysis, the varying $G^*(n)$ free energy can be calculated for the situation of a liquid meniscus transitioning from a Cassie to Wenzel mode wetting state, as illustrated in Figure 3.4, where $n$ is the position of the triple point along the sidewall. The resulting calculation is shown in Figure 3.5.

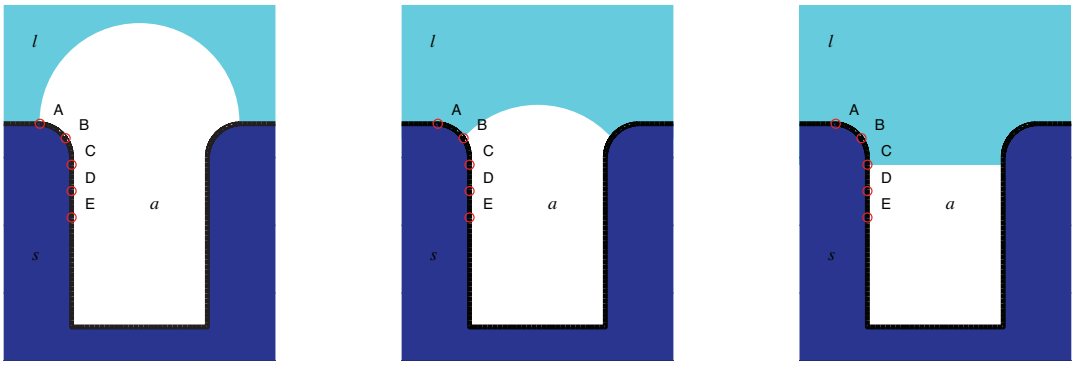


Figure 3.4: Liquid, which forms a contact angle $\theta = 90°$, begins to transition from Cassie towards Wenzel wetting states. The liquid-air interface area can change rapidly.

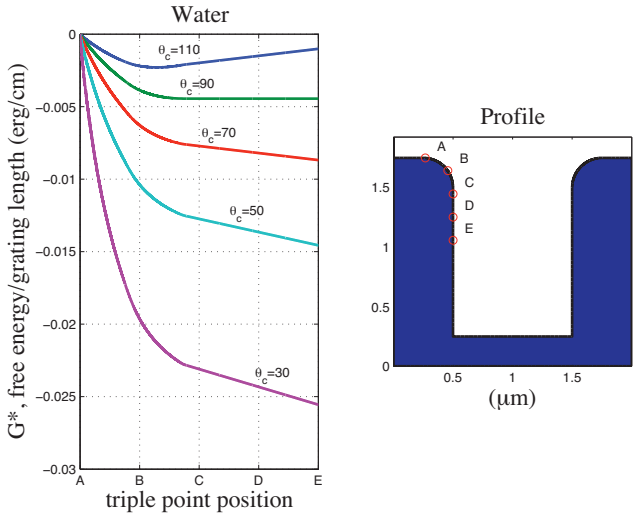


Figure 3.5: Interfacial free energy for water wetting a surface with contour as shown on the right. The free energy has been plotted for several different possible contact angles $\theta$ based on changing $\sigma_s$.

Contact angle is a sensitive variable in the free energy calculation, so modifying the surface with different molecular coatings to create different $\theta$ with a fixed liquid can yield fundamentally different $G^*(n)$ curves. In the left side of Figure 3.5, a set of five free energy curves are plotted based on the triple point position in transition from Cassie to Wenzel states. All five curves begin with $G^*(\mathrm{A}) = 0$ arbitrarily at triple point A. Local minima in the $G^*$ curves indicate stable triple point locations, because energy is required to move the contact line in to or out of the minima. For example, given a surface of contact angle $\theta = 110°$, a minimum exists near point "B", indicating a stable Cassie mode

wetting state. If the solid surface was an imprint mold and the liquid was imprint resist, the large energy barrier seen going into the structure gap would possibly prevent proper molding during imprinting. Solids forming contact angles of $\theta = 30°, 50°, 70°$, or $90°$ do not have local minima so it is predicted that such situations will readily transition from Cassie to Wenzel wetting modes. In other words, these configurations of mold and resist interfacial tension will lead to proper wetting of imprint molds. Calculations were performed in MATLAB software using a custom script. The grating script can be found in Appendix C.

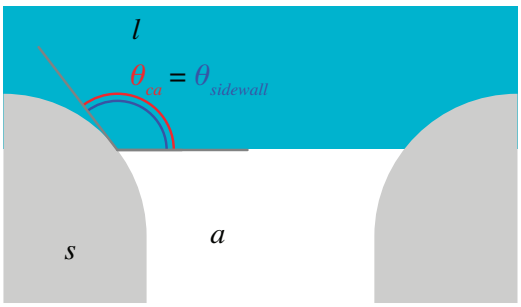


Figure 3.6: $G^*_{\min}$ occurs approximately when sidewall angle equals contact angle.

Comparing to published conclusions in the literature, simple tapered, flared, or straight sidewall profiles show the efficacy of the grating calculation routine. The lowest free energy $G^*(n)$ occurs approximately when the liquid-air interface forms a horizontal meniscus. Sidewall angle is measured in a polar coordinate fashion from the horizontal plane, such that the flat surface has a sidewall angle defined as 180°, and vertical trenches have sidewall angle 90°. Thus, in Figure 3.7, the sidewall angle from A to E changes from 180° to 120°. All liquid-solid combinations forming contact angles $120° < \theta < 180°$ will form flat menisci at locations between A and E when the sidewall angle equals $\theta$. This encompasses perfectly to "moderately" flat-surface dewetting combinations. All other $\theta$ combinations will not find local minima, and the $G^*(n)$ function will be monotonically decreasing. This means that those combinations of liquid and solid will readily transition from Cassie to Wenzel wetting states.

In Figure 3.8, the sidewall angle varies from 180° to 60°. All but moderately wetting liquid-solid combinations will readily transition to Wenzel states for this surface

morphology, and for $\theta > 60°$, stable Cassie states can be achieved. This is the general consensus of Marmur, Nosonovsky, and Tuteja.

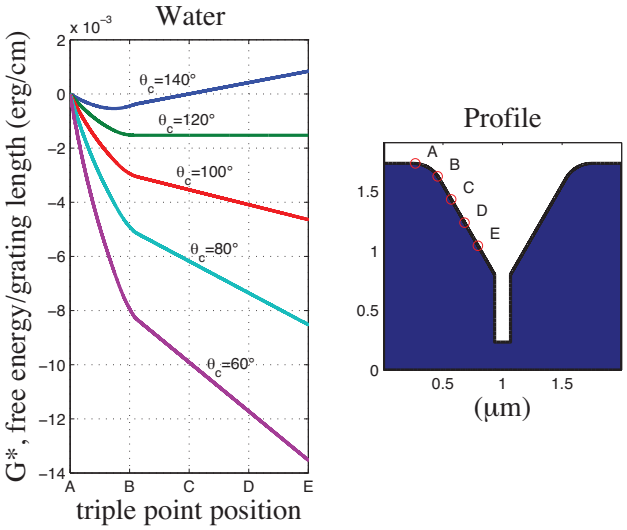


Figure 3.7: Tapered structure with critical $\theta = 120°$.

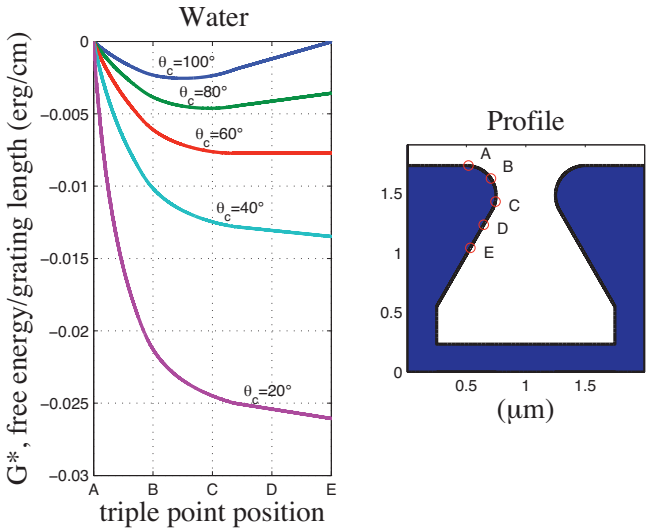


Figure 3.8: Tapered structure with critical $\theta = 60°$.

## Meniscus to Sidewall Collisions

Comparison to Nosonovsky is possible with similarly drawn parameter curves. [69] Reproduced in Figure 3.9, Nosonovsky graphed similar interfacial free energy plots as functions of triple point positions. Two such analyses were published and similar curves are plotted in Figure 3.10 using the methodology developed here. Nosonovsky's abscissa axis markers 0 through 3 correspond precisely with sidewall markers A through D in Figure 3.10. $G^*(n)$ for the wave structure on the left half of Figure 3.10 shows a marked disagreement with Nosonovsky's result near location C or 2. At C-2, a liquid forming a large contact angle of 150° would form a meniscus that points further into the solid wall towards D-3. The ultimate shape of the meniscus across the gap is not straightforward and in fact fails a simple analysis: the meniscus would collide with the sidewall again. This essentially means that the triple point cannot exist in the region from approximately C-2 downwards. In effect, neither results are really valid or useful. The bead structure on the right half of Figure 3.10 shows better agreement with Nosonovsky. However, in this situation as well, the sidewall shape would cause an encroaching meniscus to collide with the sidewall in the vicinity of point C-2. The asymptotic minima that occur in Figure 3.10 at C are a consequence of the fact that the continuous sidewall must pass through angle $\theta$ as it abruptly changes from 0° to 180° angle. But, again, neither result is truly valid near point C-2.

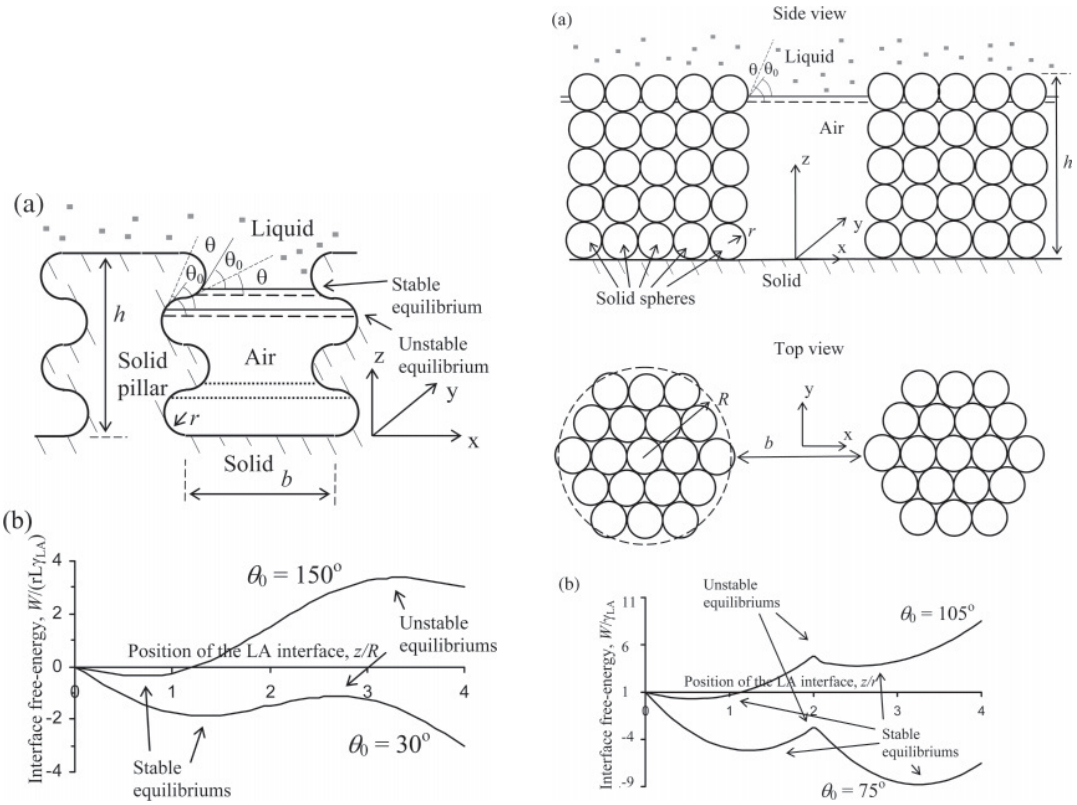


Figure 3.9: Nosonovsky's analysis of hypothetical wave and bead structures. Reproduced from [69].

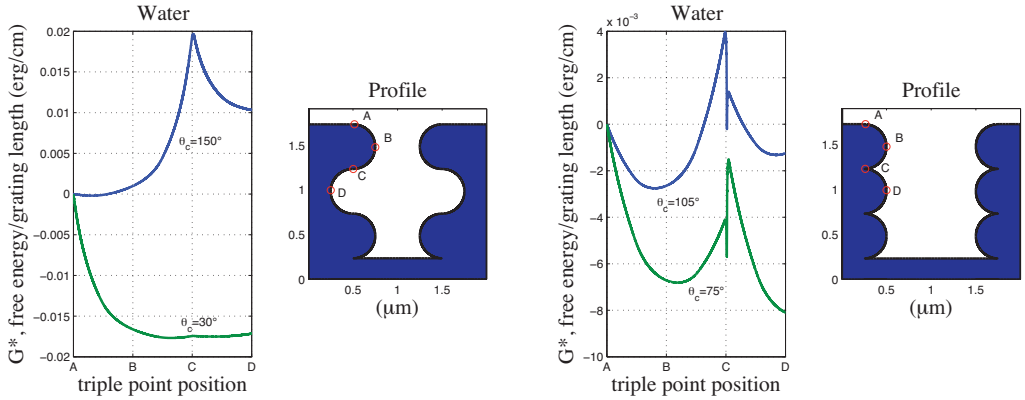


Figure 3.10: Grating analysis of similar ridge and bead structures to Nosonovsky, Figure 3.9.

Tuteja's treatment of meniscus collision is the most thorough in the literature.

[60-61] As $\theta > 90°$ liquids transition from Cassie to Wenzel state wetting, the bottoms of

the intruding menisci will make early contact with the bottoms of the surface micro-cavities. When the cavity depth is on the order of half the cavity width, this contact can occur when the triple point is only a fraction of the way down the sidewall. Tuteja *et al.* take into account these geometries in their mathematical robustness and design parameters to optimize the surface cavity geometries of their dewetting surfaces.

### Negative Angle Sidewalls

Because contact angles are limited to the domain $0° < \theta < 180°$, if the cavity sidewall transitions fully from 180° to 0° or < 0°, all liquid-solid combinations will encounter some stable, energy minimizing, triple point location somewhere along the sidewall. Figure 3.11 illustrates this calculation. For a surface to resist wetting even by the lowest surface energy fluids, such a morphology could be designed and implemented. This is similar to structures proposed by Tuteja.[61]

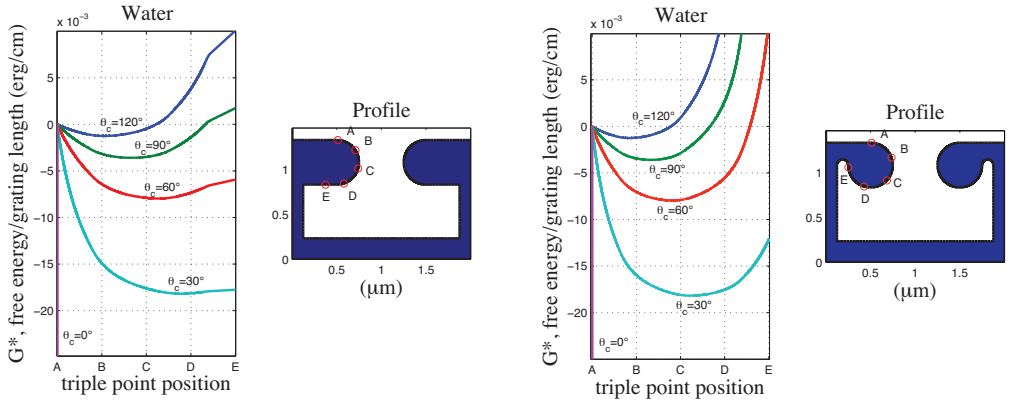


Figure 3.11: 0° and −90° angle sidewall structures.

**Derivation of Free Energy Calculation for Cylindroids**

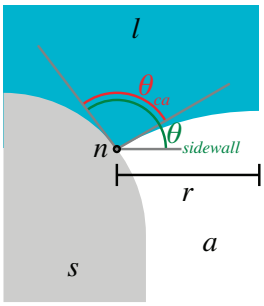


Figure 3.12: Triple point location $n$ and $r(n)$ cavity radius.

Modifying the grating model to calculate $G^*$ for cylindrical cavity openings on a surface is done by treating the meniscus as a dome rather than a cylinder, and the $A_{sl}$ and $A_{sa}$ areas as series of differential cylinders of radius $r(n)$. Equation 3.4 shows this modification. This equation is more generalized than Equation 3.3, and relies on two-dimensional parametric position data for points $n$, as well as the local slope or $dy_n$ / $dx_n$. The computation of these is within the script in Appendix D.

$$G^*(n) = \sigma_{la} \underbrace{\pi r^2 \left(1 + \tan^2 \frac{\theta(n)_{sidewall} - \theta_{ca}}{2}\right)}_{A_{la}} - \sigma_{la} \cos\left(\theta(n)_{sidewall} - \theta_{ca}\right) \underbrace{\int_0^n 2\pi r(m) dm}_{A_{sl}} - G_0 \tag{3.4}$$

Additionally, the capillary pressure $P_{liquid}$ can be calculated at all triple point locations. This is shown in Equation 3.5. Figure 3.12 identifies the triple point location $n$ and $r(n)$ cavity radius.

$$P_{liquid} = -\frac{2\sigma_{la}}{r_{meniscus}}$$
$$\Rightarrow P(n)_{liquid} = -\frac{2\sigma_{la}\sin\left(\theta(n)_{sidewall} - \theta_{ca}\right)}{r(n)} \quad 3.5$$

Calculations were again performed in MATLAB software using a custom script. The cylindroid script can be found in Appendix D. The resulting calculation is shown in Figure 3.13. Similar to the grating $G^*(n)$ calculation, all $\theta$ liquids encounter a stable energy minimum at some location on the sidewall $n$. The sidewall profiles are made identical in both plots from A to D to highlight the differences caused by the −90° sidewall from D to E. Thus, the trends for both the 0° and −90° sidewalls are identical until the $\theta_{sidewall} = 0°$ point, D. An inflection point (change in $d^2G^* / dn^2$) is noticeable for the 0° sidewall, causing $G^*(n)$ curves to rise less rapidly than the −90° plot. All $\theta > 0°$ free energy curves have minima somewhere between A and D, and the −90° introduces deeper minima for low $\theta$ systems. For $\theta = 130°$, the minimum is point A: such high contact angle liquid menisci will rest at the entrance to the cavity. For $\theta = 90°$, free energy is approximately constant from A to C: such medium contact angle liquid menisci will be located somewhere between A and C in the vertical portion of the cavity. Wetting liquids of $\theta = 50°$ have minima approximately halfway between C and D: the menisci will readily wet through the cavity and part way around re-entrant features. Strongly wetting liquids of $\theta = 10°$ have shallow minima located just before D, or moderately deep minima in the case of the −90° sidewall: such liquids will readily wet most of the way through the cavity opening.

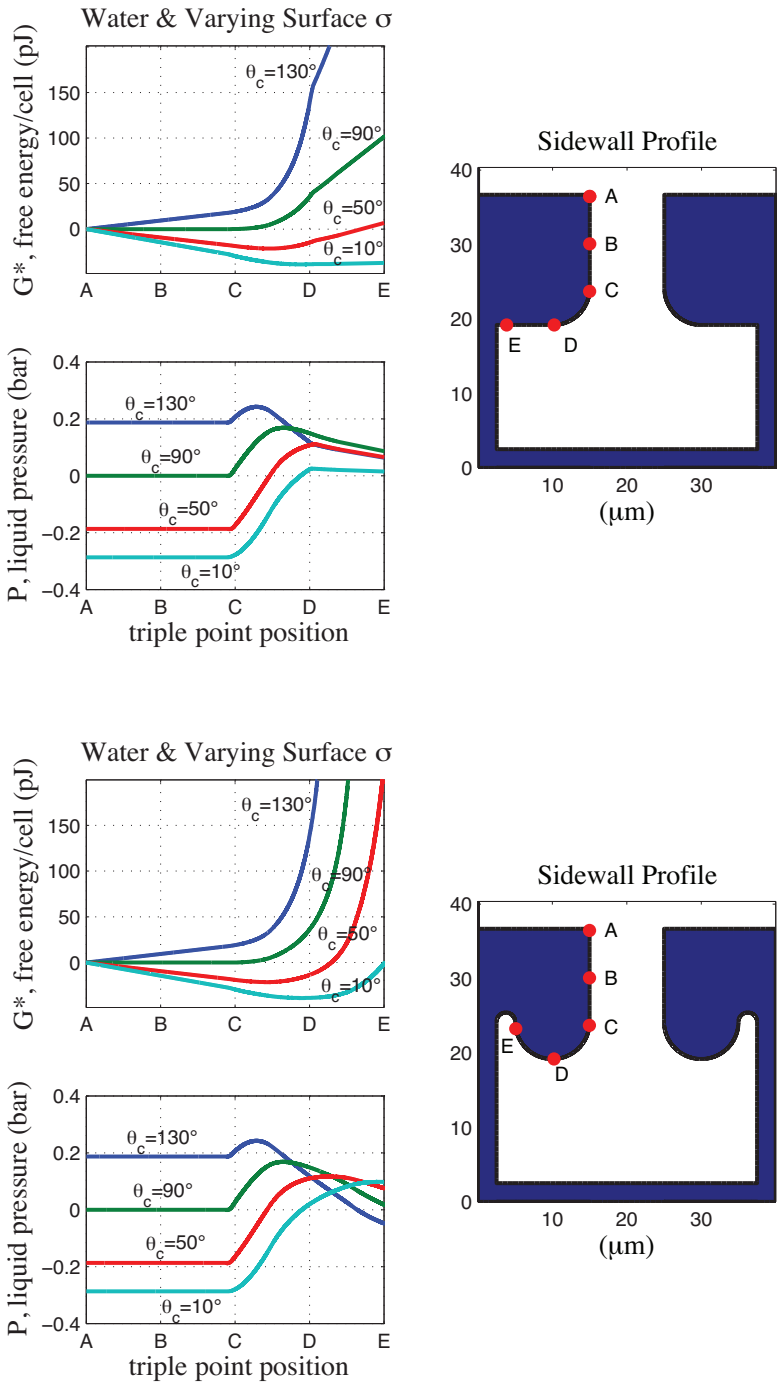


Figure 3.13: 0° and −90° angle sidewall structured cylindrical cavities.

## Equilibrium Meniscus Pressure

During NIL, small external pressures are applied to drive the low viscosity resist precursor into the mold features. Because of this, the effect of liquid pressure on the triple point position is studied. Equation 3.5 shows the derivation of this pressure. It is essentially the capillary pressure which takes surface energy and radius of curvature as parameters. The surface energy term is assigned based on liquid type, and the radius of curvature of the meniscus dome is calculated based on the angle $\theta(n)_{sidewall} - \theta$ and the local cavity radius $r(n)$. The consequence of this calculation is that the meniscus radius varies from $r(n)$ to $\infty$. This means that $|P|$ will be tend to be maximum when $|\theta(n)_{sidewall} - \theta| = 90°$, although $r(n)$ is a confounding variable, and zero when $\theta(n)_{sidewall} = \theta$. Zero pressure thus corresponds nearly exactly with the flat membrane condition for $G^*_{\min}$. In Figure 3.13, the minima of $G^*$ correspond to the zero cross-overs of $P$.

Pressure maxima, however, do not correlate to points of interest on the free energy graph. However, interpretation of the $P(n)$ graph can yield yet another understanding of the liquid-solid system, this time in a dynamic fashion. The reason for the non-correlation has to do with when and where static equilibrium occurs. For this interpretation, it is necessary to decouple $P(n)$ and $G^*(n)$. In $G^*(n)$, free energy has been plotted for hypothetical triple point locations $n$, and zero external applied pressure. Minima in $G^*(n)$ indicate regions where the triple point may find a stable equilibrium. These $n$ points act as attractors to the dynamic situation of liquid wetting the solid surface. All other $n$ locations where $dG^*(n) / dn \neq 0$ and $d^2G^*(n) / dn^2 < 0$ are unstable triple points, and the unavoidable minute perturbations of the natural system will cause the triple point to move to a location with lower $G^*$.

Application of pressure to the liquid can, however, stabilize the triple point location at certain $n$. What is graphed in $P(n)$ is the required liquid pressure to maintain equilibrium at given locations $n$. Because $G^*$ is calculated based on the condition that $P = 0$, correlation between $P(n)$ and $G^*(n)$ can only be made when $P$ crosses the abscissa. Thus, $P(n)$ indicates for $\theta = 90°$ that no external pressure is required for the triple point to

easily move from A to C. During this time, the liquid meniscus is flat. Beyond C, positive liquid pressure is required to move the triple point towards D. The application of positive pressure will cause a convex meniscus bowing, and a non-zero force upon the liquid meniscus, as shown in Figure 3.14. The meniscus will then move due to this force, towards D. Equilibrium is reestablished when the Young's contact angle formed at the sidewall creates a meniscus dome radius whose capillary pressure equals the applied pressure $P$. $P_{max}$ is approximately 0.16 bar and occurs just past the halfway point between C and D. If this pressure is applied, the liquid meniscus radius would be at its minimum, balancing the applied pressure with high capillary pressure. The meniscus would form an approximately 45° angle with horizontal. The reason why the pressure maximum is not at D, where the meniscus would be a hemisphere, is because the cavity radius $r(n)$ begins to increase from C onward. The confounding $r(n)$ variable is significant when the radius of curvature of the sidewall is approximately equal to $r$. Therefor balance between increasing $r$ and increasing $\sin(\theta(n)_{sidewall} - \theta)$ is struck part way between C and D. Beyond this maximum, $P(n)$ decreases.

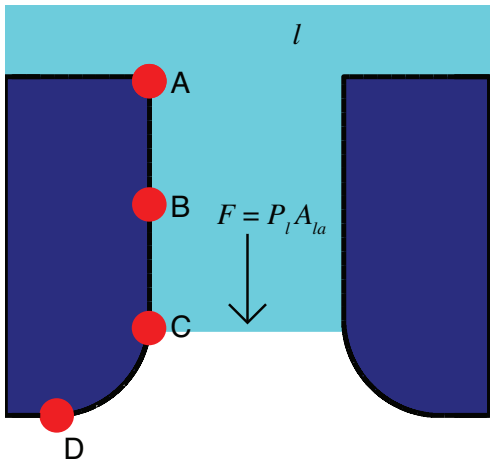


Figure 3.14: Application of pressure will cause the liquid meniscus to move until equilibrium is reestablished.

However, the negative $dP$ / $dn$ has profound implications. If the triple point is located at D, for example, and a perturbation causes liquid pressure to increase, the system would no longer be in equilibrium. Non-zero, forward pressure would be applied

to the meniscus because its radius of curvature would be insufficient to provide equal and opposite restorative pressure. Because the equilibrium meniscus pressures at all locations downward into the cavity from D imply decreasing pressures, the forward pressure will never encounter resistance, and thus readily wet the entire cavity. Inasmuch, regions of $P(n)$ where $dP / dn < 0$ are unstable triple point locations. As soon as the pressure is raised above $P_{max}$ or "breakthrough", the liquid will transition to the Wenzel state.

For $\theta = 130°$, positive external pressure is required for the triple point to enter the cavity beginning at point A. If the requisite pressure is applied, a convex meniscus bowing occurs, moving into the region between A and C. Even greater positive pressure is required to force the liquid towards point D. Beyond this maximum, liquid will transition to Wenzel state.

For $\theta = 50°$, the liquid will readily enter the cavity until the zero pressure point part way between C and D. This corresponds to the free energy minimum in the same location on the graph $G^*(n)$ and a flat meniscus condition. To prevent the liquid from readily flowing inward, negative external pressure is required. Approximately –0.18 bar is required to maintain the triple point at some location between A and C. If this pressure is reduced, the triple point will migrate to a location between C and the zero pressure point corresponding to the exact amount of negative pressure applied. Between A and C, a concave meniscus bowing occurs, exactly balancing the applied negative pressure $P$. Beyond the zero pressure point between C and D, positive pressure is required to force the liquid in further. The flat meniscus changes to a convex shape and balances this pressure.

For $\theta = 10°$, the liquid will readily enter the cavity until the zero pressure point just before D. This corresponds to the free energy minimum in the same location on the graph $G^*(n)$ and a flat meniscus condition. To prevent the liquid from readily flowing inward, negative external pressure is required. Approximately –0.29 bar is required to maintain the triple point at some location between A and C. If this pressure is reduced, the triple point will migrate to a location between C and the zero pressure point corresponding to the exact amount of negative pressure applied. Beyond the zero pressure point just before D, positive pressure is required to force the liquid in further. There is a major difference in this required pressure between the 0° and –90° sidewall

structures. For the 0° sidewall, the required positive pressure to force liquid through peaks at approximately 0.04 bar, whereas for the −90° sidewall, the required pressure continues to increase before leveling out and peaking at E at approximately 0.1 bar: more than double.

This positive pressure barrier is the key differentiator between the 0° and −90° sidewall structures. In the 0° sidewall structure, $P(n)$ predicts diminishing forward pressures required to prevent low $\sigma$ liquids from wetting into the cavity and transitioning to the Wenzel state. However, for −90° sidewalls, the required pressure to force wetting liquids into the cavity does not diminish as rapidly with $\theta$. Finally, to compare the two methods, whereas the $G^*(n)$ graphs show energy minima for low $\theta$ fluids, the $P(n)$ graphs better quantify what pressures are needed for liquid to transition from Cassie to Wenzel states. This pressure information is useful in the context of capillary pressure. When a small enough droplet of liquid is placed on a micro-structured surface, the droplet exerts pressure on the liquid-air interfaces that form the composite Cassie wetting state, pushing the liquid towards Wenzel mode.

This pressure information is also useful in the context of NIL. For the length scales plotted in Figure 3.13, the forward pressure barriers to engage Wenzel mode wetting were on the order of tenths of a bar: 0-30 kPa or 0-5 psi. However, if the feature size is reduced to the lengths typically used in NIL, two or three orders of magnitude less, the pressure increases to significant amounts. As shown in Figure 3.15, for a 50 nm diameter cavity, the forward pressure to force water into the pore of a $\theta = 130°$ surface would be 37.4 bar: 3.74 MPa or 543 psi. This magnitude of imprinting pressure exceeds most process designs for thermoplastic imprinting, and is far greater than the typical pressures used for crosslinking resists. High imprinting process pressures also stress the mold and substrate, and lead to resist distortion as discussed in Chapter II.

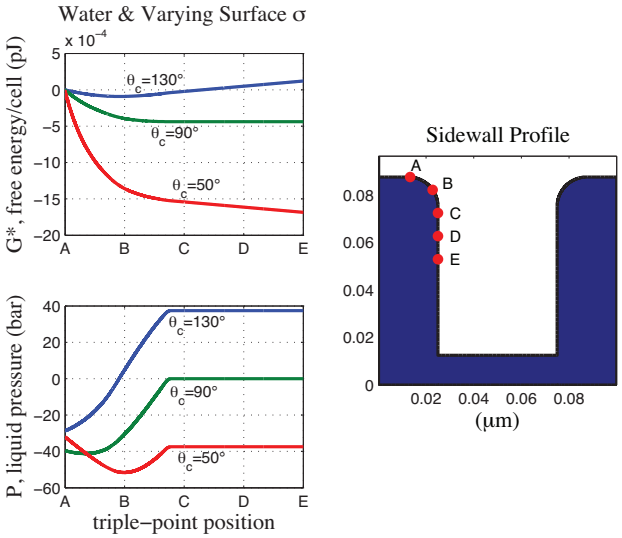


Figure 3.15: Cylindroid analysis of $P(n)$ for a structure at NIL length scales.

## Conclusions

Liquid wetting on grating and cylindroid patterned surfaces has been modeled using an *ab initio* interfacial free energy minimization method. The exact method of calculation is unique from the published literature, in that the microstructure profile is parameterized bitmap data to allow for maximum flexibility in modeling measured, sample surfaces. Additionally, wetting behavior has also been modeled by calculating equilibrium pressure gradients across the liquid-air interface. This method also utilizes parameterized data. Both methodologies have been verified against the well-accepted conclusions and wetting behaviors found in the establishment.

Equilibrium meniscus pressure calculations predict stable triple point locations in the same places as free energy minimization. Free energy calculations are useful for finding stable triple point locations and predicting equilibrium wetting conditions on micro-structured surfaces. However, this has limited utility in NIL where pressure is generally applied to minimize residual layer thicknesses and achieve proper resist wetting

of the mold. Meniscus pressure calculations establish non-zero liquid pressures that are necessary to move the triple point to any location on the sidewall and hold its position.

# CHAPTER IV

## Design and Fabrication of a Negative Sidewall Angle Pore Membrane

All the micro-structured surfaces modeled in Chapter III were examined well above the bottoms of the cavities, near the surface-side pores and gratings. The energy minima and hence conclusions about wetting behavior are all deduced based on the equilibrium free energy or meniscus pressures at these upper cavity locations. As such, liquid wetting of the bottoms of the cavities is ignored, and in fact have no effect on the wetting dynamics occurring above them. If, however, the bottoms of the cavities are removed, a free-standing (if cavity geometry permits) porous membrane would remain. The task of modeling the wetting behavior remains the same, by calculating $G^*$ or $P$ along the pore wall, from one side of the membrane to the other. Liquids not readily flowing through the membrane would be in a Cassie-like wetting state, and liquids flowing through would be in a Wenzel-like state.

Extending a dewetting surface microstructure to a negative sidewall angle pore membrane does require a shift in paradigm from cavity-field to surface-field design to have a self-supporting membrane. That is, natural and artificial dewetting surfaces are all comprised of physically discontinuous protrusions from the bulk of the solid, with continuous fields of recessed regions.[47-50, 52-54, 60-62] A continuous field design is reported by Ahuja.[55] Others have reported woven or spun fiber mat structures which are also self-supporting.[51, 58, 61, 70] Such fiber mats are durable and make effective pore membranes, and attempts have been made to accurately analyze their wetting and liquid penetration behavior, especially early on by Kim and Harriott.[58, 61-62, 71] As fabricated, however, the pore geometries of fiber mats are distributed over a range of sizes and geometries. The mats themselves are thick, and liquids penetrating them would follow an irregular, chaotic, tortuous path to the exit side. Also, the mats lack negative

sidewall structures because of the tubular structure or circular cross-section of the fibers themselves. Figure 4.1 illustrates the expected liquid wetting behavior through well-controlled membrane pore geometries.

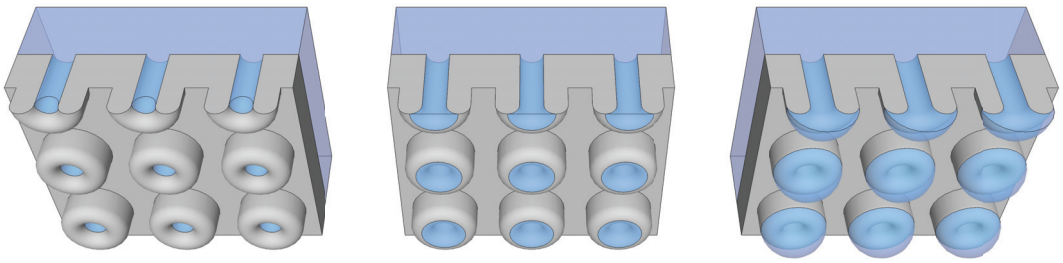

Figure 4.1: Cross-section view of wetting of a low $\theta$ liquid through membrane pores.

NIL is ideal for fabricating well controlled geometries and microstructures, and the process lends itself to three-dimensional or multilevel patterning more so than photo or e-beam lithography.[3,7] Using NIL to fabricate membranes has only recently been reported by Choi *et al*.[72] The use of SU-8 negative photoresist is as the membrane material, based on earlier work established by Hu, who reported planar tubules directly imprinted into SU-8, which itself is kept as the final structure instead of as an intermediary resist layer.[73] Earlier work by Cheng and Guo utilize SU-8 as a polymerizable thermoplastic resist layer in a combined thermal and UV imprint process. [74-75] Wang *et al*. report similar pore membranes fabricated using a sacrificial mold, but this process will utilize a reusable imprint mold and better morphology control.[76]

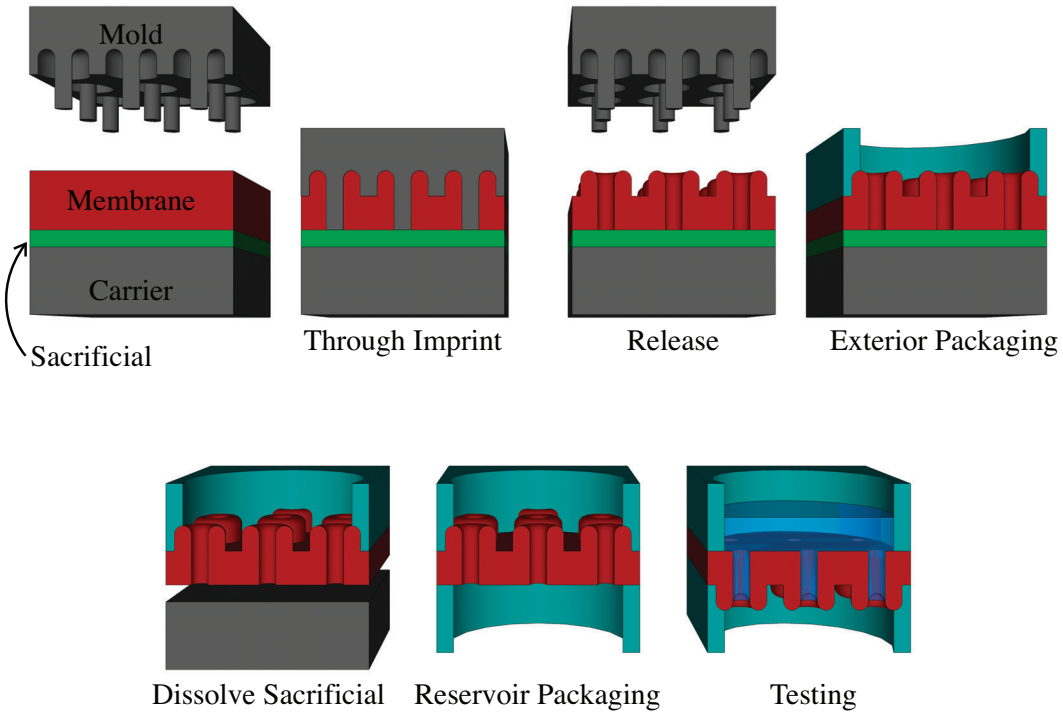


Figure 4.2: NIL fabrication, packaging, and testing of membrane pores.

In this work, self supporting SU-8 membranes were also fabricated using a modified imprint process. To begin with, the membrane SU-8 layer was coated on to a rigid silicon substrate. A sacrificial layer of high $M_w$ PMMA was coated between the SU-8 layer and the substrate to allow release at the end of the process. The PMMA layer also minimized the squeeze-flow of SU-8 beneath the mold protrusions, ensuring proper through-imprinting of the membrane layer. High molecular weight PMMA was chosen to facilitate the spin coating of the solvated SU-8.[39] The material stack was imprinted using thermal imprinting mode by heating and pressurizing with the mold. The imprint mold was designed to pattern the crucial exit side of the pore membrane. In Chapter III, it was shown that the re-entrant $-90°$ sidewall profile, on the exit side of the membrane, is responsible for differentiating liquid flow-through behavior.

After the mold was released from the imprinted SU-8, the exit side exterior packaging material was applied. Polymerizable PDMS was used as the exterior packaging to anchor the membrane and to provide easier manual handling. PDMS was chosen due to its solvent compatibility with the later fluids for testing.[77] After a UV light exposure to activate the embedded crosslinking agents in the SU-8, the carrier, along with sacrificial, SU-8, and PDMS packaging were heated to polymerize the SU-8 and PDMS. Following crosslinking, the sacrificial layer was removed in solvent and the SU-8 with PDMS were released from the carrier wafer. Each membrane was manually affixed to a reservoir structure, again using PDMS to form the leak-proof seal. Additional fabrication details will follow after the sections on design specification and mold fabrication.

## Appropriate Membrane and Pore Length Scales

Selection of length scales for the membrane and pores is based on several competing factors. These include: required flow-through pressure, membrane thickness, membrane diameter, membrane yield stress, pore diameter, and imprint aspect ratio. The polymer membranes were packaged for testing by mounting to circular ring supports at the peripheries. Deformation due to application of pressure on such supported membranes is known as plate bending, and causes radial and tangential stresses as shown in Equation 4.1, where $\sigma$ are stresses at plate radius $r$, $P$ is the applied pressure, $\nu$ is Poisson's radio, $a$ is plate radius, and $h$ is plate thickness.[78]

$$\sigma_r = \frac{3P}{8h^2}\left(a^2(1+\nu) - r^2(3+\nu)\right)$$

$$\sigma_t = \frac{3P}{3h^2}\left(a^2(1+\nu) - r^2(1+3\nu)\right) \qquad 4.1$$

Maximum stress occurs at the plate edge by the anchor, as in Equation 4.2, where variables have been rewritten such that $r$ is membrane radius and $t$ is membrane thickness.

$$\sigma_{max} = \frac{3Pr^2}{4t^2} \tag{4.2}$$

This plate stress should be kept below the yield stress of SU-8, which is reported to be approximately 115 MPa.[79] Imprinting aspect ratio is the depth to diameter of the membrane pores in this case. A conservative aspect ratio of $t$ / $d_{pore}$ = 3 was chosen to maximize processing yield. The maximum expected liquid pressure is estimated based on the maximum of equilibrium meniscus pressure, as discussed in Chapter III. This is approximately $2\sigma_{la}$ / $r$. Balancing all these factors together results in the inequality shown in Equation 4.3

$$\begin{cases} \dfrac{t}{d_{membrane}} = \sqrt{\dfrac{3P_{max}}{16\sigma_{yield}}} \\ P_{max} \approx \dfrac{2\sigma_{la}}{r} \\ \dfrac{t}{2r} \leq 3 \end{cases}$$

$$\Rightarrow t \geq \left( d_{membrane}^2 \frac{\sigma_{la}}{16\sigma_{yield}} \right)^{1/3} \tag{4.3}$$

When membrane diameter $d_{membrane}$ = 10 mm and water surface energy is used ($\sigma_{la}$ = 72.8 mN/m), the design rule gives a membrane thickness of $t$ = 40 μm. At this membrane thickness, pores should be sized to at least 13 μm, and the measurement equipment able to measure liquid pressures on the order of 22 kPa and less. At these pressures, a sensitive manometer able to measure up to 224 $cmH_2O$ will be required.

Based on these design estimates, membrane and pore design geometries were chosen to be: $t = 40$ μm and $d_{pore} = 10$ μm. The general shape requirement of the membrane imprint mold can be seen in Figure 4.3. The imprint mold should comprise of 40 μm tall pillar-like protrusions, each surrounded by a trench structure that extends further into the mold bulk. The radius of the pillars and trench curvature should be 5 μm. The imprint mold should be composed of a rigid material such as silicon or glass.

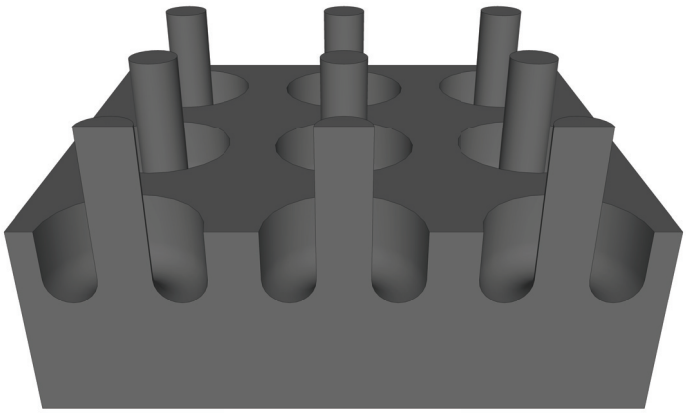

Figure 4.3: Imprint mold design requiring two-level lithography.

These length scales push the upper limits of common microfabrication processes, particularly due to the pillar height. The mold can be fabricated from silicon or glass by masked etching of the surface to a depth equal to the pillar height. Options for such etch processing would be limited to deep reactive ion etching (DRIE) or isotropic wet etching. Other etching processes would be impractically slow to utilize in this process. In this work, wet etching was chosen due to its rapid etch rates and isotropic etch profile. The imprint mold appearance is markedly different from Figure 4.3 due to this isotropic etch profile, but the same general features exist. It is shown in Figure 4.4. An isotropic wet etch can be used to pattern first the pillars. Then, after a second lithography step, a second isotropic wet etch for the trenches surrounding the pillars. Square geometry is also designed because such layouts require less resources to generate on the available photomask making equipment.

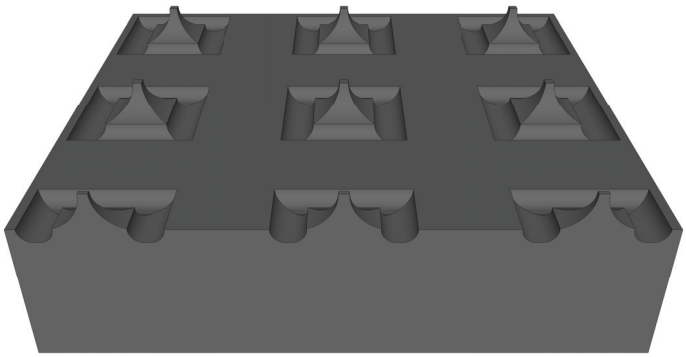

Figure 4.4: Isotropic etch processed membrane mold.

**Pore Membrane Imprint Mold Fabrication**

Mold fabrication began with two photomask designs. The first level mask layout was comprised of a regular array of dark squares on a bright field. Square density and size were laid out spanning one order of magnitude, from 10 to 100 μm, to anticipate any future changes in fabrication processes (for example, DRIE can utilize smaller, higher density square patterns). The second level mask layout was comprised of a regular array of bright square outlines on a dark field. Both photomask layouts align to each other so that the pillar and trench structures are properly centered. Each continuous field of array patterns was $(8\ \text{mm})^2$. Borders were included and sets of four dies were lumped into larger, $(20\ \text{mm})^2$ macro dies. These were laid out at 1:1 size in a $4 \times 4$ array to fit on 100 mm diameter wafers with the four corner dies removed, resulting in 12 macro dies per wafer.

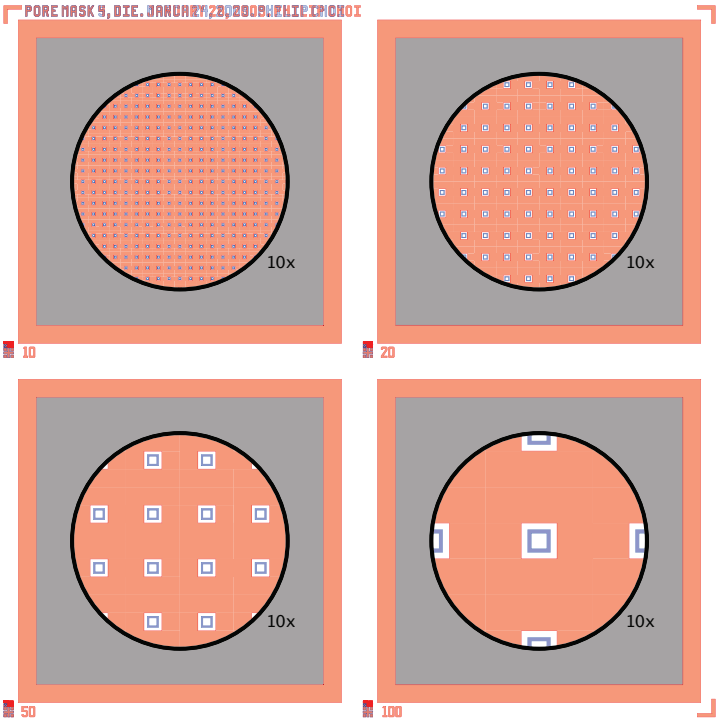


Figure 4.5: Individual membrane macro die layout pattern. Features are enlarged within the circles to show detail.

Borosilicate glass (BSG) wafers with a hydrofluoric acid isotropic etch process were chosen as the substrate and patterning scheme. Polished and cleaned wafers were first stripped of the top layer of glass in HF. Gold was then deposited by evaporation onto the wafers, with a chrome adhesion layer in between. Image-reversal photoresist was spin coated, followed by photolithography using the first level mask pattern. Photoresist was developed and flood exposed to activate the crosslinking agents. Wafers then underwent a post-exposure bake to crosslink and densify the photoresist. Afterwards, the Cr/Au metal layers were acid etched using the photoresist mask to expose the underlying BSG substrate. Wafers were again hard-baked to ensure good adhesion between the photoresist and metal layer.

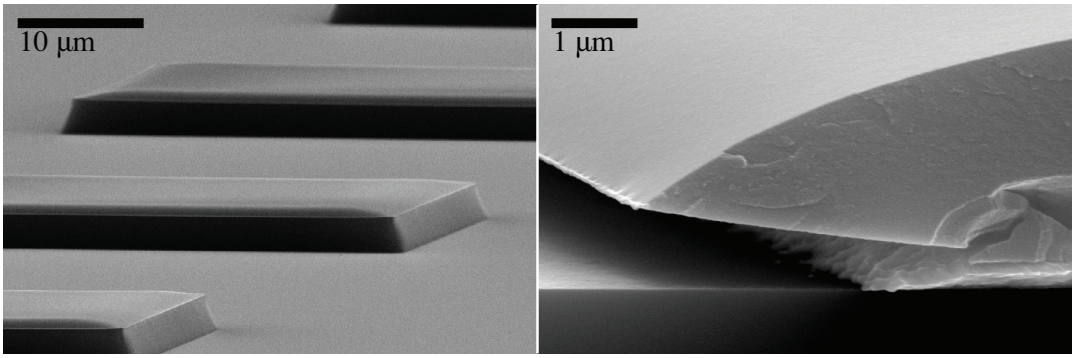


Figure 4.6: Photoresist on Cr/Au metal layers, on BSG wafer. Right: detail of Cr/Au undercut below photoresist edge.

Wafers were then etched in an HF acid mixture to etch the primary pore pillars to a depth of approximately 38 μm, leaving a narrow portion of original BSG surface of approximately 11 μm at the tops of the pillars. After etching, the wafers were stripped of photoresist, gold, and finally chrome. Pillar structures that were fabricated are shown in Figure 4.7. This completes the fabrication for molds that imprint 0° sidewall membrane pores. Prior to using these molds for imprinting, they were given a final clean followed by vapor coating with fluorosilane mold release agent.

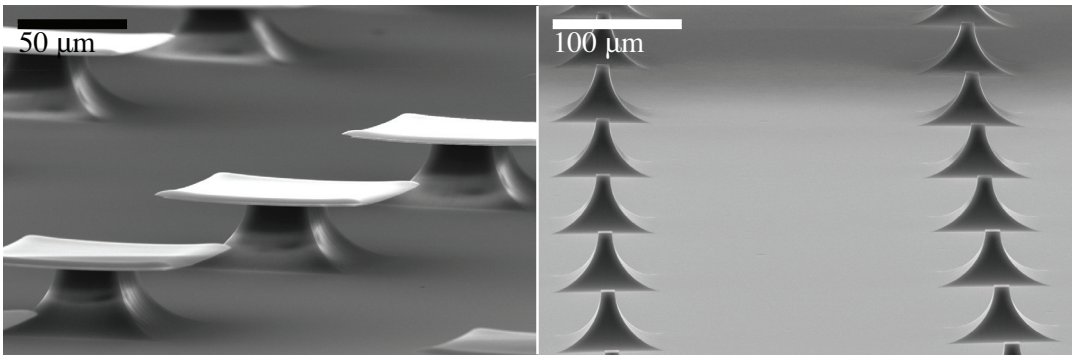


Figure 4.7: Isotropic HF etching of BSG, with Cr/Au/PR etch masks still attached. Right: completed etched pillar structures 11 μm × 38 μm.

Wet etching of the wafers in HF was not a trivial task. It was found that the material quality of the glass as well as the quality of the metal etch mask greatly affected the uniformity and sidewall angle of the etching. Initial etching results showed a large amount of lateral undercut and a very shallow sidewall angle, as shown in Figure 4.8.

Further etching attempts with poor quality glass substrates resulted in a heavily pitted surface, presumably due to inhomogeneous glass structure and uneven etch rates. Lift-off processing can exacerbate the low sidewall angle problem due to inadequate Cr to glass adhesion. Instead, depositing the Cr/Au layer on cleaned glass that was also pre-etched improved the adhesion quality. Leaving the photoresist and Cr/Au patterning layer on during the HF wet etch also served to improve masking effects. Pitting in the substrate is evidence of poor quality substrate material. Addition of hydrochloric acid to the HF solution to dissolve trace impurity oxides did improve results, as well as pre-etching the glass to avoid surface defects from foundry polishing. [80-81] Successful patterning was obtained only after these key steps were taken.

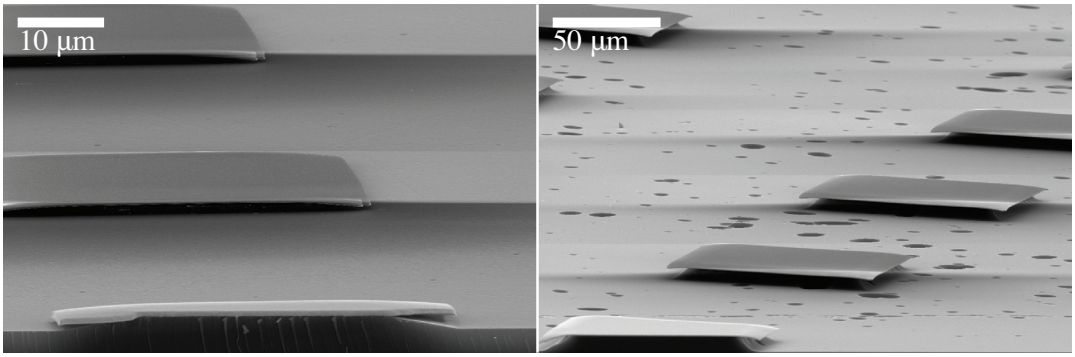


Figure 4.8: Poor quality etch results on glass due to left: inadequate mask protection, and right: poor quality substrates.

To pattern the –90° sidewall features, select molds continued on to second level lithography and patterning. The cleaned wafers were coated again the Cr/Au, followed by a thick layer of photoresist, sufficient to cover the entire height of the protruding pillars of the molds. These and other issues resulting from such thick photoresist are covered in the next section. Wafers were exposed with the second layer pattern and developed. Again, the Cr/Au layers were acid etched using the photoresist as a mask, followed by etching in an HF mixture to a depth of approximately 10 µm. Afterwards, the photoresist and Cr/Au layers were stripped, and the molds vapor coated with fluorosilane mold release agent prior to imprinting. Full details of the mold fabrication

process are available in Appendix E. Figure 4.9 shows the pillar profile of 0° and −90° sidewall molds.

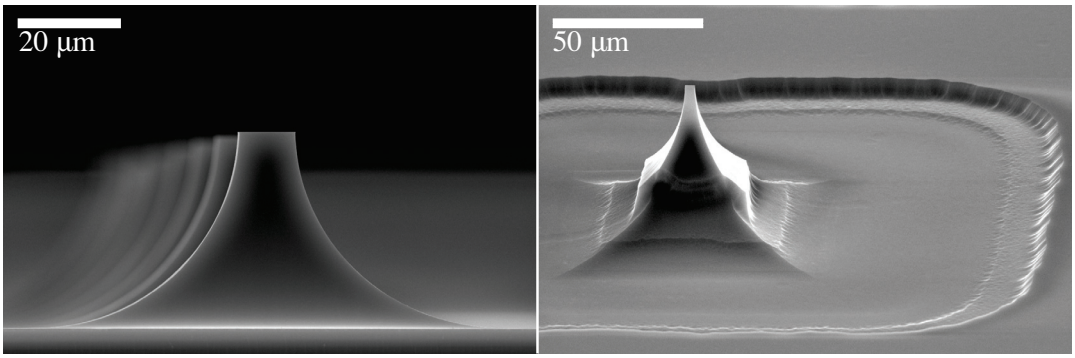


Figure 4.9: 0° (left) and −90° (right) angle sidewall imprint mold structures.

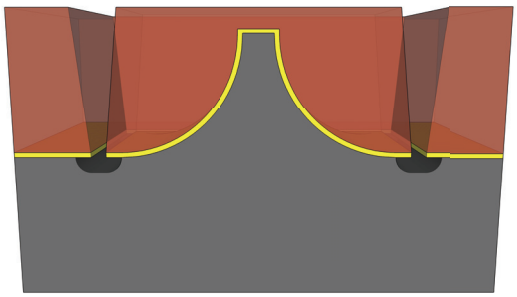

Figure 4.10: Thick photoresist is utilized to pattern trenches while protecting the tall pillars.

### Thick Photoresist Processing

To protect the existing pillar structures from the first level patterning during the second level trench etching, a very thick layer of positive photoresist was used, and its processing was not a trivial task. The positive photoresist used was AZ 9260 (AZ Electronic Materials).[82] The pillars to be protected were approximately 40 µm tall, so

a photoresist coating of approximately 40 μm was used. It was found that the resist wetted the pillar wall and tip sufficiently at this thickness. Because this layer was so thick, an extended soft-bake time of several minutes was required to sufficiently remove the resist solvent. Failure to do so would cause burning and cracking formations upon exposure due to residual solvent, as well as fouling of the photomask used in the contact aligner.

Subjecting the resist to such a long soft-bake time would cause it to become overly dehydrated. The destabilized diazonaphthoquinone requires a water molecule to convert to an acid, and with insufficient moisture in the resist, this photoacid generation fails. To remedy this, the wafer was placed in a warm water bath for several minutes following the prior lengthy soft-bake step. A warm water bath was used because the thermal shock of using room temperature water would commonly cause the resist to fracture.

Exposing such thick resist required a great deal of photon energy, and it was found empirically that approximately 7 J/cm$^2$ exposure dose was required. Compare this to the typical exposure dose required for typical resist thicknesses: 150 mJ/cm$^2$. The high exposure dose was also partially due to the fact that glass substrates were used. The thin Cr/Au layer on the glass did not reflect as much light as a silicon wafer would have, thus requiring such a high exposure dose.

Developing such thick resist also required an unusually long dissolution time. It was found that AZ 400K, diluted 3:1 with water, was the only developer solution with adequate sensitivity, over 4:1 AZ 400K or other organic developers. Even still, the AZ 9260 required a full 10 min developing time to fully clear out the narrow trench features surrounding every pillar. This long develop time is somewhat exacerbated by the large thickness to width aspect ratio of the features.

After etching the Cr/Au metal mask, the AZ 9260 resist was removed. Because of the narrow opening through which the HF solution had to reach the BSG substrate, the resist was stripped prior the wet etching to keep from loading the reaction. Manual or ultrasonic agitation of the gold and chrome etch solutions is also advisable due to this potential wetting issue. Process details are available in Appendix E.

## Membrane Imprinting

Clean substrates of polished silicon wafers were first coated with a 20 μm thick PMMA layer. The polymer has high molecular weight: $M_n$=950 kg·mol$^{-1}$, so that it would not dissolve or overly intermix with the following SU-8 layer during spin coating. The PMMA layer was thoroughly baked at high temperature to ensure as much solvent was removed as possible, to prevent any outgassing during imprinting. Afterwards, SU-8 was coated onto the PMMA at a thickness of approximately 34 μm. This thickness was chosen to not exceed the pillar height of the mold, such that the pillars would squeeze and imprint through the SU-8 layer into the sacrificial PMMA layer. This is the zero residue process shown in Figure 2.5. The sample was again baked for an extended period of time to prevent outgassing of solvent from the relatively thick films during imprint.

Imprinting was carried out using an NX-2000 (Nanonex). Samples were vacuum sealed followed by an imprint at 95 °C, 200 psi, for 2 min, and cooled to 40 °C before releasing pressure. Molds were then removed from the SU-8, and the entire carrier wafer was flood exposed to a UV dose of approximately 180 mJ/cm$^2$ to activate the crosslinking agents in the SU-8 layer. Degassed PDMS was then applied in 6 mm rings centered on the exit sides of the pore membrane dies. These rings of PDMS were held in place by short cylinders of polyethylene tubing. The assembly: carrier wafer, sacrificial, imprinted SU-8, and molded PDMS, was heated to polymerize both the SU-8 and PDMS polymers.

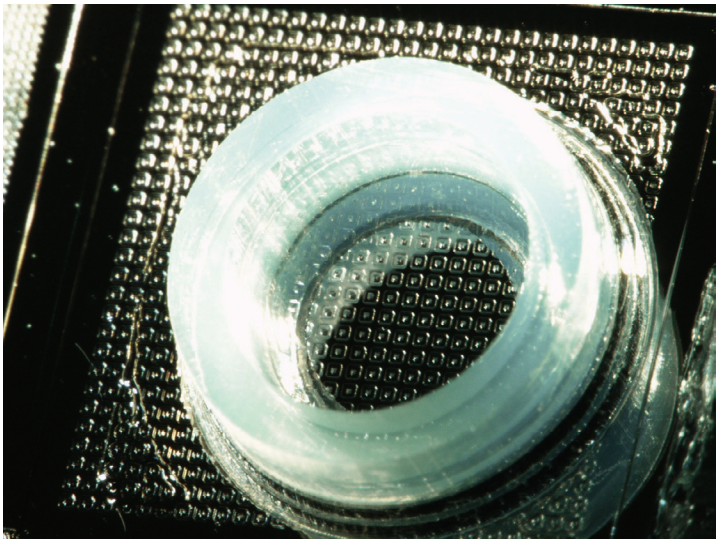

Figure 4.11: Imprinted, cured, but unreleased −90° sidewall SU-8 membrane with PE and PDMS rings attached to the exit side.

Carrier wafers were then soaked in solvent to dissolve the sacrificial PMMA layers, releasing the SU-8 membranes. During this time, the PE tubes used to mold the PDMS detached from the substrate. The membranes were then rinsed in fresh solvent and dried. Membranes were finally manually affixed to the ends of longer lengths of PE tubes, also 6 mm in diameter and again with PDMS. Samples were heat cured and finally ready for use. See Appendix F for full process details. Figures 4.12 and 4.13 show the fully packaged 0° and −90° sidewall pore membranes. Figure 4.14 shows SEM images of cut membranes.

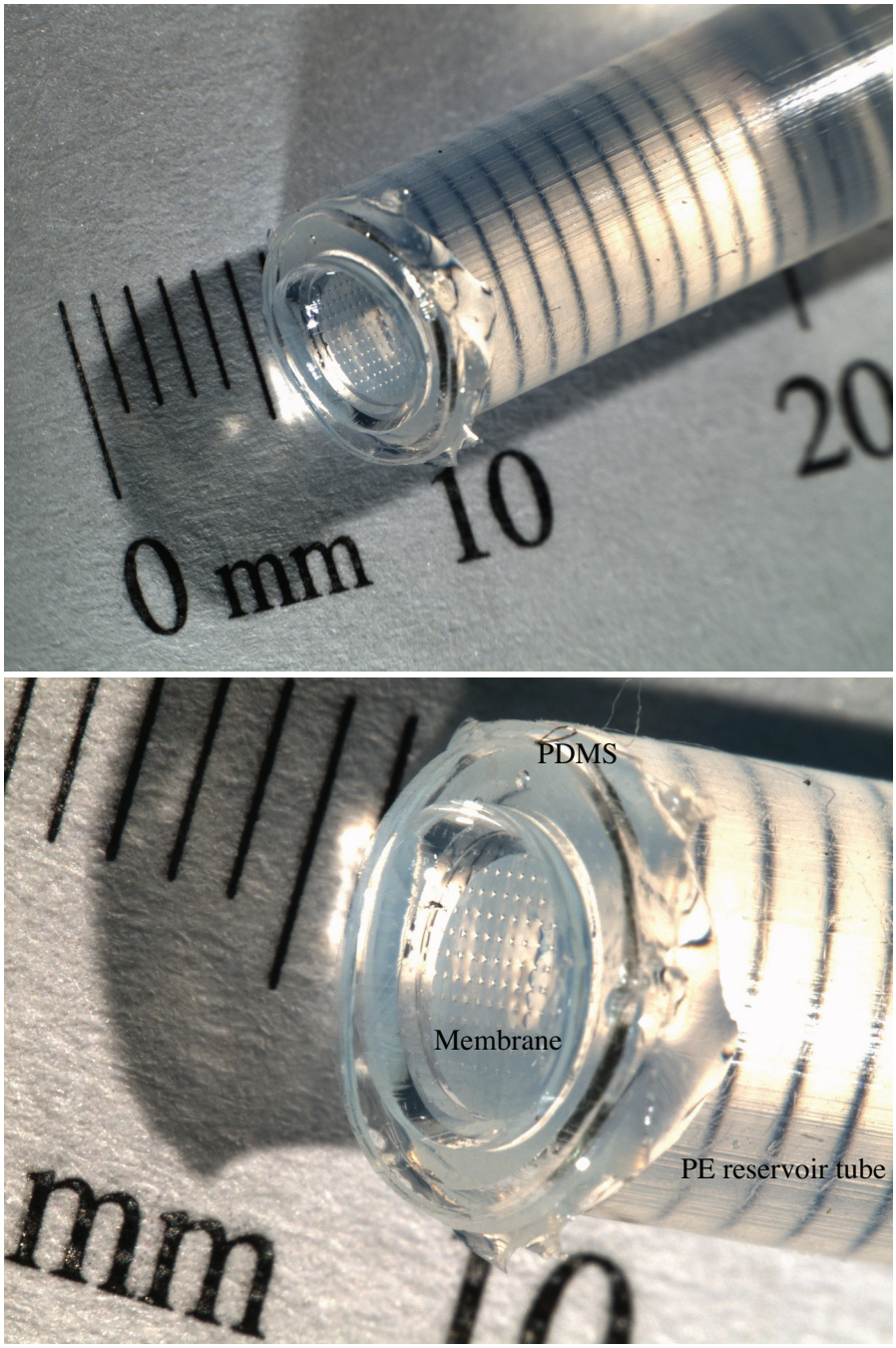

Figure 4.12: Fully packaged 0° sidewall pore membrane.

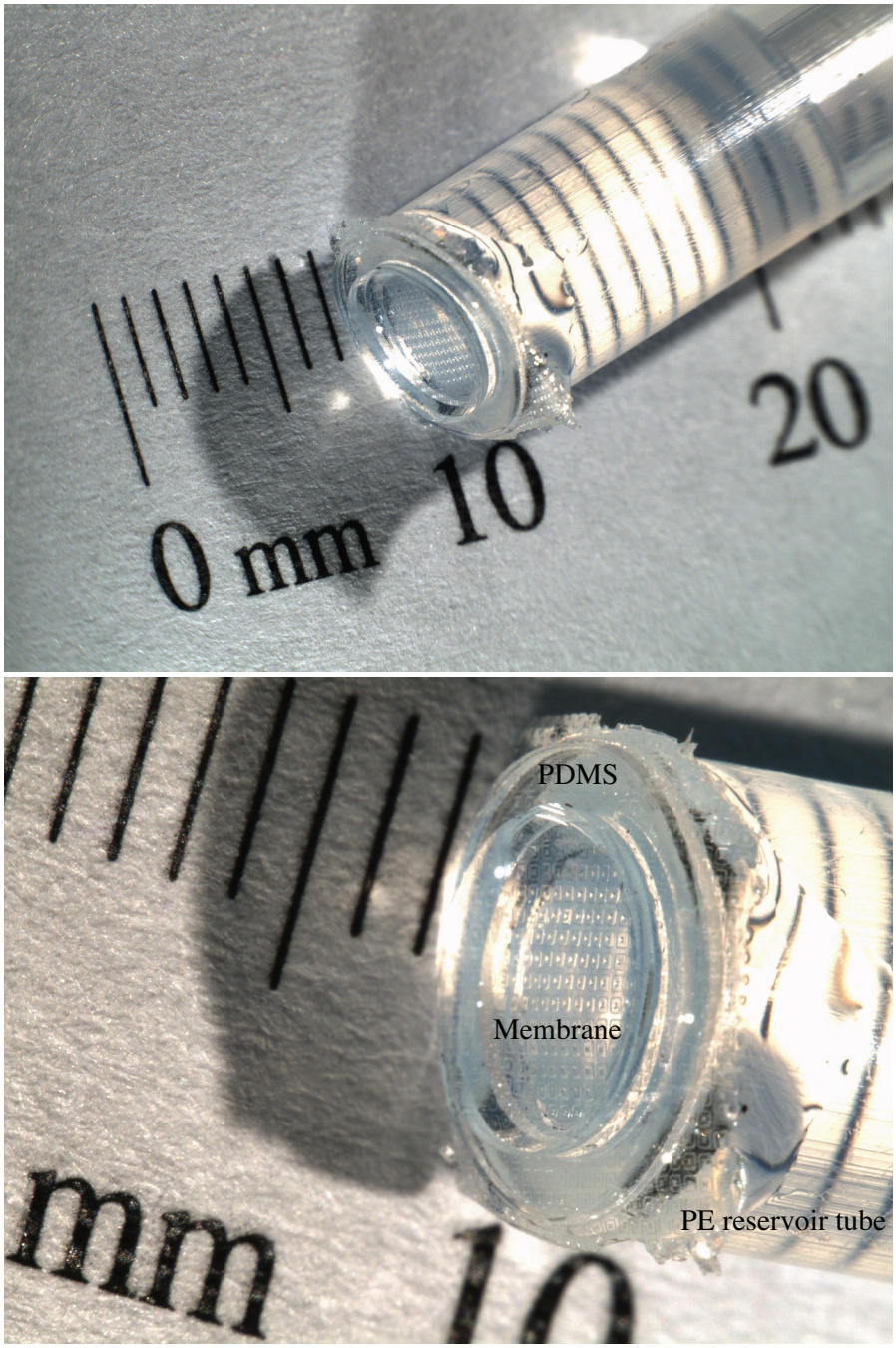

Figure 4.13: Fully packaged −90° sidewall pore membrane.

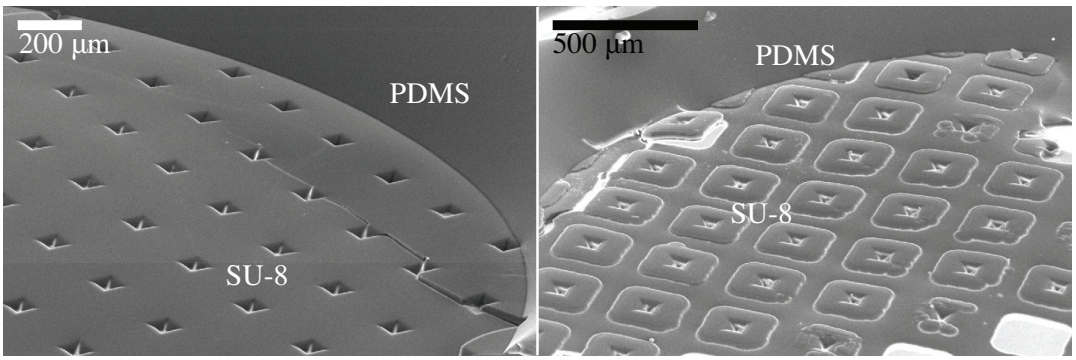

Figure 4.14: Dissected −90° and 0° sidewall pore membrane packages, showing pore morphology and anchor seal.

## Conclusions

Freestanding polymer membranes have been fabricated using a custom imprinting process. The membrane diameter, thickness, pore diameter, and pore contour were all chosen deliberately to test conclusions reached by models in Chapter III. Membranes were fabricated from SU-8, a cross-linking polymer that is formulated from a monomer composition that is a solid thermoplastic at room temperature. Whereas most NIL crosslinking resists are formulated to be low viscosity liquids at room temperature, SU-8 can be easily dissolved, spin coated, and dried at specific thicknesses on the substrate before imprinting, which gives a high level of control over the imprinted membrane thickness. The imprinting process essentially becomes thermal imprinting, heating the SU-8 up to an imprint temperature above its $T_g$ = 55 °C.[73] Because the mold can be removed prior to UV activation and polymerization bake, any uncured SU-8 residue on the imprint mold can be removed with solvent. Contrast this to liquid resists which must be polymerized with the mold *in situ*, potentially contaminating the mold with insoluble residues.

Imprinting into such thick SU-8 layers stretches the limits of microfabrication, and atypical spin coating procedures, including slow, short spin times and multiple layers, are utilized to produce polymer films of this thickness. This is non-ideal, and more

optimal solutions such as higher concentration resists, dip-coating, or laminating would be an improvement. But the process demonstrates the possibility of applying imprint processing to this size regime.

Prior to releasing from the sacrificial layer, the fully formed and polymerized SU-8 membranes were made more durable by the addition of a PDMS ring at the die edges. This relatively thick layer of PDMS greatly improved the handleability of the membranes, especially during the rinse and dry process after PMMA dissolution. PDMS was further used to package the fragile SU-8 membranes by sealing them to the bottom sides of long polymer tubes. These tubes are convenient to manipulate by hand for subsequent testing purposes. The wetting behavior of various $\sigma$ liquids will be tested on these packaged membranes in Chapter V.

# CHAPTER V

## Pore Membrane Pressure Testing and Comparison to Equilibrium Meniscus Pressure Calculation

Negative sidewall angle pore membranes were predicted in Chapter III to exhibit similar $P_{max}(n)$ for large $\theta$ valued solid-liquid interactions, but diverging behavior for small $\theta$ situations. Pore membranes with sidewalls of $-90°$ and $0°$ were successfully fabricated, as shown in Chapter IV, to test this hypothesis. A consequence of the membrane design was the need to measure test pressures on the order of 0.1 kPa. A custom built water manometer was used to perform these tests.

It will be shown in this chapter that the sidewall shapes of the imprinted pore membranes can be used to predict their wetting behaviors. The equilibrium meniscus pressure calculation method from Chapter III will be revisited and used to predict the outcomes of the wetting tests.

## Manometry

Liquid pressures in the membrane reservoirs were actuated and measured using a custom built manometer-pump device. The schematic is shown in Figure 5.1. The 1 m high measurement column is a U-tube filled with water. One end of the tube is open to atmosphere as reference, while the control end is connected to the syringe pump pressure actuator and the reservoir-membrane package. Liquid column height differentials give gauge pressure of the control chamber of the manometer, such that readings indicate the

pressure applied to the test liquid inside the membrane reservoir. All fittings on the control chamber are sealed so that leaking air will not adversely affect measurement accuracy. A microscope with camera is mounted in view of the membrane to observe liquid menisci on the exit side.

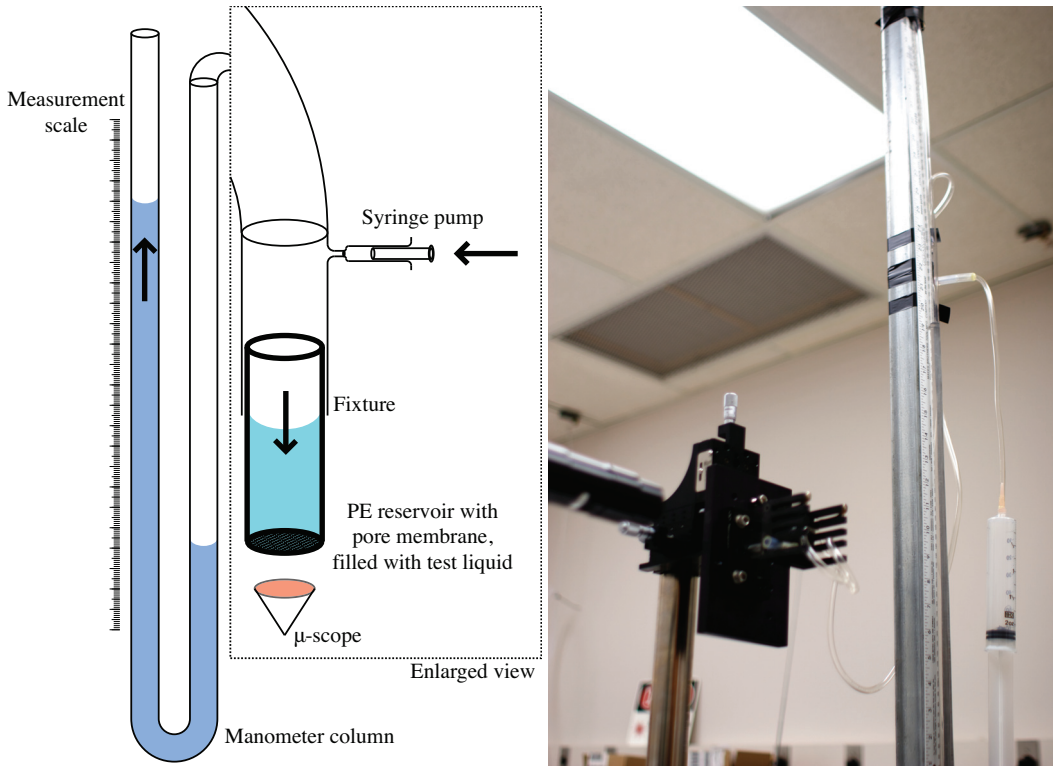


Figure 5.1: Schematic and photograph of manometer-pump testing device.

### Measurement of $\theta$ and Approximation of $\sigma$

For testing, two liquids were chosen: deionized water and CMOS grade methanol. The two liquids' $\sigma_{la}$ values are known at room temperature (20 °C) to be 72.94 mN/m and 22.50 mN/m, respectively.[11] Because the water and methanol are miscible, the two liquids can be mixed to create fluids of intermediate surface energies

and contact angles. The contact angles $\theta$ and surface energies $\sigma_{la}$ of the test solutions are required to predict equilibrium membrane pressures for the system.

Utilizing a mixture of these two fluids is useful in that many test mixtures within the $\theta$ and $\sigma_{la}$ ranges can be created simply by varying the concentrations. Because the membrane and packaging seal are polymers, it is also useful to limit test liquids to those that are known to not absorb too readily.[77] Unfortunately, the drawback is that the $\sigma_{la}$ values for water-methanol mixtures are not well known or agreed upon, due to the complex interaction of the molecules in solution. Matsumoto *et al*. provide a useful survey of these $\sigma_{la}$ values in their simulation work.[83] The variance in these values must be taken into account when comparing the $P(n)$ calculations to the measured pressures.

Contact angles $\theta$ for the test solutions were measured against control SU-8 surfaces: these flat, unpatterned SU-8 membrane surfaces were processed along-side the porous membranes up until PMMA dissolution. Table 5.1 summarizes these contact angle measurements. Details of the measurement setup are available in Appendix G. The $\sigma_{la}$ row of the table is estimated based on Matsumoto, Figure 5.2.

| **$H_2O$:$CH_3OH$ wt. fraction** | **1.00:0.00** | **0.75:0.25** | **0.50:0.50** | **0.25:0.75** | **0.00:1.00** |
|---|---|---|---|---|---|
| $\overline{\theta}$ | 85.05° | 68.69° | 56.73° | 43.88° | 24.27° |
| **$\sigma_{la}$ (mN/m)** | 72.94 | 40 | 30 | 25 | 22.50 |

Table 5.1: Contact angles of $H_2O$:$CH_3OH$ mixtures on smooth SU-8 surfaces.

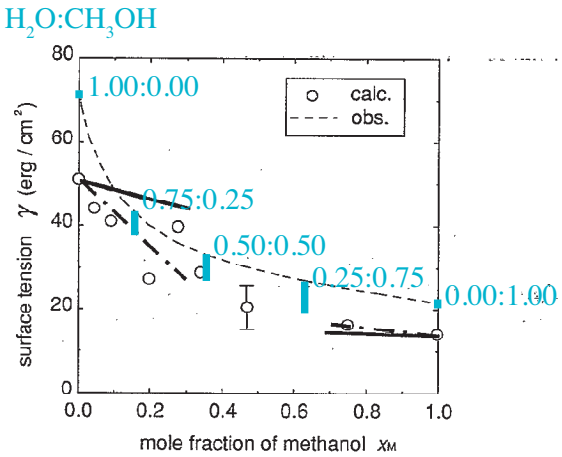


Figure 5.2: Estimated $\sigma_{la}$ values. Reproduced from [83]. Annotations in blue have been added.

**Predicted Equilibrium Meniscus Pressures**

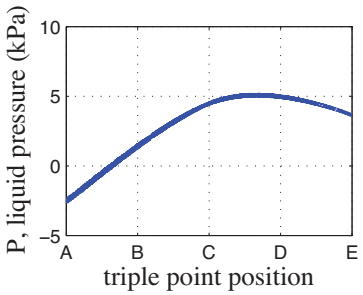


Figure 5.3: $P_{\max}$ significance.

During testing, forward pressure will force the test liquids into the membrane pores and through, depending on the magnitude of the pressure. Examining the simplified Figure 5.3, it is apparent that the maximum meniscus pressure is calculated to be approximately 5 kPa. $P = 0$ at a point between A and B. This means that when the sample is loaded and zero liquid pressure is applied, the liquid will readily wet up until this point. Forward control chamber pressure will cause the liquid to flow into the pore. During testing, it is imperative to use a slow enough pressure change to allow for the

limited flow rate of the liquid. In other words, the triple point location must be allowed to trail behind as close to equilibrium $n$ as possible.

Though the manometer equipment is not sophisticated enough to monitor the exact position of the triple point for all $P$, $P_{max}$ can be easily measured by slowly raising the control chamber pressure until menisci are seen readily flowing through on the exit side camera monitor. This is due to the fact that when the triple point moves beyond the $P_{max}$ point, the $dP / dn < 0$ unstable region is encountered, as discussed in Chapter III.

High resolution SEM images of the imprint molds, Figure 4.9, are traced as input data to the equilibrium calculation script. The revision of the script used in this chapter appears in Appendix H. In Figure 5.4, the 0° sidewall membrane pore profile has been traced, and equilibrium meniscus pressure plotted on the upper left, and breakthrough pressure on the right. Similarly, in Figure 5.5, the −90° sidewall profile has been traced and analyzed.

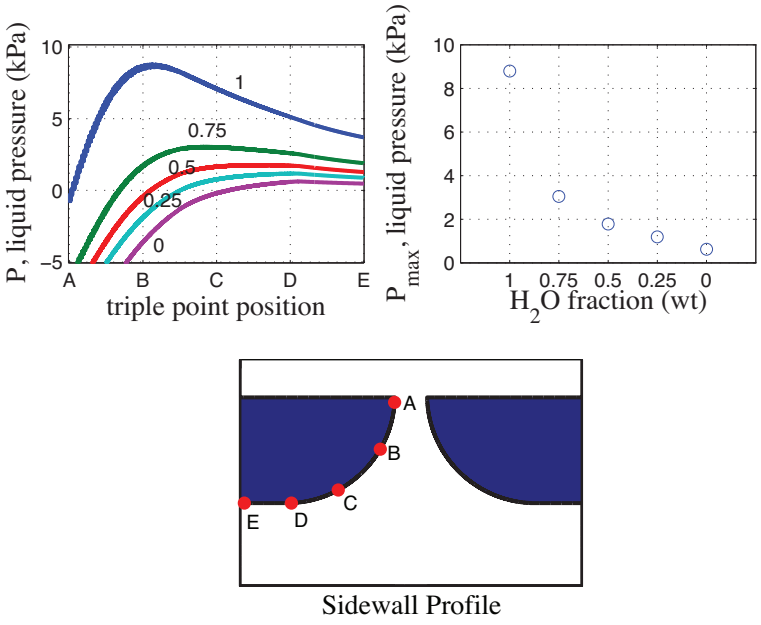


Figure 5.4: Traced 0° sidewall pore membrane and calculated equilibrium and breakthrough meniscus pressures.

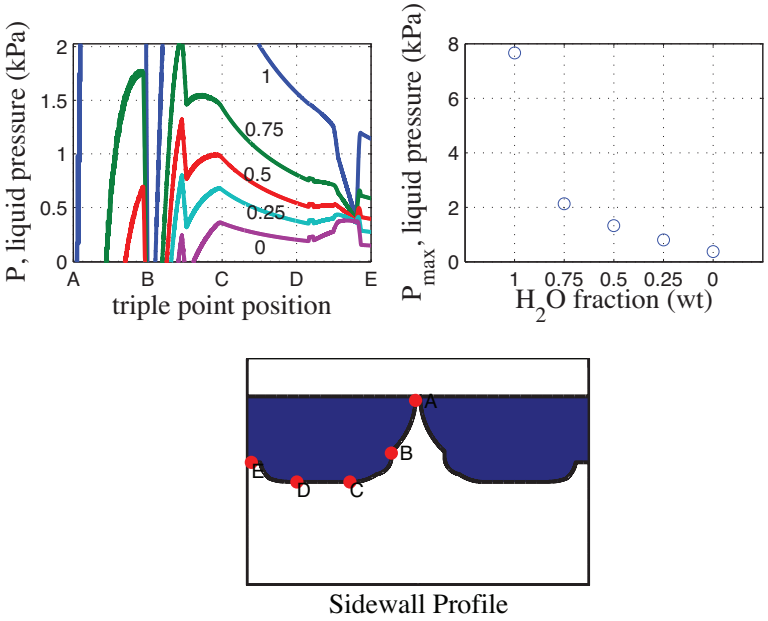


Figure 5.5: Traced −90° sidewall pore membrane and calculated equilibrium and breakthrough meniscus pressures.

## Breakthrough Pressure Measurements

When measuring the breakthrough or $P_{max}$ pressure of the fabricated pore membranes, each membrane was loaded with test liquid in the reservoir and clamped onto the control chamber fixture. The monitoring camera was positioned and focused to be able to observe the liquid action on the exit side of the membrane. Manual pressure was applied using the syringe. At first, the rate of pressure rise was rapid to establish the proper range for $P_{max}$ and to test whether the membranes were working properly without tears or leaks. Each time liquid penetrated through the pores, pressure at the control chamber was reversed to cease flow. The exit sides of the membranes were always blown dry with a gentle stream of dry $N_2$. With an expected pressure range established, the control pressure was raised to with 2 cm$H_2O$, and then a slow pressure rise at a rate of

0.2 cm$H_2O$/s was applied. As soon as menisci were observed penetrating the pore membranes, the pressure increase was ceased and the value logged.

Initial breakthrough fluid flow was not simultaneous across all pores, due to minute differences in fabrication shape and size. Droplets also tended to coalesce once a sufficient volume of fluid had flowed through. Some microscope monitor frames showing the breakthrough effluence of liquids is shown in Figure 5.6. Because of this factor, the pressure value was measured not at the first pore being broken through, but after at least two were leaking liquid.

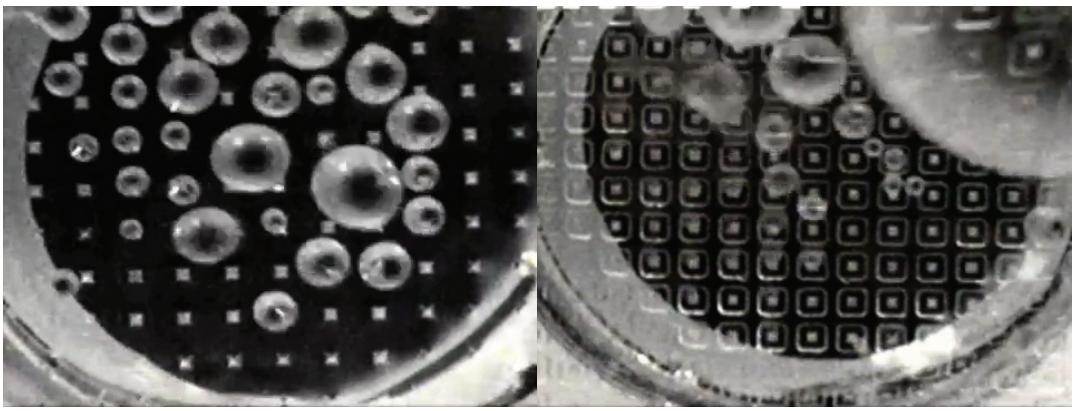

Figure 5.6: Observation of large droplet menisci exiting the membrane pores.

Between liquid types, the membrane reservoirs were rinsed twice and the pores purged during the beginning of the subsequent baseline establishing phase. Series of five breakthrough pressure measurements were taken for each of the five mixtures of water and methanol, each of two types of membranes. The standard deviation of each set of measurements was found to be fractions of 1 kPa, so the measurements are taken to be fairly experimentally consistent. The measurements were averaged and converted into the proper units and are plotted on Figure 5.7. For both pore structures, there is good agreement between the calculated and measured data for breakthrough pressures particularly for the methanol phases.

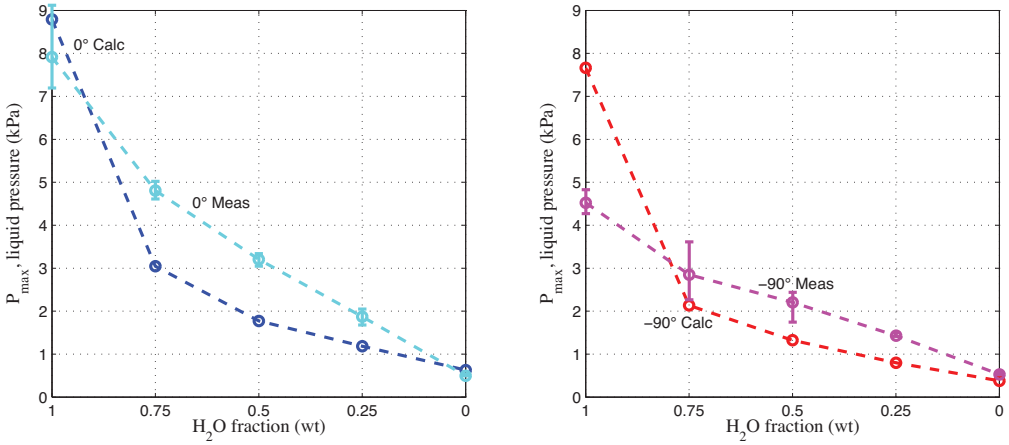


Figure 5.7: Comparison between expected breakthrough pressures and measured breakthrough pressures. Error bars on measured data indicate highest and lowest samples out of $n = 5$.

There is less agreement between measured and calculated breakthrough pressures for other liquid mixtures. The trend for both membranes is uniformly higher pressures for the three heterogeneous $H_2O$ and $CH_3OH$ mixtures, and lower measured pressure for pure water tests. One possible explanation for the higher measurements for the heterogeneous mixtures is that breakthrough pressure will always be measured high, though this does not explain the discrepancy for pure water tests. The reason for erroneously high $P_{max}$ measurements is likely due to the limited flow rate of fluid through the pores, coupled with the limited image resolution of the monitoring system. Because the control chamber pressure is continuously raised, even with the slow, 0.2 $cmH_2O/s$ rate, $P_{max}$ will be exceeded before a visible meniscus is seen through the microscope. Nevertheless, the general trend of measured data does follow the calculated breakthrough pressures well. These data help to validate the breakthrough, equilibrium pressure, and free energy calculation methods shown in Chapter III. The model is versatile in the parameterized data that it accepts, making it flexible for both designing and evaluating liquid micropore geometries.

## Conclusions

Liquid breakthrough pressures were measured on the two types of pore membranes previously fabricated. The cross-sectional profiles of the pores were traced and digitized by sidewall parameterization methods developed previously, and the equilibrium meniscus pressures $P(n)$ and breakthrough pressures $P_{\max}$ were calculated. Essential data for these calculations are the liquid surface energy $\sigma_{la}$ and the contact angle formed on the SU-8 surfaces. Contact angles were carefully measured using goniometry, but the three intermediate surface energies were interpolated based on conflicting reports in the literature.

To measure the small pressures required, a custom manometer was built. Measured breakthrough pressures were generally in good agreement with the expected values as calculated. Deviance is likely due to the intrinsic limitation of the measurement method, that is unable to pinpoint the exact $P_{\max}$ pressure.

# CHAPTER VI

## Conclusions and Outlook

Contributions made by this dissertation research are now summarized. A new class of imprint resist that incorporates inorganic siloxane polymer blocks or grafts was tested, characterized, and adapted for use in nanoimprint lithography (NIL). In comparison to primitive, homopolymer imprint resists, these resists were shown to have several advantages, including low mold adhesion or fouling, and strong chemical etch resistance. These copolymer resists were shown to pattern features down to 60 nm or less, and were utilized in multilayer resist coating and lithography to generate re-entrant sidewalls, pattern over existing topography, and imprint with no residual layer.

NIL often deals with fluids moving into small spaces, and the topic of wetting dynamics is a relevant and important one to this technology. Much recent work in stable dewetting phenomena has focused on modeling the interfacial physics involved. Along this vein, a new approach to imaging the profiles of grating and cylindroid sidewalls and using the contour data to predict wetting behavior was developed. Among the metrics explored were free energy, menisci pressure, and breakthrough pressure. The value and location of breakthrough pressures can be unexpected, especially if the sidewall contour changes are of the same or similar size to the cavity diameter.

NIL was utilized to form freestanding polymer pore membranes. These SU-8 membranes were designed to test the aforementioned wetting models, and along the way, the challenging and unusual pore geometries led to the development of new imprint processing and membrane packaging techniques. Testing liquid wetting behavior on these model membranes provided good evidence for the validity of the wetting models and opens the way for other uses of this methodology. Because the recent literature focuses heavily on the modeling of wetting behavior on micro-patterned surfaces, the

work here focused on a different paradigm of liquid penetrating into pores of a surface, through, and finally out the other side. It was found in this case that interesting divergence in wetting trends would occur based on the angle formed by the pore sidewall at the exit side of the membranes. Negative sidewall angle or "wraparound" exit pore structures would prevent the free flow of low energy fluids through the pore unless larger pressures were applied. Because of the negative sidewall angle, this type of structure is different than what can be achieved by a simple tube or fiber weave—the types of structures to which membrane breakthrough pressure analysis has been applied to up to now. Membrane pores have now been modeled in an exacting manner with regard to the effect of sidewall morphology on breakthrough pressure. Whereas surface wetting of microstructures has been modeled in this manner for quite some time, this is the first time such a model has been applied and verified on membranes.

Imprinted porous polymer membranes could find large uses as free-standing filtration, dispensing, or sampling tools. These durable membranes were fabricated from a brittle plastic, yet packaging them using an elastomer greatly improved their handleability around an external testing platform. Other materials choices for membranes could improve the durability and overall yield of such a process. The membranes were originally developed to test the wetting models mentioned previously, but they end up extending the breadth of NIL research as well, by virtue of the novel fabrication method used. This new imprinting technique extends the boundaries of NIL and of planar microfabrication as a whole. Indeed, some of the largest challenges in designing the membrane fabrication process were due to the extraordinary depths and thicknesses of etches and photoresist masks required. Fringing on three-dimensional fabrication should not be a deterrence, however, and the simple replication of numerous pore membranes towards the end was a testament to the speed and accuracy of the process in creating such finely yet deeply defined structures.

And while originally developed to address the issue of low viscosity imprint resists poorly wetting nano-structured imprint molds, there are a great deal of possibilities for the wetting calculation methods presented here. One particularly widespread area of application could be in the design of inkjet nozzles. Utilizing a negative-sidewall angle exit pore morphology could allow for modulation of dispensing pressures and droplet

sizes. Fouling of the nozzle structure is a particular challenge; combined with bulk material or coating choices to modify the $\sigma$ of the nozzle surfaces, low-energy dispensed fluids could be better controlled to prevent wetting between pores on the exit side. In the future, inkjets may be utilized to print a wider variety of materials such as organic-electronic molecules, colloidal metal suspensions, biological solutions, or lithography polymers in applications varying from optics, electronics, and microfabrication to microbiological research and medical diagnostics. It is conceivable that fluid residue or fouling of the exit side of nozzle arrays would be severely detrimental to the success of these future applications.

Controlled dispensing of low energy liquids, negative angle sidewall structures, and surface wetting dynamics are all areas that could use a fresh perspective in modeling and prediction. In this dissertation, the wetting model was applied to just two pore sidewall profiles and wetting modes, so there is much more work that can be done using this technique.

# APPENDIX A

## Synthesis and Characterization of Siloxane Copolymers

Synthesis processes and characterization data for the siloxane copolymers in Chapter II are presented here. This information is provided by Fu, and reprinted from Choi *et al*.[39]

## Synthesis Materials and Methods

Toluene and tetrahydrofuran (THF) were distilled freshly from sodium (3-8 mm sphere)/benzophenone prior to use. Styrene was refluxed over calcium hydride ($CaH_2$) for 4 hr and distilled freshly under vacuum prior to use. Anhydrous dimethylformamide (DMF), cyclohexane, n-butyl lithium ($^{n}$BuLi), methacryloxypropyl dimethylchlorosilane were purchased from Aldrich and used directly. All manipulation of air sensitive materials was performed with the rigorous exclusion of oxygen and moisture in dried Schlenk-type glassware. High purity argon (Michigan Gas) was used without further purification.

## Physical and Analytical Measurements

Nuclear magnetic resonance (NMR) spectra were recorded on a Varian XL-400 spectrometer. Chemical shifts for $^{1}$H, $^{13}$C, and $^{29}$Si spectra were referenced to internal solvent resonance and are reported relative to tetramethylsilane. Gel permeation

chromatography (GPC) was performed at room temperatures on a Waters 150 CV plus chromatograph equipped with a refractive index detector. Molecular weight averages were determined relative to a calibration curve (third order) created using polystyrene standards covering the molecular weight range of 580-2,300,000 g·mol$^{-1}$. Glass transitions were measured by differential scanning calorimetry (DSC), carried out on a DuPont 910 DSC.

**Synthesis of PDMS-Polystyrene Diblock Copolymer**

To a three-necked 2 L flask, equipped with a magnetic stir bar and a condenser, under nitrogen were charged anhydrous cyclohexane (275 mL) and styrene (freshly distilled from $CaH_2$, 80 g, 0.77 mol). The polymerization was initiated by the introduction of $^{n}$BuLi solution (3.2 mL, 1.6 M in hexane), and the solution turned to orange-red immediately. The mixture was stirred at RT for 2.5 hr to yield a viscous solution. Next, 100 mL of hexamethylcyclotrisiloxane ($D_3$) (120 g, 0.54 mol) in anhydrous cyclohexane (350 mL), dried over $CaH_2$ by refluxing for 2 hr, was introduced to the reaction flask. The mixture was then stirred at 60 °C for 1 hr; at the time a complete disappearance of the orange-red color was observed. The remaining $D_3$ cyclohexane solution was added into the reaction flask together with 120 mL of THF. The mixture was refluxed for 6 hr to yield an almost clear solution from the originally cloudy one and then cooled down to room temperature. The reaction was terminated with acetic acid (2 mL). The polymer was precipitated by the addition of methanol, collected by filtration, washed with methanol, and dried in a vacuum-oven (60-70 °C). Yield: 160.2 g (80.1%). GPC: $M_n$=45 kg mol$^{-1}$, $M_w/M_n$ = 1.19. $T_g$=−127, 100 °C. Weight fraction of each component was approximately 50%.

**Synthesis of Silanol Capped Polysiloxane Macromonomer**

To a 1 L Schlenk flask equipped with a magnetic stir bar under nitrogen were added $D_3$ (300 g, 1.35 mol), freshly distilled toluene (600 mL), and $^{n}$BuLi (37.8 ml of 1.6 M in hexane, 60.5 mmol) at room temperature (23 °C). The mixture was stirred for 15 min and followed by the addition of DMF (32 mL, ca. 10% weight of $D_3$) to accelerate the reaction. The reaction was monitored by gas chromatography, and stopped at 90% of $D_3$ conversion (3.5 hr reaction) by the addition of acetic acid (3.685 g, 3.5 mL, 61.4 mmol). The solution was continually stirred for a few hours and then filtrated through a 0.5 μm filter film using a pressure filter (60 psi). After the removal of the volatiles using a rotary pump, the yellowish viscous liquid was washed with acetone/ methanol (50/50 volume ratio) to yield a colorless liquid. Yield: 268 g (89.3%). $^{29}$Si NMR (in $CDCl_3$): 7.57 (Bu−$SiMe_2$−), −10.62 (HO−$SiMe_2$−), −21.96 (−$SiMe_2$−); GPC (relative to polystyrene, in toluene): $M_n$=5,119 g·mol$^{-1}$, $M_w/M_n$=1.05.

**Synthesis of Methacryloxyl Capped PDMS Macromonomer**

To a flamed Schlenk flask under nitrogen were added silanol terminated PDMS macromonomer, $BuSiMe_2$−$(OSiMe_2)_n$−OH ($M_n$=5,119, $M_w/M_n$=1.05; 100 g, 19.53 mmol), and triethyl amine (2.56 g, 3.53 mL, 25.4 mmol). The flask was stirred for two minutes and followed by the addition of methacryloxypropyl dimethylchlorosilane (5.61 g, 25.4 mmol) using a syringe. The mixture became cloudy immediately and was stirred for two hours at RT. The filtration of the mixture through a 0.45 μm pressure filter gave a clear liquid, which yielded a colorless liquid of the title polymer upon the removal of the volatiles under vacuum at 100 °C. Yield: 80 g (80%). $^{29}$Si NMR (in $CDCl_3$): 7.55 (Bu−$SiMe_2$−), 7.35 (−MA−$(CH_2)_3$−$SiMe_2$−), −21.96 (−$SiMe_2$−); GPC (relative to PS): $M_n$=5,086 g·mol$^{-1}$, $M_w/M_n$=1.07.[65]

**Synthesis of poly(dimethyl siloxane)-graft-poly(methyl methacrylate) (PDMS–g –PMMA)**

To a 500 mL three-necked flask containing a magnetic stirrer bar were charged methyl methacrylate (90 g, 0.90 mol), methacryloxyl capped PDMS macromonomer (10 g, 1.97 mmol), toluene (300 mL), and azobis(isobutyronitri1e) (AIBN, 0.1 g) under nitrogen. The mixture was stirred at 65 °C for 18 hr. The copolymers were precipitated in methanol, washed with hexanes to remove any unreacted PDMS macromonomer, and dried under reduced pressure. Yield: 85 g (85%). $T_g$=105 °C. PDMS content was approximately 10% by weight.

**Synthesis of poly(dimethyl siloxane)-graft-poly(methacrylate)-co-poly(isobornyl acrylate) (PDMS–g–PMIA)**

To a 500 mL three-necked flask containing a magnetic stirrer bar were charged isobornyl acrylate (80 g, 0.38 mol), methyl acrylate (10 g, 0.12 mol), methacryloxyl capped PDMS macromonomer (10 g, 1.97 mmol), toluene (300 mL), and azobis(isobutyronitri1e) (AIBN, 0.1 g) under nitrogen. The mixture was stirred at 65 °C for 18 hr. The copolymers were precipitated in methanol, washed with hexanes to remove any unreacted PDMS macromonomer, and dried under reduced pressure. Yield: 87 g (87%). $T_g$=54-64 °C. PDMS content was approximately 10% by weight.

# APPENDIX B

## Copolymer Imprinting Characterization Process

### Sample Preparation

Each polymer was dissolved in propylene glycol methyl ether acetate (PGMEA) (MicroChem) and forced through 0.2 μm filters to remove particulates. Solutions were spin coated onto silicon wafer substrates and soft-baked at 130 °C. On some samples, a $M_n$=950 kg·mol$^{-1}$ PMMA under-layer (MicroChem) was spin coated onto various patterned and unpatterned silicon substrates, baked at 130 °C for 5 min, and coated with a copolymer imprint resist. All samples were hard-baked at 180 °C for 20 min. Although the hard-bake temperature exceeds the $T_g$ of all species, no dewetting problems were observed.

### Imprinting Process and Characterization

Imprint molds were patterned thermal oxide on silicon substrates. Some molds were patterned with laser-interference lithography, while others through a combination of NIL, RIE, or chemical vapor deposition (CVD) processing. Additionally, molds were vapor coated with tridecafluoro-(1,1,2,2-tetrahydrooctyl)-trichlorosilane (Gelest) at 130 °C in nitrogen ambient; the surface treatment was annealed for 1 hr.

Imprinting was carried out using an NX-2000 (Nanonex). Samples were vacuum sealed followed by an imprint at various temperatures, pressures, and times ranging from 100-170 °C, 200-600 psi for 30 s-5 min. Samples were cooled to 40 °C before releasing

pressure. In some cases, additional annealing followed at 170 °C and low pressures before demolding.

Release forces were measured with silicon wafer substrates prepared in the aforementioned manner and surfactant treated grating molds of 700 nm pitch, 50% duty cycle, 200 nm feature height, and total area of 4.94 $cm^2$. After imprinting, each sample was subject to a tensile load normal to the interface plane between mold and substrate using an FDHT force tester (Larson Systems). Peak force, corresponding to the moment before adhesion failure, was recorded at a resolution of ± 0.02 N.

Due to the limited availability of molds, and to maintain experimental consistency, molds were rinsed in solvent prior to each imprint cycle. However, as illustrated, such cleaning does not imply that the resists have delamination issues. Nevertheless, in the event that improper handling leads to contamination of the mold by these copolymer resists, they can be readily dissolved in appropriate solvents, such as PGMEA or acetone since these PDMS copolymers are amorphous, uncrosslinked materials. The easy cleaning feature of these thermoplastic resists offers a processing advantage over cross-linking (or "curing") resists that are typically very difficult to clean or remove from the mold.[2] Cross-linked polymer generally must be plasma-etched in the event that it contaminates the valuable imprint mold, potentially jeopardizing the pattern fidelity.

To characterize the etch behavior of the copolymers, a capacitively coupled RIE was used. Typical flow gas rates were 20 sccm with chamber pressure ranging from 5-20 mtorr, and power 50-150 W. RIE was used to etch polymer residual, under-coating, and $SiO_2$. Metal lift-off was performed by evaporating layers of Ti and Ni onto substrates, and dissolving the PMMA under-coating in acetone. Thicknesses were measured using ellipsometry. Imprinted structure morphology was inspected with a scanning electron microscope (SEM).

# APPENDIX C

## Free Energy Calculation for Gratings

This MATLAB script calculates free energy with respect to triple point position down the sidewall of an arbitrary grating profile. This code is used to generate plots similar to Figure 3.5.

```
size=18;
width=2;

scale=1;

liquid='Water';
sigma=72.8 ...
    *1e-3;

theta=[140 120 100 80 60] ...
    *pi/180;

markers=5;

image=flipdim(imread('trace.tif')',2);

xmax=length(image(:,1));
ymax=length(image(1,:));

interval=ceil(max([xmax ymax])/100);

scale=scale/xmax;

for y = ymax:-1:1
    if image(1,y) == 0;
        curve=[1 y];
        break;
    end
end

priority=1;
search=[1 1; 1 0; 1 -1; 0 -1; -1 -1; -1 0; -1 1; 0 1];
n=1;
done=false;

while ~done,
    for i = priority:priority+8
        x=curve(n,1)+search(mod(i-1,8)+1,1);
```

```
        y=curve(n,2)+search(mod(i-1,8)+1,2);
        if x>xmax || x<1 || y>ymax || y<1
            done=true;
            break;
        end
        if image(x,y) == 0
            curve=[curve; x y];
            priority=mod(i+5-1,8)+1;
            break;
        end
    end
    n=n+1;
end

limits=[curve(1,2) curve(length(curve),2)];
trim=[find(curve(:,2) < limits(1),1) ...
    find(curve(:,2) > limits(2),1,'last')];
trim=[trim(1) floor((trim(2)-trim(1))/2+trim(1))];
curve=curve*scale;
curvetrim=curve((trim(1):1:trim(2)),:);

delta=[];
for i = 1:length(curvetrim)-interval
    delta=[delta; curvetrim(i,:)-curvetrim(i+interval,:)];
end

angle=atan2(-delta(:,2),-delta(:,1))+pi;

delta2d=sqrt(delta(:,1).^2 + delta(:,2).^2);
lineint=[];
for i = 1:length(delta2d)
    lineint=[lineint; sum(delta2d(1:i))/interval];
end

r=curve(length(curve),1)-curvetrim(:,1);
r=r(floor(interval/2):floor(length(curvetrim)-interval/2-1));

G=[];
for i = 1:length(theta)
    Gsub=[];
    for j = 1:length(r)
        dtheta=angle(j)-theta(i);
        if angle(j) > 3*pi/2
             dtheta=dtheta-2*pi;
        end
        if dtheta ~= 0
            Gsub=[Gsub; sigma * ( r(j).*dtheta ./ sin(dtheta) ...
            - cos(theta(i)).*lineint(j) )];
        else
            Gsub=[Gsub; sigma * ( r(j) ...
            - cos(theta(i)).*lineint(j) )];
        end
    end
    G=[G [(Gsub-Gsub(1)) / (xmax*scale) * 0.1]];
```

```
end

labels=['A';'B';'C';'D';'E';'F';'G';'H';'I';'J';'K'];
labels=labels(1:markers);
markers=round(linspace(1, length(G), markers));

clf;
A=newplot;
A=subplot(1,2,1);
plot([1:length(G)], G, 'linewidth', width);
set(A, 'XTick', markers);
set(A, 'XTickLabel', labels);
xlabel('triple point position', 'fontname', 'Times', 'fontsize', size);
ylabel('G*, free energy/grating length (erg/cm)', 'fontname', 'Times',
'fontsize', size);
title(liquid, 'fontname', 'Times', 'fontsize', size);
axis tight;
ylim('auto')
grid;

markers=round(markers+interval/2+trim(1));

A=subplot(1,2,2);
area([curve(1,1); curve(:,1); 2*curve(length(curve),1)-flipdim(curve(:,1),
1)], ...
    [curve(1,2)*1.1; curve(:,2); flipdim(curve(:,2),1)], 'linewidth', width);
hold;
plot(curve(markers,1), curve(markers,2), 'or'); hold;
text(curve(markers,1)+.1, curve(markers,2)+.1, labels);
xlabel('(\mum)', 'fontname', 'Times', 'fontsize', size);
title('Profile', 'fontname', 'Times', 'fontsize', size);
axis image;

A=subplot(1,2,1);
legend(num2str((1:1:length(theta))'));
for i = 1:length(theta)
    gtext(strcat(['\theta_c=' num2str(theta(i)*180/pi) '°']));
end
legend hide;
```

# APPENDIX D

## Free Energy and Equilibrium Meniscus Pressure Calculation for Cylindroids

This MATLAB script calculates free energy and equilibrium meniscus pressure with respect to triple point position down the sidewall of an arbitrary cylindroid profile. This code is used to generate plots similar to Figure 3.13.

```
size=18;
width=2;
dot=20;

scale=20;

liquid='Water & Varying Surfaces';
sigma=72.8 ...
    *1e-3;

theta=[90 50 10] ...
    *pi/180;

markers=5;

image=flipdim(imread('trace.tif')',2);

xmax=length(image(:,1));
ymax=length(image(1,:));

interval=ceil(max([xmax ymax])/100);

scale=scale/xmax;

for y = ymax:-1:1
    if image(1,y) == 0;
        curve=[1 y];
        break;
    end
end

priority=1;
search=[1 1; 1 0; 1 -1; 0 -1; -1 -1; -1 0; -1 1; 0 1];
n=1;
done=false;

while ~done,
    for i = priority:priority+8
```

```
        x=curve(n,1)+search(mod(i-1,8)+1,1);
        y=curve(n,2)+search(mod(i-1,8)+1,2);
        if x>xmax || x<1 || y>ymax || y<1
            done=true;
            break;
        end
        if image(x,y) == 0
            curve=[curve; x y];
            priority=mod(i+5-1,8)+1;
            break;
        end
    end
    n=n+1;
end

limit=[curve(length(curve),2)];
trim=find(curve(:,1) > limit,1);
trim=find(curve(trim:1:length(curve),2) < curve(trim,2),1)+trim;
trim=[trim find(curve(trim:1:length(curve),1) <= limit,1,'first')+trim];
trim=[trim(1)+interval trim(2)-interval];
curve=curve*scale;
curvetrim=curve((trim(1):1:trim(2)),:);

delta=[];
for i = 1:length(curvetrim)-interval
    delta=[delta; curvetrim(i,:)-curvetrim(i+interval,:)];
end

angle=atan2(-delta(:,2),-delta(:,1))+pi;

r=curve(length(curve),1)-curvetrim(:,1);
r=r(floor(interval/2):floor(length(curvetrim)-interval/2-1));

delta2d=sqrt(delta(:,1).^2 + delta(:,2).^2);
ringint=[];
rint=0;
for i = 1:length(delta2d)
    rint=rint+2*pi*r(i)*delta2d(i)/interval;
    ringint=[ringint; rint];
end

G=[];
for i = 1:length(theta)
    Gsub=[];
    for j = 1:length(r)
        dtheta=angle(j)-theta(i);
        if angle(j) > 3*pi/2
             dtheta=dtheta-2*pi;
        end
        Gsub=[Gsub; sigma * (pi*r(j)^2 * (1 + tan(dtheta/2)^2) ...
        - cos(theta(i))*ringint(j) )];
    end
    G=[G [(Gsub-Gsub(1)) * 1]];
end
```

```
P=[];
for i = 1:length(theta)
    Psub=[];
    for j = 1:length(r)
        dtheta=angle(j)-theta(i);
        if angle(j) > 3*pi/2
             dtheta=dtheta-2*pi;
        end
        Psub=[Psub; -2*sigma * sin(dtheta) ./ r(j) ];
    end
    P=[P [Psub * 10]];
end

labels=['A';'B';'C';'D';'E';'F';'G';'H';'I';'J';'K'];
labels=labels(1:markers);
markers=round(linspace(1, length(G), markers));

clf;
A=newplot;
A=subplot(2,2,1);
plot([1:length(G)], G, 'linewidth', width);
set(A, 'XTick', markers);
set(A, 'XTickLabel', labels);
title(liquid, 'fontname', 'Times', 'fontsize', size);
xlabel('triple point position', 'fontname', 'Times', 'fontsize', size);
ylabel('G*, free energy/cell (pJ)', 'fontname', 'Times', 'fontsize', size);
axis tight;
ylim('auto');
grid;

A=subplot(2,2,2);
plot([1:length(P)], P, 'linewidth', width);
set(A, 'XTick', markers);
set(A, 'XTickLabel', labels);
xlabel('triple point position', 'fontname', 'Times', 'fontsize', size);
ylabel('P, liquid pressure (bar)', 'fontname', 'Times', 'fontsize', size);
axis tight;
ylim('auto')
grid;

markers=round(markers+interval/2+trim(1));

A=subplot(2,2,[3 4]);
area([curve(:,1); 2*curve(length(curve),1)-flipdim(curve(:,1),1)], ...
    [curve(:,2); flipdim(curve(:,2),1)], 'linewidth', width); hold;
plot(curve(markers,1), curve(markers,2), '.r', 'markersize', dot);
text(curve(markers,1)-.05*scale*xmax*sin(angle(markers-markers(1)+1)-pi), ...
    curve(markers,2)+.05*scale*xmax*cos(angle(markers-markers(1)+1)-pi),
labels);
xlabel('Sidewall Profile', 'fontname', 'Times', 'fontsize', size);
axis image;
X=xlim; Y=ylim;
bar=floor(min([X(2)-X(1) Y(2)-Y(1)])/3);
```

```
[X,Y]=ginput(1);
plot([X X+5], [Y Y], 'linewidth', 2*width); hold;
gtext(strcat([ num2str(bar) '\mum']));
set(A, 'XTick', []);
set(A, 'YTick', []);

A=subplot(2,2,1);
X=xlim;
pause;
xlim(X);
legend(num2str((1:1:length(theta))'));
for i = 1:length(theta)
    gtext(strcat(['\theta_c=' num2str(theta(i)*180/pi) '°']));
end
legend hide;

A=subplot(2,2,2);
X=xlim;
pause;
xlim(X);
legend(num2str((1:1:length(theta))'));
for i = 1:length(theta)
    gtext(strcat(['\theta_c=' num2str(theta(i)*180/pi) '°']));
end
legend hide;
```

# APPENDIX E

## Detailed Pore Membrane Imprint Mold Fabrication Process

### Photomask Fabrication

Pore membrane CAD layout patterns were drawn in LayoutEditor software (juspertor). The layout patterns were exposed onto (5 in)$^2$, 90 mil thick, AZ-1518 coated soda-lime glass chromed photomasks. An Electromask pattern generator (Interserv) was used to transfer the patterns onto the photomasks first in pattern generation mode, then in image repeat mode. After exposure, all photomasks were developed in MF-319 developer (Microposit) for 110 s, followed by Cr etch in CR-14 solution (Cyantek) for 120 s, and finally photoresist removal in PRS-2000 (Baker) for 10 min.

### First Level Imprint Mold Fabrication

Begin with 100 mm diameter, 500 μm thick standard grade borosilicate glass wafers (planoptik):

1. Piranha clean, 3:1 $H_2SO_4$:$H_2O_2$ solution, 20 min
2. Top oxide strip, 10:1 HF:HCl, 1 min (6-7 μm)
3. Deposit, 10 nm/500 nm Cr/Au, e-beam evaporator (EnerJet)
4. Solvent clean, propylene glycol monomethyl ether acetate (PGMEA)
5. Spin coat, AZ-5214E (AZ Electronic Materials), 1000 rpm, 30 s

6. Soft-bake, hot plate, 110 °C, 50 s

7. Edge-bead removal, PGMEA

8. Expose, MA/BA6 (SUSS MicroTec), 200 mJ/cm$^2$ *ih* line

9. Spray develop, AZ 300 MIF (AZ Electronic Materials), 60 s

10. Flood expose, MA/BA6, 200 mJ/cm$^2$ *ih* line

11. Post exposure bake, oven, 180 °C, 10 min

12. Gold etch, TFA (Transene), 80 s

13. Chrome etch, CR-14, 8 s

14. Hard-bake, oven, 180 °C, 10 min

15. BSG etch, 10:1 HF:HCl, (nominal etch rate 6-7 μm/min)

16. Resist strip, 3:1 $H_2SO_4$:$H_2O_2$ solution, 20 min

17. Gold strip, TFA, 2 min

18. Chrome strip, CR-14, 20 s

End of first level patterning, and 0° sidewall mold fabrication. For 0° sidewall molds, skip past step 34 for fluorosurfactant coating.

**Second Level Imprint Mold Fabrication**

19. Piranha clean, 3:1 $H_2SO_4$:$H_2O_2$ solution, 20 min

20. Deposit, 10 nm/500 nm Cr/Au, argon plasma sputter (EnerJet)

21. Solvent clean, PGMEA

22. Spin coat, AZ-9260 (AZ Electronic Materials), 40 μm

23. Soft-bake, hot plate, 110 °C, 170 s

24. Edge-bead removal, PGMEA

25. Bake, hot plate, 110 °C, 10 min

26. Hydrate, $H_2O$, 40 °C, 10 min

27. Expose, MA/BA6, 7.1 J/cm$^2$ *ih* line

28. Develop, 1:3 AZ 400K:$H_2O$ (AZ Electronic Materials), 10 min

29. Gold etch, TFA, 80 s

30. Chrome etch, CR-14, 8 s

31. Resist strip, 3:1 $H_2SO_4$:$H_2O_2$ solution, 20 min

32. BSG etch, 10:1 HF:HCl, (nominal etch rate 6-7 μm/min)

33. Gold strip, TFA, 2 min

34. Chrome strip, CR-14, 20 s

End of second level patterning, and −90° sidewall mold fabrication. Prior to imprinting, molds were vapor coated with tridecafluoro-(1,1,2,2-tetrahydrooctyl)-trichlorosilane (Gelest) at 130 °C in nitrogen ambient; the surface treatment was annealed for 1 hr.

## APPENDIX F

### Detailed Pore Membrane Imprint Process

Begin with 100 mm diameter, 500 μm thick silicon carrier wafer:

1. Piranha clean, 3:1 $H_2SO_4$:$H_2O_2$ solution, 20 min

Perform steps 2-3 a total of three times

2. Coat PMMA 950K A9 (MicroChem), 1000 rpm, 3 s

3. Soft-bake, hot plate, 180 °C, 3 min

Perform steps 4-5 a total of two times

4. Coat SU-8 2010 (MicroChem), 2000 rpm, 30 s

5. Soft-bake, hot plate, 95 °C, 4 min

6. Bake, hot plate, 95 °C, 20 min

7. Imprint, NX-2000, pump 30 s, pre-imprint 0 °C, 120 psi, imprint 95 °C, 200 psi, vent 40 °C

8. Release mold

9. Flood expose, MA/BA6, 180 mJ/cm$^2$ *ih* line

10. Bond PDMS exit-side anchor, Sylgard 184 (Dow Corning), 10:1.05 base:curing agent

11. Bake, hot plate, 95 °C, 2 hr

12. Dissolve PMMA, acetone, 1-2 hr

13. Soak and rinse, isopropanol, 10 min

14. Dry

15. Bond reservoir polyethylene tubule, PDMS

16. Bake, oven, 95 °C, 2 hr

## APPENDIX G

### Detailed Goniometry of SU-8 Surfaces

Contact angle measurements were made for each of five water-methanol test mixtures on smooth SU-8 membrane control samples. The goniometer used was a CAM100 (KSV Instruments). Each SU-8 contact surface was liberally rinsed in deionized water and air dried prior to measurement. Example contact angle measurements are shown below.

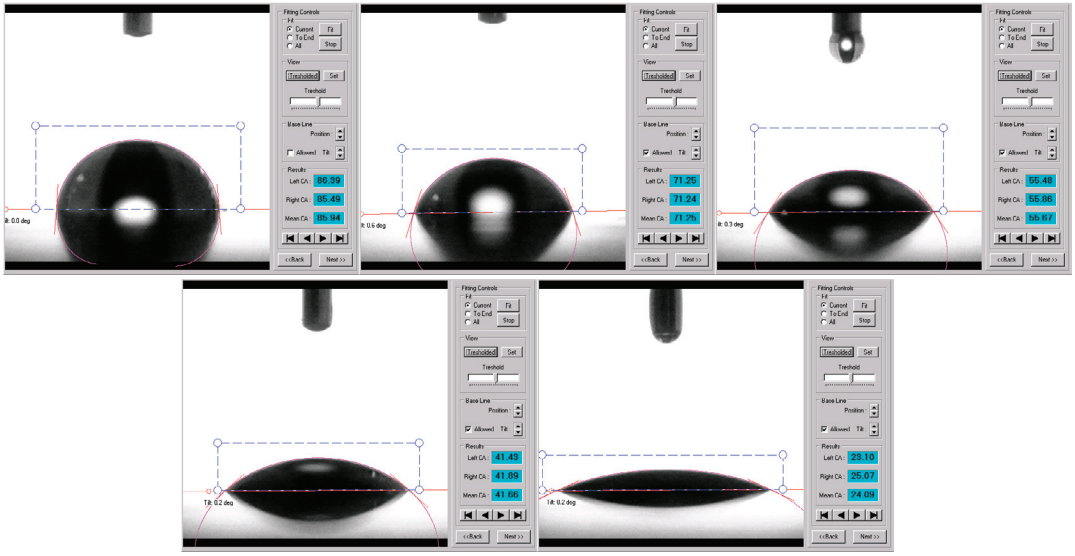


Figure G.1: Computed contact angles for water-methanol mixtures, of decreasing water fraction corresponding to mixtures in Table 5.1. Panels are in left-to-right order, row by row.

## APPENDIX H

### Equilibrium Meniscus Pressure and Breakthrough Pressure Calculation

This MATLAB script calculates equilibrium meniscus pressure with respect to triple point position down the sidewall of an arbitrary cylindroid profile, as well as breakthrough pressure. This code is used to generate plots similar to Figure 5.4.

```
size=14;
width=2;
dot=20;

scale=50*2267.91/864;

sigma=[72.94 40 30 25 22.50] ...
    *1e-3;

theta=[85.05 68.69 56.73 43.88 24.27] ...
    *pi/180;

fluids=[1 .75 .5 .25 0];

markers=5;

image=flipdim(imread('trace.tif')',2);

xmax=length(image(:,1));
ymax=length(image(1,:));

interval=ceil(max([xmax ymax])/100);

scale=scale/xmax;

for y = ymax:-1:1
    if image(1,y) == 0;
        curve=[1 y];
        break;
    end
end

priority=1;
search=[1 1; 1 0; 1 -1; 0 -1; -1 -1; -1 0; -1 1; 0 1];
n=1;
done=false;

while ~done,
```

```
    for i = priority:priority+8
        x=curve(n,1)+search(mod(i-1,8)+1,1);
        y=curve(n,2)+search(mod(i-1,8)+1,2);
        if x>xmax || x<1 || y>ymax || y<1
            done=true;
            break;
        end
        if image(x,y) == 0
            curve=[curve; x y];
            priority=mod(i+5-1,8)+1;
            break;
        end
    end
    n=n+1;
end

limit=[curve(length(curve),2)];
trim=find(curve(:,1) > limit,1);
trim=find(curve(trim:1:length(curve),2) < curve(trim,2),1)+trim;
trim=[trim find(curve(trim:1:length(curve),1) <= limit,1,'first')+trim];
trim=[trim(1)+interval trim(2)-interval];
curve=curve*scale;
curvetrim=curve((trim(1):1:trim(2)),:);

delta=[];
for i = 1:length(curvetrim)-interval
    delta=[delta; curvetrim(i,:)-curvetrim(i+interval,:)];
end

angle=atan2(-delta(:,2),-delta(:,1))+pi;

r=curve(length(curve),1)-curvetrim(:,1);
r=r(floor(interval/2):floor(length(curvetrim)-interval/2-1));

delta2d=sqrt(delta(:,1).^2 + delta(:,2).^2);
ringint=[];
rint=0;
for i = 1:length(delta2d)
    rint=rint+2*pi*r(i)*delta2d(i)/interval;
    ringint=[ringint; rint];
end

G=[];
for i = 1:length(theta)
    Gsub=[];
    for j = 1:length(r)
        dtheta=angle(j)-theta(i);
        if angle(j) > 3*pi/2
             dtheta=dtheta-2*pi;
        end
        Gsub=[Gsub; sigma(i) * (pi*r(j)^2 * (1 + tan(dtheta/2)^2) ...
        - cos(theta(i))*ringint(j) )];
    end
    G=[G [(Gsub-Gsub(1)) * 1]];
```

```
end

P=[];
for i = 1:length(theta)
    Psub=[];
    for j = 1:length(r)
        dtheta=angle(j)-theta(i);
        if angle(j) > 3*pi/2
             dtheta=dtheta-2*pi;
        end
        Psub=[Psub; -2*sigma(i) * sin(dtheta) ./ r(j) ];
    end
    P=[P [Psub * 1000]];
end

labels=['A';'B';'C';'D';'E';'F';'G';'H';'I';'J';'K'];
labels=labels(1:markers);
markers=round(linspace(1, length(G), markers));

clf;
A=newplot;
A=subplot(2,2,1);
plot([1:length(P)], P, 'linewidth', width);
set(A, 'XTick', markers);
set(A, 'XTickLabel', labels);
xlabel('triple point position', 'fontname', 'Times', 'fontsize', size);
ylabel('P, liquid pressure (kPa)', 'fontname', 'Times', 'fontsize', size);
axis tight;
ylim('auto')
grid;

Pmax=[];
for i = 1:length(theta)
    Pmax=[Pmax; max(P(:,i)) ];
end
A=subplot(2,2,2);
plot([1:length(Pmax)], Pmax, 'o');
set(A, 'XTick', [1:length(Pmax)]);
set(A, 'XTickLabel', fluids);
xlabel('H_2O fraction (wt)', 'fontname', 'Times', 'fontsize', size);
ylabel('P_{max}, liquid pressure (kPa)', 'fontname', 'Times', 'fontsize',
size);
grid;

markers=round(markers+interval/2+trim(1));

A=subplot(2,2,[3 4]);
area([curve(:,1); 2*curve(length(curve),1)-flipdim(curve(:,1),1)], ...
    [curve(:,2); flipdim(curve(:,2),1)], 'linewidth', width); hold;
plot(curve(markers,1), curve(markers,2), '.r', 'markersize', dot);
text(curve(markers,1)-.05*scale*xmax*sin(angle(markers-markers(1)+1)-pi), ...
    curve(markers,2)+.05*scale*xmax*cos(angle(markers-markers(1)+1)-pi),
labels);
xlabel('Sidewall Profile', 'fontname', 'Times', 'fontsize', size);
```

```
axis image;
X=xlim; Y=ylim;
bar=floor(min([X(2)-X(1) Y(2)-Y(1)])/3);
[X,Y]=ginput(1);
plot([X X+10], [Y Y], 'linewidth', 2*width); hold;
gtext(strcat([ num2str(bar) '\mum']));
set(A, 'XTick', []);
set(A, 'YTick', []);

A=subplot(2,2,1);
X=xlim;
pause;
xlim(X);
legend(num2str((1:1:length(theta))'));
for i = 1:length(theta)
    gtext(num2str(fluids(i)));
end
legend hide;
```

## BIBLIOGRAPHY


1. Chou, S. Y., P. R. Krauss, *et al*. "Sub-10 nm imprint lithography and applications." *Journal of Vacuum Science & Technology B*, 15(6): 2897-2904 (1997).

2. Colburn, M., S. Johnson, *et al*. "Step and Flash Imprint Lithography: A New Approach to High-Resolution Patterning." *Proceedings of the Society of Photo-Optical Instrumentation Engineers*, 3676(I): 379 (1999).

3. Guo, L. J. "Recent progress in nanoimprint technology and its applications." *Journal of Physics D-Applied Physics*, 37(11): R123-R141 (2004).

4. Austin, M. D., H. X. Ge, *et al*. "Fabrication of 5 nm linewidth and 14 nm pitch features by nanoimprint lithography." *Applied Physics Letters*, 84(26): 5299-5301 (2004).

5. Perret, C., C. Gourgon, *et al*. "Characterization of 8-in wafers printed by nanoimprint lithography." *Microelectronic Engineering*, 73-74: 172-177 (2004).

6. Guo, L. J. "Nanoimprint lithography: Methods and material requirements." *Advanced Materials*, 19(4): 495-513 (2007).

7. Sotomayor Torres, C. M. *Alternative lithography : unleashing the potentials of nanotechnology*. New York, Kluwer Academic/Plenum (2003).

8. Chen, Y., D. Macintyre, *et al*. "Fabrication of high electron mobility transistors with T-gates by nanoimprint lithography." *Journal of Vacuum Science & Technology B*, 20(6): 2887-2890 (2002).

9. Hirai, Y., S. Yoshida, *et al*. "Defect analysis in thermal nanoimprint lithography." *Journal of Vacuum Science & Technology B*, 21(6): 2765-2770 (2003).

10. Israelachvili, J. N. *Intermolecular and surface forces*. London, Academic (1992).

11. Adamson, A. W. and A. P. Gast. *Physical chemistry of surfaces*. New York, Wiley (1997).

12. Keil, M., M. Beck, *et al*. "Process development and characterization of antisticking layers on nickel-based stamps designed for nanoimprint lithography." *Journal of Vacuum Science & Technology B*, 22(6): 3283-3287 (2004).

13. Lee, N., S. Choi, *et al*. "Self-assembled monolayer as an antiadhesion layer on a nickel nanostamper in the nanoreplication process for optoelectronic applications." *Applied Physics Letters*, 88(7) (2006).

14. Jaszewski, R. W., H. Schift, *et al*. "The deposition of anti-adhesive ultra-thin teflon-like films and their interaction with polymers during hot embossing." *Applied Surface Science*, 143(1-4): 301-308 (1999).

15. Beck, M., M. Graczyk, *et al*. "Improving stamps for 10 nm level wafer scale nanoimprint lithography." *Microelectronic Engineering*, 61-2: 441-448 (2002).

16. Lee, M. J., N. Y. Lee, *et al*. "Antiadhesion surface treatments of molds for high-resolution unconventional lithography." *Advanced Materials*, 18(23): 3115-3119 (2006).

17. Wang, C. F., S. F. Chiou, *et al*. "Polybenzoxazine as a mold-release agent for nanoimprint lithography." *Langmuir*, 23(11): 5868-5871 (2007).

18. Schmid, H. and B. Michel. "Siloxane polymers for high-resolution, high-accuracy soft lithography." *Macromolecules*, 33(8): 3042-3049 (2000).

19. McClelland, G. M., M. W. Hart, *et al*. "Nanoscale patterning of magnetic islands by imprint lithography using a flexible mold." *Applied Physics Letters*, 81(8): 1483-1485 (2002).

20. Kim, Y. S., H. H. Lee, *et al*. "High density nanostructure transfer in soft molding using polyurethane acrylate molds and polyelectrolyte multilayers." *Nanotechnology*, 14(10): 1140-1144 (2003).

21. Khang, D. Y., H. Kang, *et al*. "Low-pressure nanoimprint lithography." *Nano Letters*, 4(4): 633-637 (2004).

22. Khang, D. Y. and H. H. Lee. "Sub-100 nm patterning with an amorphous fluoropolymer mold." *Langmuir*, 20(6): 2445-2448 (2004).

23. Choi, D. G., J. H. Jeong, *et al*. "Fluorinated organic-inorganic hybrid mold as a new stamp for nanoimprint and soft lithography." *Langmuir*, 21(21): 9390-9392 (2005).

24. Chen, X., J. A. Gardella, *et al*. "Fourier-Transform Infrared and Electron-Spectroscopy for Chemical-Analysis Studies of Block Copolymers of Styrene and Dimethylsiloxane." *Macromolecules*, 25(24): 6621-6630 (1992).

25. Chen, X., J. A. Gardella, *et al*. "Surface Ordering of Block Copolymers." *Macromolecules*, 25(24): 6631-6637 (1992).

26. Chen, X. and J. A. Gardella. "Surface Modification of Polymers by Blending Siloxane Block-Copolymers." *Macromolecules*, 27(12): 3363-3369 (1994).

27. Yilgör, I., E. Yilgör, *et al*. "Silicone Surfactants. Part V: Siloxane Copolymers as Surface Modifying Additives for Polymers." *Tenside Surf. Det*., 30(3): 158-164 (1993).

28. Yilgör, I. "Polymer Surface Modifiers." Silicone surfactants. R. M. Hill. New York, Marcel Dekker (1999).

29. Stoebe, T., R. M. Hill, *et al*. "Surfactant Enhanced Spreading." Silicone surfactants. R. M. Hill. New York, Marcel Dekker (1999).

30. Ma, M. L., R. M. Hill, *et al*. "Electrospun poly(styrene-block-dimethylsiloxane) block copolymer fibers exhibiting superhydrophobicity." *Langmuir*, 21(12): 5549-5554 (2005).

31. Xu, T., C. J. Hawker, *et al*. "Interfacial interaction dependence of microdomain orientation in diblock copolymer thin films." *Macromolecules*, 38(7): 2802-2805 (2005).

32. Barbero, D. R., M. S. M. Saifullah, *et al*. "High resolution nanoimprinting with a robust and reusable polymer mold." *Advanced Functional Materials*, 17(14): 2419-2425 (2007).

33. Williams, K. R. and R. S. Muller. "Etch rates for micromachining processing." *Journal of Microelectromechanical Systems*, 5(4): 256-269 (1996).

34. Williams, K. R., K. Gupta, *et al*. "Etch rates for micromachining processing - Part II." *Journal of Microelectromechanical Systems*, 12(6): 761-778 (2003).

35. Carlberg, P., M. Graczyk, *et al*. "Lift-off process for nanoimprint lithography." *Microelectronic Engineering*, 67-8: 203-207 (2003).

36. Schulz, H., H. C. Scheer, *et al*. "New polymer materials for nanoimprinting." *Journal of Vacuum Science & Technology B*, 18(4): 1861-1865 (2000).

37. Hofer, D. C., R. D. Miller, *et al*. "Polysilane Bilayer Uv Lithography." *Proceedings of the Society of Photo-Optical Instrumentation Engineers*, 469: 16-23 (1984).

38. Chou, N. J., C. H. Tang, *et al*. "Mechanism of Oxygen Plasma-Etching of Polydimethyl Siloxane Films." *Applied Physics Letters*, 46(1): 31-33 (1985).

39. Choi, P., P. F. Fu, *et al*. "Siloxane copolymers for nanoimprint lithography." *Advanced Functional Materials*, 17(1): 65-70 (2007).

40. Howard, R. E., E. L. Hu, *et al*. "Multilevel Resist for Lithography Below 100-Nm." *Ieee Transactions on Electron Devices*, 28(11): 1378-1381 (1981).

41. Reiter, G. "Dewetting of Thin Polymer-Films." *Physical Review Letters*, 68(1): 75-78 (1992).

42. Rowland, H. D., A. C. Sun, *et al*. "Impact of polymer film thickness and cavity size on polymer flow during embossing: toward process design rules for nanoimprint lithography." *Journal of Micromechanics and Microengineering*, 15(12): 2414-2425 (2005).

43. Rowland, H. D., W. P. King, *et al*. "Simulations of nonuniform embossing: The effect of asymmetric neighbor cavities on polymer flow during nanoimprint lithography." *Journal of Vacuum Science & Technology B*, 23(6): 2958-2962 (2005).

44. Cheng, X., L. J. Guo, *et al*. "Room-temperature, low-pressure nanoimprinting based on cationic photopolymerization of novel epoxysilicone monomers." *Advanced Materials*, 17(11): 1419-1424 (2005).

45. Wenzel, R. N. "Resistance of solid surfaces to wetting by water." *Industrial and Engineering Chemistry*, 28: 988-994 (1936).

46. Cassie, A. B. D. and S. Baxter. "Wettability of porous surfaces." *Transactions of the Faraday Society*, 40: 0546-0550 (1944).

47. Neinhuis, C. and W. Barthlott. "Characterization and distribution of water-repellent, self-cleaning plant surfaces." *Annals of Botany*, 79(6): 667-677 (1997).

48. Koch, K., H. F. Bohn, *et al*. "Hierarchically Sculptured Plant Surfaces and Superhydrophobicity." *Langmuir*, 25(24): 14116-14120 (2009).

49. Furstner, R., W. Barthlott, *et al*. "Wetting and self-cleaning properties of artificial superhydrophobic surfaces." *Langmuir*, 21(3): 956-961 (2005).

50. Sun, M. H., C. X. Luo, *et al*. "Artificial lotus leaf by nanocasting." *Langmuir*, 21(19): 8978-8981 (2005).

51. Gao, L. C. and T. J. McCarthy. "A perfectly hydrophobic surface (theta(A)/ theta(R)=180 degrees/180 degrees)." *Journal of the American Chemical Society*, 128(28): 9052-9053 (2006).

52. Callies, M. and D. Quere. "On water repellency." *Soft Matter*, 1(1): 55-61 (2005).

53. Nosonovsky, M. and B. Bhushan. "Biologically inspired surfaces: Broadening the scope of roughness." *Advanced Functional Materials*, 18(6): 843-855 (2008).

54. Cheng, Y. T., D. E. Rodak, *et al*. "Microscopic observations of condensation of water on lotus leaves." *Applied Physics Letters*, 87(19) (2005).

55. Ahuja, A., J. A. Taylor, *et al*. "Nanonails: A simple geometrical approach to electrically tunable superlyophobic surfaces." *Langmuir*, 24(1): 9-14 (2008).

56. Marmur, A. "Wetting on hydrophobic rough surfaces: To be heterogeneous or not to be?" *Langmuir*, 19(20): 8343-8348 (2003).

57. Patankar, N. A. "Transition between superhydrophobic states on rough surfaces." *Langmuir*, 20(17): 7097-7102 (2004).

58. Yuan, J. K., X. G. Liu, *et al*. "Superwetting nanowire membranes for selective absorption." *Nature Nanotechnology*, 3(6): 332-336 (2008).

59. Marmur, A. "Underwater superhydrophobicity: Theoretical feasibility." *Langmuir*, 22(4): 1400-1402 (2006).

60. Marmur, A. "From hygrophilic to superhygrophobic: Theoretical conditions for making high-contact-angle surfaces from low-contact-angle materials." *Langmuir*, 24(14): 7573-7579 (2008).

61. Tuteja, A., W. Choi, *et al*. "Designing superoleophobic surfaces." *Science*, 318(5856): 1618-1622 (2007).

62. Tuteja, A., W. Choi, *et al*. "Robust omniphobic surfaces." *Proceedings of the National Academy of Sciences of the United States of America*, 105(47): 18200-18205 (2008).

63. Saam, J. C., D. J. Gordon, *et al*. "Block copolymers of polydimethylsiloxe and and polystyrene." *Macromolecules*, 3(1): 1-& (1970).

64. Hamley, I. W. *The physics of block copolymers*. Oxford, Oxford University Press (1998).

65. Smith, S. D., J. M. Desimone, *et al*. "Synthesis and characterization of poly(methyl methacrylate)-g-poly(dimethylsiloxane) copolymers .1. Bulk and surface characterization." *Macromolecules*, 25(10): 2575-2581 (1992).

66. Vanoss, C. J., M. K. Chaudhury, *et al*. "Interfacial Lifshitz-Vanderwaals and polar interactions in macroscopic systems." *Chemical Reviews*, 88(6): 927-941 (1988).

67. Vanoss, C. J. "Acid-base interfacial interactions in aqueous-media." *Colloids and Surfaces a-Physicochemical and Engineering Aspects*, 78: 1-49 (1993).

68. Hansen, C. M. *Hansen solubility parameters : a user's handbook*. Boca Raton, Fla., CRC Press (2000).

69. Nosonovsky, M. "Multiscale roughness and stability of superhydrophobic biomimetic interfaces." *Langmuir*, 23(6): 3157-3161 (2007).

70. Gao, L. C. and T. J. McCarthy. ""Artificial lotus leaf" prepared using a 1945 patent and a commercial textile." *Langmuir*, 22(14): 5998-6000 (2006).

71. Kim, B. S. and P. Harriott. "Critical entry pressure for liquids in hydrophobic membranes." *Journal of Colloid and Interface Science*, 115(1): 1-8 (1987).

72. Choi, J., A. Roychowdhury, *et al*. "Low Cost Fabrication of Micro- and Nanopores in Free-Standing Polymer Membranes for Study of Lipid Adsorption." Nsti Nanotech 2008, Vol 1, Technical Proceedings - Materials, Fabrication, Particles, and Characterization. M. Laudon and B. Romanowicz. Boca Raton, Crc Press-Taylor & Francis Group (2008).

73. Hu, W., B. Yang, *et al*. "Three-dimensional SU-8 structures by reversal UV imprint." *Journal of Vacuum Science & Technology B*, 24(5): 2225-2229 (2006).

74. Cheng, X. and L. J. Guo. "A combined-nanoimprint-and-photolithography patterning technique." *Microelectronic Engineering*, 71(3-4): 277-282 (2004).

75. Cheng, X. and L. J. Guo. "One-step lithography for various size patterns with a hybrid mask-mold." *Microelectronic Engineering*, 71(3-4): 288-293 (2004).

76. Wang, S., C. C. Zeng, *et al*. "Polymeric nanonozzle array fabricated by sacrificial template imprinting." *Advanced Materials*, 17(9): 1182-1186 (2005).

77. Lee, J. N., C. Park, *et al*. "Solvent compatibility of poly(dimethylsiloxane)-based microfluidic devices." *Analytical Chemistry*, 75(23): 6544-6554 (2003).

78. Timoshenko, S., S. Woinowsky-Krieger, *et al*. *Theory of plates and shells*. New York, McGraw-Hill (1959).

79. McAleavey, A., G. Coles, *et al*. "Mechanical properties of SU-8." Materials Science of Microelectromechanical Systems. A. H. Heuer and S. J. Jacobs. Warrendale, Materials Research Society (1999).

80. Harrison, D. J., K. Fluri, *et al*. "Micromachining a miniaturized capillary electrophoresis-based chemical-analysis system on a chip." *Science*, 261(5123): 895-897 (1993).

81. Iliescu, C., J. Jing, *et al*. "Characterization of masking layers for deep wet etching of glass in an improved HF/HCl solution." 2nd International Conference on Advances of Thin Films and Coating Technology, Singapore, Singapore, Elsevier Science Sa.

82. Conedera, V., B. Le Goff, *et al*. "Potentialities of a new positive photoresist for the realization of thick moulds." *Journal of Micromechanics and Microengineering*, 9(2): 173-175 (1999).

83. Matsumoto, M., Y. Takaoka, *et al*. "Liquid-vapor interface of water-methanol mixture .1. Computer simulation." *Journal of Chemical Physics*, 98(2): 1464-1472 (1993).